



Dissertation
DEVELOPING CFD SOFTWARE
FOR SIMULATING GAS-SOLID RISER FLOW

IS BUNYAMIN SURYO

Supervisor :

Prof. Dr. Ir. Tri Yogi Yuwono, DEA

Prof. Dr.-Ing. Uwe Schnell (Stuttgart University, Germany)

DOCTORAL PROGRAM
ENERGY CONVERSION ENGINEERING
MECHANICAL ENGINEERING DEPARTMENT
INDUSTRIAL TECHNOLOGY & SYSTEM ENGINEERING FACULTY
INSTITUT TEKNOLOGI SEPULUH NOPEMBER
SURABAYA
2022



Dissertation

Developing CFD Software for Simulating Gas-Solid Riser Flow

**IS BUNYAMIN SURYO
7007201005**

SUPERVISOR:

Prof. Dr. Ir. Tri Yogi Yuwono, DEA

Prof. Dr.-Ing. Uwe Schnell (Stuttgart University, Germany)

DOCTORAL PROGRAM

ENERGY CONVERSION ENGINEERING

MECHANICAL ENGINEERING DEPARTMENT

INDUSTRIAL TECHNOLOGY & SYSTEM ENGINEERING FACULTY

INSTITUT TEKNOLOGI SEPULUH NOPEMBER

SURABAYA

2022

Is Bunyamin Suryo

Vorgelegt von

Developing CFD Software for Simulating Gas-Solid Riser Flow

aus Lamongan, Indonesia

Institut für Feuerungs- und Kraftwerkstechnik
der Universität Stuttgart

2018

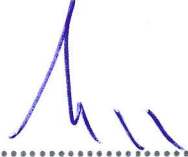


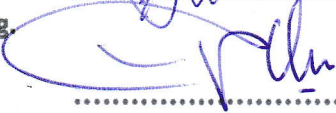


APPROVAL PAGE

Developing CFD Software for Simulating Gas-Solid Riser Flow
by
IS BUNYAMIN SURYO
7007201005

Dissertation submitted to the faculty of Industrial Technology and System
Engineering - Institut Teknologi Sepuluh Nopember (ITS)
in partial fulfillment of the requirements for the degree of
Doctor
in
Mechanical Engineering

Graduation period:
March, 26th - 27th 2022 - Gasal 2021/2022

Approved by :

- | | | |
|--|--|-----------------|
| 1. Prof. Dr. Ir. Triyogi Yuwono, DEA.
NIP. 19600129 198701 1001 |  | (Supervisor) |
| 2. Prof. Dr.-Ing. Uwe Schnell
(Stuttgart University, Germany) |  | (Co-Supervisor) |
| 3. Prof. Ir. Sutardi, M.Eng. Ph.D
NIP. 19641228 199003 1002 |  | (Examiner I) |
| 4. Prof. Dr-Eng. Ir. Prabowo, M.Eng.
NIP. 19650505 199003 1005 |  | (Examiner II) |
| 5. Prof. Dr. Ir. Indarto, DEA.
NIP. 19530622 198101 1001 |  | (Examiner III) |
| 6. Dr. Wawan A. Widodo, ST. MT.
NIP. 19710405 199702 1001 |  | (Examiner IV) |

Head of Mechanical Engineering Department, FTIRS - ITS




Dr. Ir. Atok Setiyawan, M.Eng.Sc
NIP. 19660402-198903 1002

For
my beloved parents, Suryono and Maslehah
my lovely wife, Farida
my sweetie daughter, Hana

Indeed, in the creation of the heavens and the earth and the alternation of the night and the day are signs for those of understanding [Ali 'Imran:190]

Acknowledgements

Foremost, I would like to reveal my greatest gratitude to my supervisor Prof. Dr. Ir. Tri Yogi Yuwono, DEA, Rector of Institut Teknologi Sepuluh Nopember (ITS) 2011-2015, for great encouragement during my doctoral research. Great thank to him for an initial direction for my research and good discussion during the doctoral research. A huge thank also for my Co-supervisor, the group leader of Feuerungs- und Dampferzeugersimulation (FDS) department of IFK Universitt Stuttgart, Prof. Dr.-Ing. Uwe Schnell for intensive discussion during the research. He leaves me the freedom of focus on the greatest academic interest. His big helps on either academic and non-academic issues for me were really amazing. He always gave his time for discussion and delivered a such really positive feedback on my progress and report manuscript. He also recommended for me some academic journeys for enriching my knowledge.

I would like to thank Prof. Juray De Wilde from IMMC-UCLouvain, Belgium for a short term intensive discussion on fundamental issues of developing CFD software dedicated to solve gas-solid multiphase flow. The discussion was absolutely very important for me in developing my code. I would like to thank the members of my examination committee, Prof. Sutardi, Prof. Prabowo, Prof. Indarto and Dr. Wawan Aries W. for their great attention on my doctoral thesis. They gave valuable and useful comments during the examination such that my doctoral thesis become more preferable.

Great thank also for some former researchers at IFK Universitt Stuttgart, Dominik Kurz; Michael Muller; and Max Weidmann, for their good introduction of AIOLOS and how to utilize it for simulations. It was really helpful in the early period of my doctoral research at IFK Uni Stuttgart. For all colleagues in FDS department of IFK Universitt Stuttgart, Marcel Beirow; Harold Garcia; Bernhard Schopfer, thank you so much for really kind helps, discussions, knowledge sharing etc. during my doctoral research. That was a great experience for me having a such great research team. My thank also should be delivered to Frau Renate Klein who always help me in the administration matters. Thank you in advance for the administrator in High Performance Computing Center Stuttgart (HLRS) and Karlsruhe

Institute of Technology (KIT) who provide me an access to BwUniCluster computer cluster. The access was really help me in providing the computing resources for my reserach simulations.

For the great and limitless support and motivation, I should express a great thank to the big family of Suryono and Maslehah, my lovely wife Farida Rahmawati Purnadiana, and my sweetie daughter Hana Nisaul Lubna. Without their daily invocation, finishing the doctoral research was seemingly really hard. But their continuous hopefulness lifted some burdens on my shoulder such that my doctoral research was enjoyable episode, my endless love dedicated for them. A big appreciation also for the Indonesian muslim community united in Ngaji Stuttgart, their kind and kinship hospitalizing during my life in Stuttgart was really amazing.

Finally, I would like to thank the Indonesian government by the Ministry of National Education in providing the financial support for my doctoral research. In exchange, the endless dedication for the home country is worthy devoted.

August, 2018

Is Bunyamin Suryo

Contents

Abstract	xiii
Nomenclature	xv
1 Introduction	1
1.1 Fluidization and its Applications	1
1.2 Research Objective	7
1.3 Thesis Outline	7
2 Gas-Solid Two Phase Flow	9
2.1 Mechanism of Gas-Solid Riser Flow	9
2.2 Computational Methods of Gas-Solid Two Phase Flow	12
2.3 The Development of the Two-Fluid Model	13
3 Two-Fluid Model for Gas-Solid Riser Flow	23
3.1 The Governing Equations of Two-Fluid Model	23
3.2 The Constitutive Equations	24
3.2.1 Viscous Stress Tensor for gas phase	24
3.2.2 Viscous Stress Tensor for solid phase	25
3.2.3 Pressure for gas phase	26
3.2.4 Interphase Momentum Transfer	26
3.2.4.1 Wen and Yu model	28
3.2.4.2 Syamlal and O'Brien model	28
3.2.4.3 Gidaspow model	29
3.2.5 Kinetic Theory of Granular Flow (KTGF)	30
3.2.5.1 Solid Viscosity	34

3.2.5.2	Solid Pressure	35
3.2.5.3	Radial Distribution Function	35
3.2.5.4	Coefficient of Restitution	37
3.2.6	Frictional Stress Model	39
3.2.6.1	$k-\epsilon$ Turbulence Model for the Gas Phase	41
3.3	The 3D CFD-code AIOLOS	42
4	Numerical Simulation Procedure	45
4.1	Solution Algorithm	45
4.2	Numerical Scheme	46
4.3	Solving Solid Phase Continuity Equation	50
5	Numerical Simulation of 3D Gas-Solid Flow in Cylindrical Riser	55
5.1	Simulation Parameters	55
5.2	Simulation Results and Discussion	56
5.2.1	The Influence of Meshing	58
5.2.2	The Influence of Initial Condition	60
5.2.3	The Variation of Simulation Parameters	61
5.2.4	The Effect of Drag Model	72
5.2.4.1	Time Step of 0.0001 s	73
5.2.4.2	Time Step of 0.00015 s	78
5.2.5	The Effect of Radial Distribution Function Model	82
5.2.6	The Effect of Restitution Coefficient Value	84
5.2.7	The Effect of Simulation Time Step	85
5.2.8	Comparison of the Current Simulation with L. Cabezas's Result	88
5.2.9	Comparison of Laminar and Turbulent Simulation	91
5.2.10	Discussion	95
5.2.10.1	Wall Boundary Condition	95
5.2.10.2	Drag Model	98
5.2.10.3	Gas Phase Viscous Model	99
6	Numerical Simulation of 3D Gas-Solid Flow in Rectangular Riser	101
6.1	Simulation Parameters	101

6.2	Simulation Results and Discussion	104
6.2.1	Solid Velocity Lateral Profile	104
6.2.2	Gas Volume Fraction Lateral Profile	105
7	Conclusions and Outlook	107
7.1	Conclusions	107
7.2	Outlook	109
	Bibliography	111

List of Figures

1.1	Winkler coal gasifier reactor [77]	2
1.2	Bubbling fluidized bed schematic [75]	3
1.3	Circulating fluidized bed schematic [4]	5
2.1	Fluidized beds in different regimes [39]	10
2.2	The Geldart particles classification diagram [24]	11
2.3	Fluidization process of different groups of Geldart particles	12
2.4	Two-Fluid Model concept for gas-solid flows	14
2.5	Sketch of solid pressure profile in fluidized beds [11]	19
3.1	Free body diagram of forces acting on a solid particle sphere	27
3.2	Comparison of different models of the momentum exchange coefficient	29
3.3	The granular temperature concept based on kinetic theory of granular flow [36]	31
3.4	Comparison of different models of the radial distribution function	38
3.5	The hydrodynamics of solid particles on dilute and dense flow	39
3.6	Internal friction angle	40
3.7	The differences of calculation between the existing and the developed AIOLOS	44
4.1	The solution algorithm	47
4.2	Non-staggered grid	50
4.3	The central difference scheme	51
5.1	Geometry and boundary conditions used in simulations (presented in 2D-plane)	57
5.2	Two different meshings	57
5.3	The highlighted position for capturing the simulation results	59

5.4	Solid velocity profile obtained by two different meshes: standard and fine . . .	60
5.5	Solid volume fraction profile obtained by two different meshes: standard and fine	61
5.6	Solid velocity profile obtained by different initial conditions	62
5.7	Solid volume fraction profile obtained by different initial conditions	62
5.8	The combination of simulation parameters	63
5.9	The solid velocity and solid volume fraction contour for different model combinations at time step 0.0001 s	65
5.10	The solid volume fraction profile for different model combinations at time step 0.0001 s	65
5.11	The solid velocity profile for different model combinations at time step 0.0001 s	66
5.12	The solid velocity and solid volume fraction contour for different model combinations at time step 0.00015 s	66
5.13	The solid volume fraction profile for different model combinations at time step 0.00015 s	67
5.14	The solid velocity profile for different model combinations at time step 0.00015 s	67
5.15	The comparison of gas velocity profile of group II after 40 s simulation with time step of 0.0001 s	68
5.16	The comparison of solid velocity profile of group II after 40 s simulation with time step of 0.0001 s	69
5.17	The comparison of solid volume fraction profile of group II after 40 s simulation with time step of 0.0001 s	69
5.18	The comparison of gas velocity profile of group IV after 40 s simulation with time step of 0.00015 s	70
5.19	The comparison of solid velocity profile of group IV after 40 s simulation with time step of 0.00015 s	71
5.20	The comparison of solid volume fraction profile of group IV after 40 s simulation with time step of 0.00015 s	71
5.21	Solid phase mass flux, $q_{m,r}$, from 30 - 40 s at the highlighted position (at height of 3.4 m above the riser inlet)	73

5.22 Solid velocity contour at different time and riser height [based on Gidaspow drag model]	74
5.23 Solid volume fraction contour at different time and riser height [based on Gidaspow drag model]	75
5.24 Time-averaged of gas phase velocity profiles for simulations with different drag models and time step of 0.0001 s	75
5.25 Time-averaged of solid phase velocity profiles for simulations with different drag models and time step of 0.0001 s	76
5.26 Time-averaged of solid volume fraction profiles for simulations with different drag models and time step of 0.0001 s	77
5.27 Comparison of the gas velocity distribution at time=40 s for simulations with different drag models and time step of 0.0001 s	78
5.28 Comparison of the solid velocity distribution at time=40 s for simulations with different drag models and time step of 0.0001 s	79
5.29 Comparison of the solid volume fraction distribution at time=40 s for simula- tions with different drag models and time step of 0.0001 s	79
5.30 Time-averaged gas phase velocity profiles for simulations with different drag models and time step of 0.00015 s	80
5.31 Time-averaged solid phase velocity profiles for simulations with different drag models and time step of 0.00015 s	81
5.32 Time-averaged solid volume fraction profiles for simulations with different drag models and time step of 0.00015 s	81
5.33 Time-averaged gas phase velocity profile for simulations with different models of radial distribution function and time step of 0.0001 s	82
5.34 Time-averaged solid phase velocity profile for simulations with different models of radial distribution function and time step of 0.0001 s	83
5.35 Time-averaged solid volume fraction profile for simulations with different models of radial distribution function and time step of 0.0001 s	84
5.36 Time-averaged solid volume fraction profile for simulations with different restitution coefficients and time steps	85

5.37	Time-averaged granular temperature profile for simulations with different restitution coefficients and time steps	86
5.38	Time-averaged gas phase velocity profile for simulations with different time steps	87
5.39	Time-averaged solid phase velocity profile for simulations with different time steps	87
5.40	Time-averaged solid volume fraction profile for simulations with different time steps	88
5.41	Time-averaged gas phase velocity profile comparison between L. Cabezas-Gomez et al. [10] and the current study	90
5.42	Time-averaged solid phase velocity profile comparison between L. Cabezas-Gomez et al. [10] and the current study	91
5.43	Time-averaged solid volume fraction profile comparison between L. Cabezas-Gomez et al. [10] and the current study	92
5.44	Time-averaged gas phase velocity profiles for laminar and turbulent simulation	93
5.45	Time-averaged solid phase velocity profiles for laminar and turbulent simulation	94
5.46	Time-averaged solid volume fraction profiles for laminar and turbulent simulation	95
5.47	Comparison of the solid velocity and the solid volume fraction distribution at time=40 s between turbulent and laminar simulation	96
5.48	A suggested wall boundary condition	97
6.1	Geometry and boundary conditions used in simulations	103
6.2	Domain meshing in y,z-plane	103
6.3	The highlighted position for capturing the solid phase velocity profiles	105
6.4	Time-averaged lateral profiles of the solid phase velocity at z=0.073 m and 0.1 m as shown by Figure 6.3	105
6.5	The highlighted position for capturing the gas volume fraction lateral profiles	106
6.6	Time-averaged lateral profiles of the gas volume fraction at x=7.06 m and 8.98 m as shown by Figure 6.5	106

List of Tables

1.1	Design parameters of BFB and CFB combustion system [37]	2
2.1	Comparison between Jackson's and Ishii's model	16
3.1	Model constants for $k - \epsilon$ turbulence model [40]	42
5.1	Simulation parameters of 3D gas-solid flow in cylindrical riser	58
6.1	Simulation parameters of 3D gas-solid flow in rectangular riser	102

Abstract

Fluidization process is widely used in commercial operation or industrial reactors. One of the reactor types which implement fluidization process is fluidized bed. The study of hydrodynamics behaviour of fluidized bed has been exercised for many years. By the development of advance numerical technique and high performance computing, computational fluid dynamics (CFD) become an important tools to analyse the gas-solid hydrodynamics behaviour. There are two different approaches in simulating gas-solid two phase flows, Two-Fluid Model (TFM) or Eulerian-Eulerian approach and Eulerian-Lagrangian approach. In this study, Two-Fluid Model alongside with the kinetic theory of granular flow (KTGF) is implemented into the developed CFD code, AIOLOS. AIOLOS is a CFD software which has been developed by Institut für Feuerungs- und Kraftwerkstechnik (IFK), Stuttgart University, Germany. It is originally dedicated for simulating pulverized coal combustion and solid fuel gasification. The solution algorithm used in the simulation is adopted from Syamlal et al. [69] with some modifications. For dealing with pressure-velocity coupling problem, the Semi-Implicit Method for Pressure Linked Equations (SIMPLE) is used. The $k - \epsilon$ turbulent model is used to calculate the gas phase turbulence viscosity.

The first test case in this study is based on the experiment of K.M. Luo [49]. The case is a 3D-cylindrical riser with height of 5.5 m and diameter of 0.076 m. Two different meshes with the number of cells of 168600 and 948480 are employed. The simulation was carried out at transient condition from 0-40 s with two different time step, namely 0.0001 and 0.00015 s. The simulation results from 30-40 s are time-averaged and its result is analysed and evaluated. Three different drag models, namely Wen-Yu model, Syamlal et al. model, and Gidaspow model, are employed to calculate the momentum transfer between gas and solid phases. The radial distribution function models proposed by Carnahan-Starling and Syamlal et al.

are utilized in the simulation. For the coefficient of restitution, two different values of 0.7 and 0.84 are set up. The inlet boundary condition is determined as a uniform inlet velocity and phase volume fraction for both gas and solid phase, i.e. $U_g = 4.979 \text{ m s}^{-1}$, $\varepsilon_g = 0.9754$, $U_m = 0.386 \text{ m s}^{-1}$, $\varepsilon_m = 0.0246$. The solid diameter, d_m , and the solid density, ρ_m , are $520 \mu\text{m}$ and 2620 kg m^{-3} , respectively. The zero gradient at outlet for any properties is set up as the outlet boundary condition. Furthermore for wall boundary conditions, no-slip boundary condition is utilized for both phases. Preliminary simulation shows that the standard mesh is more appropriate to be used for the simulation. For laminar flow simulation of the first test case, 13 combinations of the simulation parameter are simulated. Using drag model of Syamlal et al., restitution coefficient of 0.7, and radial distribution function of Syamlal et al., the simulation obtains the best agreement to the experimental data, either using time step of 0.0001 s or of 0.00015 s. Using this combination of the simulation parameter, the turbulent flow simulation achieves slightly a different result comparing with the laminar simulation.

The second test case is based on the experiments of J. Zhuo et al. [81]. The case is a 3D-rectangular riser with dimensions of $0.146 \times 0.146 \times 9.0 \text{ m}$. The computation grid consists of 146168 cells. The simulation was carried out at transient condition from 0-40 s with time step of 0.00015 s, Syamlal et al. drag model, the radial distribution function of Syamlal et al., and the restitution coefficient of 0.7. The inlet boundary condition is determined as a uniform inlet velocity and phase volume fraction for both gas and solid phase, i.e. $U_g = 5.5 \text{ m s}^{-1}$, $\varepsilon_g = 0.90$, $U_m = 0.1515 \text{ m s}^{-1}$, $\varepsilon_m = 0.10$. The solid diameter, d_m , and the solid density, ρ_m , are $213 \mu\text{m}$ and 2640 kg m^{-3} , respectively. The zero gradient at outlet for any properties is set up as the outlet boundary condition. Furthermore for wall boundary conditions, no-slip boundary condition is utilized for both phases. Examining the lateral profiles of the solid velocity and the gas volume fraction, the simulation result shows a poor agreement with the experiment.

In order to improve the results of the current simulation, the implementation of the Johnson and Jackson wall boundary condition and the energy minimization multi-scale (EMMS) drag model into the developed code are recommended. The use of a finer mesh and a parallel computer are also suggested to achieve a better result and an efficient and fast simulation.

Nomenclature

Abbreviations:

2D	Two dimensional
3D	Three dimensional
BFB	Bubbling fluidized bed
CFB	Circulating fluidized bed
CFD	Computational fluid dynamics
EE	Eulerian-Eulerian
EL	Eulerian-Lagrangian
FVM	Finite volume method
KE	Kinetic energy
TFM	Two-Fluid Method

Symbols:

c	Compacting modulus [-]
C_D	Coefficient of drag [-]
d_m	Solid particle diameter [m]
e_e	Coefficient of solid volume fraction correction [-]
e_m	Coefficient of restitution [-]
$g_{0,m}$	Radial distribution function [-]
g_i	Gravity in i-direction [m s^{-2}]
G	Solid phase elastic modulus [Pa]
G_o	Normalizing unit factor [Pa]
I_{2D}	Second invariant of the deviatoric stress tensor [s^{-2}]

I_{gm}	Interphase momentum transfer [$\text{kg m}^{-2} \text{s}^{-2}$]
k	Coefficient of granular energy diffusion [$\text{kg m}^{-1} \text{s}^{-1}$]
k_B	Boltzmann constant [$1.3805 \cdot 10^{-23} \text{ J K}^{-1}$]
m_g	Gas mass [kg]
P_g	Gas pressure [Pa]
P_m	Solid pressure [Pa]
P_f	Solid frictional pressure [Pa]
q_m	Solid mass flux [$\text{kg s}^{-1} \text{ m}^{-2}$]
Re	Reynolds number [-]
Re_m	Reynolds number for Syamlal and O'Brien drag model [-]
R	Universal gas constant [$286.9 \text{ J kg}^{-1} \text{ K}^{-1}$]
S_g	Gas strain-rate tensor [s^{-1}]
S_m	Solid strain-rate tensor [s^{-1}]
T	Time [s]
T_g	Gas temperature [$^{\circ} \text{C}$]
U_g	Gas velocity vector [m s^{-1}]
u'_g	Local random fluctuating gas velocity [m s^{-1}]
U_m	Solid velocity vector [m s^{-1}]
u_m	Local mean solid velocity [m s^{-1}]
u'_m	Local random fluctuating solid velocity [m s^{-1}]
U_{mf}	Minimum fluidization gas velocity [m s^{-1}]
$U_{m,t}$	Tangential solid velocity on the wall [m s^{-1}]
V	Volume [m^3]

Greek Letters:

β_{gm}	Momentum exchange coefficient [$\text{kg m}^{-3} \text{s}^{-1}$]
δ	Unit tensor [-]
γ	Coefficient of granular energy dissipation [$\text{kg m}^{-1} \text{s}^{-3}$]
μ_g	Gas viscosity [$\text{kg m}^{-1} \text{s}^{-1}$]
μ_m	Solid viscosity [$\text{kg m}^{-1} \text{s}^{-1}$]

μ_b	Solid bulk viscosity [$\text{kg m}^{-1} \text{s}^{-1}$]
μ_f	Solid frictional viscosity [$\text{kg m}^{-1} \text{s}^{-1}$]
μ_{mix}	Mixture viscosity [$\text{kg m}^{-1} \text{s}^{-1}$]
ϕ	Internal friction angle [$^\circ$]
ρ_g	Gas density [kg m^{-3}]
ρ_m	Solid density [kg m^{-3}]
θ_m	Granular temperature [$\text{m}^2 \text{s}^{-1}$]
τ_g	Gas phase stress tensor [N m^{-2}]
τ_m	Solid phase stress tensor [N m^{-2}]
ε_g	Gas volume fraction [-]
ε_g^*	Compacting gas phase volume fraction [-]
ε_m	Solid volume fraction [-]
ε_m^*	Maximum packing solid volume fraction [-]
φ	Specularity coefficient [-]
ζ	Coefficient of fluctuating energy exchange [$\text{kg m}^{-1} \text{s}^{-3}$]

1 Introduction

1.1 Fluidization and its Applications

Fluidization is a process in which the gas or liquid is blown upwards through a solid-filled column or reactor so that the solid part converts from a static solid-like state to a dynamic fluid-like state. Fluidization process is widely used in commercial operation or industrial reactors. One of the reactor types which implement fluidization process in their operation is fluidized beds. Due to its predominance, fluidized beds is the most widely used reactor in many industries, such as chemical, pharmaceutical, food, petroleum, and power-generation industries. Fluidized beds reactors have some advantages over other gas-solid reactor types. They provide large contact area between phases so that it enhances mixing of phases, chemical reactions, heat and mass transfer between gas and solids. Moreover, they are suitable for both large and small scale operation. One of the most prevalent applications of fluidized bed technology is combustion for heat generation. There are two types of fluidized bed combustion technologies which have been massively used for decades. They are Bubbling Fluidized Bed (BFB) and Circulating Fluidized Bed (CFB) combustion. Briefly, the technological comparison of BFB and CFB combustion is presented by table 1.1 [37].

The history of BFB development began at the first time as the BFB reactor was introduced by Fritz Winkler of Germany, December 16, 1921 [4]. He created the first demonstration of coal gasification in a fluidized bed as shown by Figure 1.1. The idea came when Winkler saw the solid particles lifted by the gas flow to be similar as a boiling liquid. This invention was then recognized as the concept of bubbling fluidized bed (BFB) process. The concept of BFB was then applied in many industrial processes, such as gasification, chemical, and combustion processes in the next periods. From 1926 till 1975, around 40 units of this type

Table 1.1: Design parameters of BFB and CFB combustion system [37]

Design parameter	BFB	CFB
Combustion temperature ($^{\circ}$ C)	760-780	800-900
Fuel particle size (mm)	0-50	0-25
Fluidization velocities (m/s)	1-3	3-10
Solid concentrations	High in bottom Low in freeboard	Gradually decreasing along furnace height
Solid circulations	No	Yes
Average steam parameters		
Steam flow (kg/s) (range)	36 (13-139)	60 (12-360)
Steam temperature ($^{\circ}$ C) (range)	466 (150-543)	506 (180-580)
Steam pressure (bar) (range)	72 (10-160)	103 (10-275)

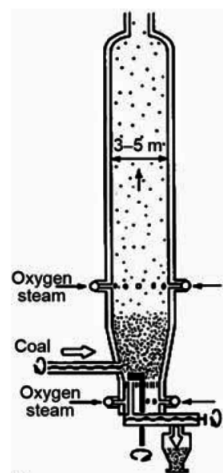


Figure 1.1: Winkler coal gasifier reactor [77]

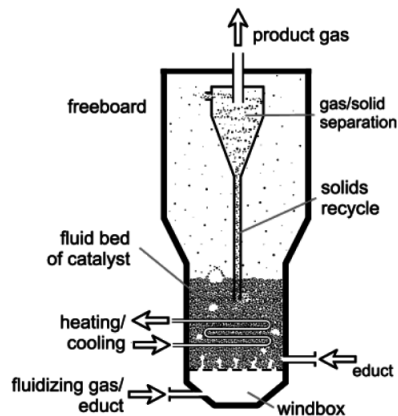


Figure 1.2: Bubbling fluidized bed schematic [75]

of reactor were built in Leuna, Germany for syngas production for the chemical industry. In the 1930s and 1940s, Germany developed BFB for coal gasification and metal refining applications. At the same time in the United States, the technology was developed for speeding the reaction of oil feedstock catalytic cracking in the petroleum industry. After World War II, the first development in utilizing fluidized beds for solid fuel combustion was made in the Soviet Union. The purposes of the development were for industrial boiler and residential-commercial (district) heating system. At the beginning of the 1960s, the British National Coal Board began a research on fluidized bed coal combustion in order to utilize a poor quality of solid fuels. The same development also occurred in the United States at the late of 1960s. It was then accelerated by the oil crises and the environmental regulation on gaseous emission for power-generating industry. Figure 1.2 shows the general arrangement of a BFB reactor.

When BFB introduction occurred at the first time in the 1920s, in the meanwhile CFB technology was proposed and became a patent in the 1940s [41]. In 1939 at the Massachusetts Institute of Technology, Warren Lewis and Edwin Gilliland developed a high-velocity fluidization process when they were trying to find an appropriate gas-solid contacting process for fluid catalytic cracking (FCC) [44]. Their invention was the first to propose a CFB reactor and patented [43]. They recognize a phenomenon of increasing on catalyst-bed reactor output when the fluidization velocity becomes higher than in a low-velocity bed reactor and a high solid mass flux into the reactor avoids empty space in the bed. This invention was

applied by Standard Oil for their fluid-bed catalytic cracker. The CFB concept for solid fuel combustion was initiated by Metallgesellschaft AG, a German company in the 1970s. They designed for the first time CFB of solid fuel combustion for calcination of aluminium hydroxide. The general layout of a CFB reactor is shown by Figure 1.3.

Since the fluidized beds combustion technology offers some advantages which are not provided by other combustion technology, such as fuel flexibility, low NO_x emission and efficient sulfur removal, the usage of BFB and CFB combustion has been increasing over the last decades [5]. The diversity and increase of fluidized beds application in industrial combustion have a consequence that the fluidized beds boiler development is necessary in order to enhance the efficiency of combustion process. Dealing with that need, the experimental techniques and advanced numerical simulation methods come to play an important role as design tools for high-efficiency fluidized bed reactors. The efficiency of fluidized beds reactor/combustion depends on the hydrodynamics behaviour of both phases inside the reactor. Therefore, the study of hydrodynamics behaviour of fluidized bed has been exercised for many years. The complexity of hydrodynamics in fluidized beds such as the interaction between phases, mixing patterns, and particles distribution induces a complication to the experimental techniques in predicting the hydrodynamics phenomena inside the reactor. Furthermore, in order to achieve a detailed analysis of hydrodynamics phenomena using the experimental techniques, varying the numbers of experimental parameters (such as gas velocity, particle diameter and density, reactor geometry etc.) is a mandatory. This variation generates a highly cost-demanding experiment. Moreover, the experimental techniques have a limitedness in capturing the complex hydrodynamics phenomena in the fluidized beds such as solid particles cluster and distribution.

Regarding the shortage of the experimental techniques in predicting the gas-solid hydrodynamics, the numerical simulation method comes to handle it. In the past decades, many researchers have shown that numerical simulation methods have great potential to be employed in studying gas-solid hydrodynamics in fluidized beds [26]. By the development of advanced numerical techniques and high performance computing, Computational Fluid Dynamics (CFD) became an important tool to analyse the gas-solid hydrodynamics. Numbers of information which are hard to obtain using experimental techniques are easily esti-

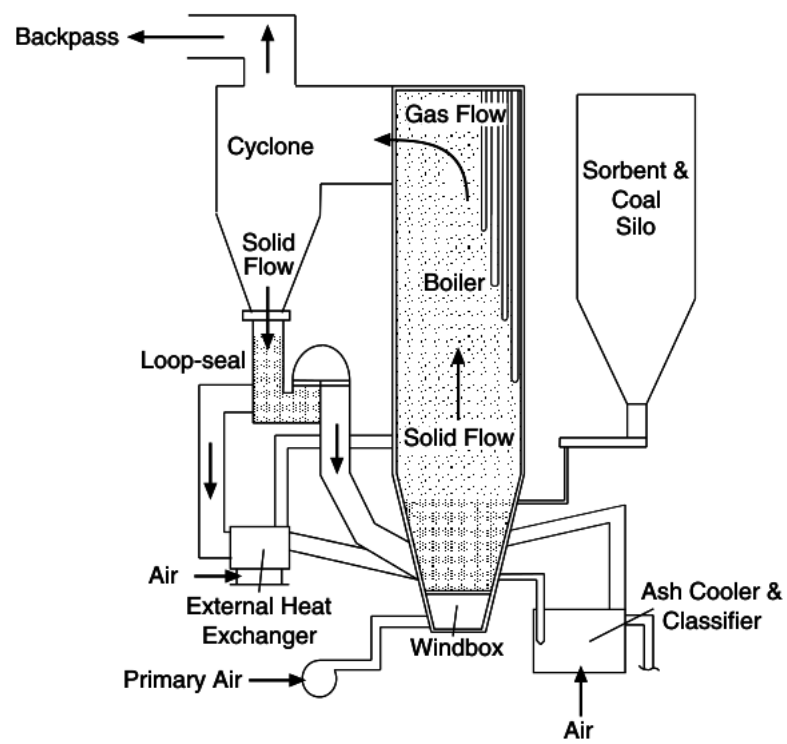


Figure 1.3: Circulating fluidized bed schematic [4]

mated using CFD tools. Moreover, some detailed data profiles as a function of space and time could be obtained by CFD tools without interfering the flow by internal probes. However, in spite of helping so significantly in understanding the hydrodynamics behaviour, the accuracy of CFD models must be validated using experimental studies.

Concerning the previous descriptions about the basics of fluidization, the application in the combustion process, and the important role of CFD in improving the performance or efficiency of fluidized bed reactors, there is a motivation to develop the capability of the in-house CFD code owned by Institut für Feuerungs- und Kraftwerkstechnik (IFK), called AIOLOS, for simulating gas-solid two phase flow problems with combustion process. AIOLOS is a CFD software dedicated for simulating pulverized coal combustion and solid fuel gasification from small-scale to full-scale industrial furnaces or boilers. The Finite Volume Method (FVM) is the basis of numerical method utilized by the software, and the Fortran language is used for building the software. The AIOLOS code consists of several packages which are able to solve hydrodynamics, chemical reactions, heat and mass transfers, and radiation problems. Nevertheless, the original AIOLOS software has not been able to simulate fluidized bed combustion processes such as BFB or CFB boilers yet. Beholding the important role of CFD in developing high-efficiency fluidized bed combustion, it is a challenging idea and task to develop the code for simulating fluidized bed combustion reactors like BFB and CFB boilers. The development result, of course, will be very beneficial for the code stakeholders.

However, the combustion process in fluidized bed reactors is a very complicated problem. It is an involute gas-solid two phase hydrodynamics phenomenon with chemical reaction, heat and mass transfer, and radiation processes. Thus, in order to achieve the ultimate goal as mentioned in the previous paragraph, the code development should be done gradually. The code development starts from the fundamental gas-solid two phase flow problem, it is the hydrodynamics of gas-solid two phase flow in a riser. In other words, the first step of AIOLOS development for dealing with gas-solid two phase flow problems is to solve a dilute gas-solid two phase flow in a riser. This task becomes the focus of the current thesis research. Subsequent to dealing with this, the next parts on fluidized bed combustion processes like chemical reaction, heat and mass transfer etc. could be solved.

1.2 Research Objective

The objective of this research is to implement the Eulerian-Eulerian (EE) approach or Two-Fluid Method (TFM) to CFD software, called AIOLOS, for simulating gas-solid two phase flow in a riser. The developed AIOLOS is then tested to predict the hydrodynamics behaviour of gas-solid flow in a three dimensional cylindrical and a three dimensional rectangular riser at transient conditions. Afterwards, in order to validate the accuracy of the developed code, the time-averaged simulation results are compared to the empirical results which are obtained by experiments of another researcher.

1.3 Thesis Outline

The thesis is compiled into seven chapters. Chapter 1 concerns on introduction to fluidization and its applications. It discusses the role of fluidization in industrial operations like combustion. Chapter 2 covers the mechanism of gas-solid flows in riser and the numerical approaches for modelling gas-solid multiphase flows. By examining the physical behaviour of gas-solid flows, researches derived the computational method used to solve gas-solid flow problem into two streams, Eulerian-Eulerian or Two-Fluid Method and Eulerian-Lagrangian approaches. The advantages and weaknesses of both methods are shortly discussed. Then the development of the Two-Fluid Model which is used in this work is briefly reviewed. Chapter 3 discusses the governing equations of the Two-Fluid Model. The constitutive equations of the governing equations are derived either using constant variable approach or using kinetic theory of granular flows. The basic concept of the kinetic theory of granular flows and its implementations are explained. A brief overview of the in-house software developed by Institut für Feuerungs- und Kraftwerkstechnik (IFK) Stuttgart University called AIOLOS is presented. The Two-Fluid Model is implemented into AIOLOS in order to simulate gas-solid flows in a riser. Chapter 4 explains the numerical solution procedure such as the solution algorithm and numerical schemes or parameters for the simulation. Chapter 5 discusses the simulation results of gas-solid flow in a 3D-cylindrical riser. The discussion of the results with respect to three different drag models, two different radial distribution function models, two different values of restitution coefficient will take place.

Chapter 6 discusses the simulation result of gas-solid flow in a 3D-rectangular riser. The result is obtained by a simulation with the parameter combination of Syamlal et al. drag model, Syamlal et al. radial distribution function model, and restitution coefficient of 0.7. Chapter 7 is about conclusions, outlook, and some recommendations for the next researchers who are willing to utilize AIOLOS for simulating gas-solid multiphase flows.

2 Gas-Solid Two Phase Flow

2.1 Mechanism of Gas-Solid Riser Flow

Once the solid particles are fluidized, its flow behaviour in fluidized beds is strongly influenced by the gas and solid properties such as velocity, density, and solid diameter. By empirical observation, there are numbers of fluidization regimes as shown in Figure 2.1. As the low velocity gas flow introduces through the solid bed, it flows upwards and occupies the empty spaces between solid particles. When this flow is maintained continuously, the solid particles in the bed will vibrate but still stay in the same position as the bed at rest. At low velocity gas flow, the drag force exerted on each solid particle is very small, thus the particle will be motionless. This condition is called fixed bed as shown by Figure 2.1.A. By increasing the gas velocity, the solid bed expanding slightly (increasing of the bed voidage, Figure 2.1.B) is observed once the drag force of the particle equals the gravitational force of the particle. This situation is the onset of fluidization and is named as minimum fluidization with respect to a minimum fluidization velocity, $U_{f,min}$. As the gas velocity further increases, the bubbles are arised in the solid beds and the formation of bubbling fluidization takes place as shown in Figure 2.1.C. At this state, it is called bubbling fluidized bed. When the gas velocity keeps on increasing, coalescing and growing bubbles occur as they rise in a bubbling fluidized bed. If the ratio of the height to the diameter of the bed is high enough, the bubbles sizes tend to the same as the bed diameter. At this point, it is labelled as slugging (Figure 2.1.D). If the particles are fluidized at a high enough gas flow rate, the particle velocity transcends the terminal velocity of the particles. It leads to the upper surface of the bed and then various sizes and shapes of turbulent motion of solid clusters and voidages. This state is named as turbulent beds as shown by Figure 2.1.E. Maintaining the increasing of gas velocity, the fluidized beds become dilute, the solid particles move upwards very fast

and the pneumatic solid transport occurs (Figure 2.1.F).

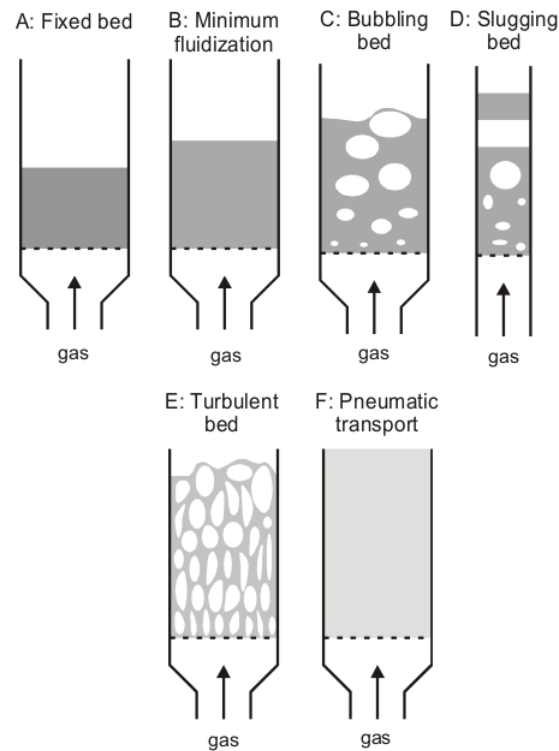


Figure 2.1: Fluidized beds in different regimes [39]

The utilization of solid particle movement in industrial fluidized bed processes demands the understanding of its characteristics. The behaviour of the particles in fluidized beds depends on their size and density. One of the most useful methods to determine the particle behaviours is by assigning a generalized map for particle behaviour. Derek Geldart was the first to classify particle behaviour in fluidized bed by gases [24]. The Geldart's classification specifies particles based on the particle and gas density difference and mean particle size as shown by Figure 2.2. Using Geldart's classification, all particles are classified into four groups; A, B, C, and D, and it became the standard to circumscribe the fluidization types.

The characteristics of Geldart's groups of particles are explained briefly as follows :

1. Group A. The particles have small mean particle size, $d_m < 30 \mu\text{m}$ and or low particle density, $\rho_m < 1.4 \text{ g cm}^{-3}$. At low gas velocities, the particles fluidize easily and smoothly without the bubble formation. At higher gas velocities, once the bubble for-

mations take place in fluidized beds the minimum bubbling velocity is always greater than the minimum fluidization velocity, $U_{f,min}$. Typically, fluid cracking catalysts are in this category.

2. Group B. This group is called 'sandlike' or bubbly particles. The particles have sizes between $150 \mu\text{m}$ and $500 \mu\text{m}$ and their density is from 1.4 to 4 g cm^{-3} . The bubble formations occur once the minimum fluidization velocity is exceeded and they might grow to a large size. Glass beads and coarse sand typically are categorized to this group.
3. Group C. This bed particles are cohesive and very fine particles. They are very difficult to fluidize due to large interparticle forces. Talc and flour are two examples of this category.
4. Group D. It is called 'spoutable' particles. They are either very dense or very large in size so that it is difficult to fluidize them. Once a high gas velocity introduces to the solid bed, a jet flow might be formed in the bed and particles can be blown out following the jet flow in a spouting motion. Some examples of this group are roasting coffee and metal ores.

The fluidization process of different fluidization regimes for different groups of Geldart particles classification is summarized by Figure 2.3 [39].

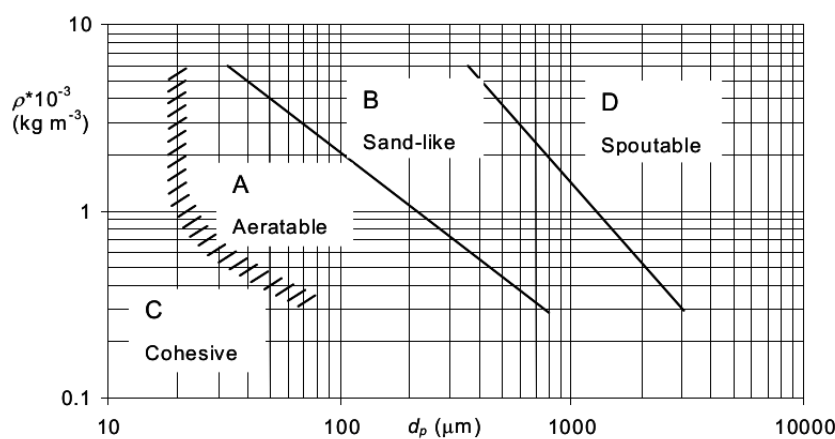


Figure 2.2: The Geldart particles classification diagram [24]

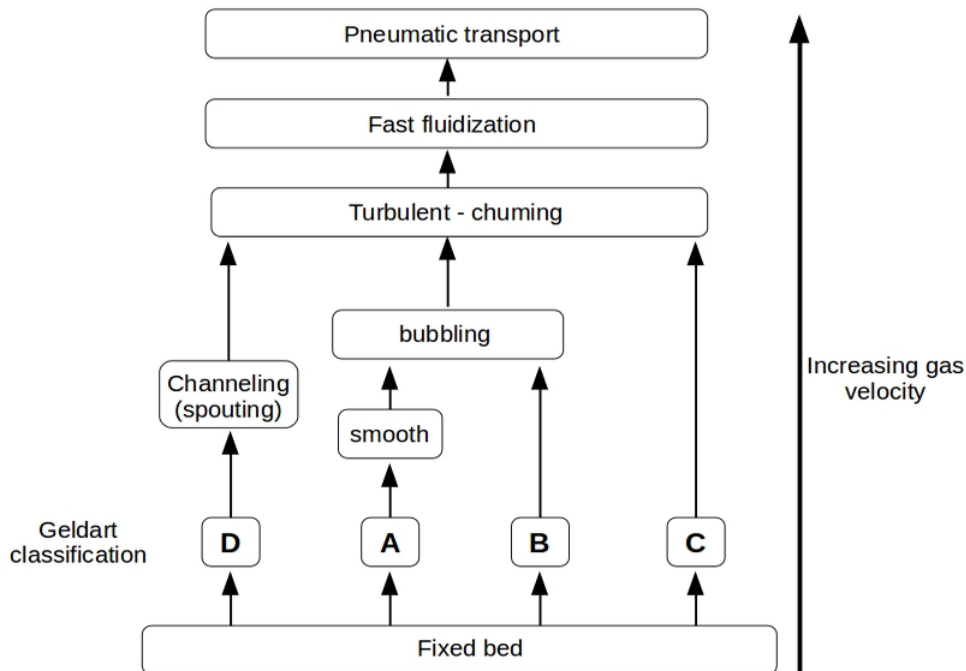


Figure 2.3: Fluidization process of different groups of Geldart particles

2.2 Computational Methods of Gas-Solid Two Phase Flow

There are two different approaches on simulating gas-solid two phase flows. They are Eulerian-Eulerian approach or Two-Fluid Model and Eulerian-Lagrangian approach. In both approaches, the gas phase is treated as a continuum phase. The difference between Eulerian-Eulerian and Eulerian-Lagrangian approach is how the model treats the solid phase. The Eulerian-Eulerian approach treats the solid phase as a continuum, therefore both phases (gas-solid) are interpenetrating phases and they are characterized by their own continuum equation of motion. The Eulerian-Lagrangian approach treats the solid phase at particle level and Newton's laws are applied to describe the motion of every single particle of the solid phase. Using the Eulerian-Lagrangian approach the trajectory of every single particle of the solid phase can be tracked.

Comparing these two different approaches, the Eulerian-Lagrangian approach is more demanding on computation resources than the Eulerian-Eulerian approach. An intensive computation requirement in using Eulerian-Lagrangian approach due to Newton's laws must be

solved for a single solid particle. Hence, the Eulerian-Lagrangian approach is highly time consuming when it is used for a system with a large number of particles. Generally, the Eulerian-Lagrangian model is used for systems containing less than 100,000 particles and some instantaneous interaction between particles have to be taken into account [73]. The Eulerian-Lagrangian approach has been utilized successfully for simulating dilute gas-solid flows with less particle collisions such as those in pulverized coal boilers, cyclone separators and spray dryers [66]. Whereas the Eulerian-Eulerian approach is usually used for a system of large size in which there is no need to take into detail up to particle level for the hydrodynamics behaviour of fluidized bed. This model becomes appropriate to the case where the solid particles loading is high and to the practical interest simulation due to its lower computational effort. In this research, the Eulerian-Eulerian approach or Two-Fluid Model will be implemented into the developed CFD code, called AIOLOS.

2.3 The Development of the Two-Fluid Model

Anderson and Jackson [2] and Ishii [29] are attributed by most researchers as the pioneers for introducing the governing equations of the Two-Fluid Model of gas-solid two phase flow. The mathematical model derivation for the Two-Fluid Model by Anderson and Jackson [2], Jackson [31], and Ishii [29] was based on the averaging of a local instantaneous of the equations of motion of a single solid particle and the Navier-Stokes equations for fluid motion over a region. This region contains many solid particles but it is much larger than the solid diameter and by far smaller than the characteristic length of the calculated domain. The original and detailed explanation of the mathematical model derivation could be found in their paper work. A review work of Two-Fluid Model for fluidization application by Enwald et al. [20] is also a good recommendation for the reader.

The averaging procedure which is the fundamental concept in the Two-Fluid Model is presented briefly by Figure 2.4. The left picture of Figure 2.4 is prior to the averaging procedure in which the gas phase is described by the instantaneous conservation equation of continuity and the Navier-Stokes equations, while the discrete solid phase motions are expressed by Newtonian equations. Theoretically, by using a numerical mesh smaller than the smallest

length scale of the flow and a time step smaller than the time scale of the fastest flow fluctuations, both conservation equations for gas phase and discrete equation for solid phase could be solved by direct numerical simulation. Though using the latest computer technology the direct numerical simulation might be possible, but it will not be efficient and not be profitable due to high demands in terms of time and computer resources. Thus, the averaging procedure is the solution for this problem. The right picture of Figure 2.4 is following this procedure.

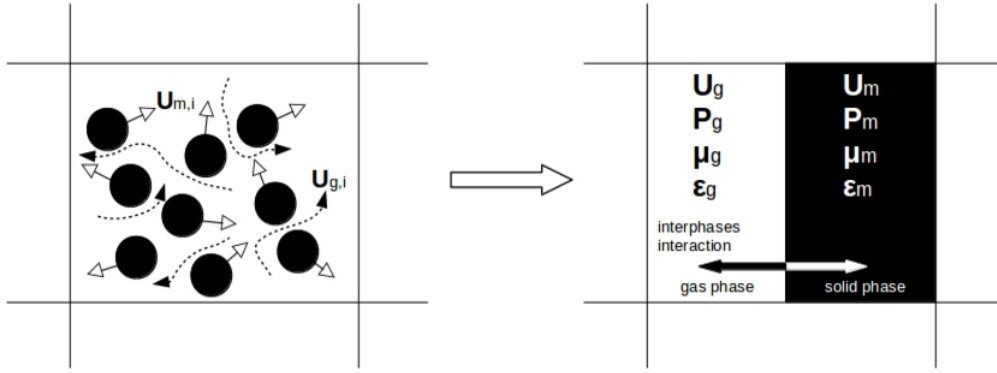


Figure 2.4: Two-Fluid Model concept for gas-solid flows

In Two-Fluid Model approach, a specified parameter which can be a scalar, or vector, is defined by the equation, $f = f(r, t)$, where r is a fixed point in space and t is time. The volume averaging is carried out around a fixed point r at time t and defined as:

$$\langle f(r, t) \rangle_V = \frac{1}{V} \int_V f(r, t) dx dy dz \quad (2.1)$$

According to Whitaker [76], the conditions under which the procedure of the volume averaging can be implemented, namely:

the phase characteristic dimension \ll the averaging volume characteristic dimension

the phase characteristic dimension \ll the physical system characteristic dimension.

While the time averaging is defined as follows:

$$\langle f(r, t) \rangle_t = \frac{1}{T} \int_{t-T/2}^{t+T/2} f(r, t) d\tau \quad (2.2)$$

Delhaye and Achard [17] give the satisfied conditions such that the time averaging can be applied with the chosen time interval as follows:

$$\begin{aligned} & \text{the turbulent fluctuations time scale} \ll \text{the averaging time scale} \\ & \text{the turbulent fluctuations time scale} \ll \text{the mean flow fluctuations time scale.} \end{aligned}$$

As mentioned before that Anderson and Jackson [2] and Ishii [29] are attributed as the pioneers for introducing the governing equations of the Two-Fluid Model of gas-solid two phase flow. The comparison of Jackson's model [31] and Ishii's model [29] was performed by van Wachem et al. [72]. There are two differences between Ishii's and Jackson's Two-Fluid Model. In the momentum equation of the solid phase, the solid volume fraction multiplied by the gradient of the total stress tensor of the gas phase is included in Jackson's model. Whilst Ishii's model only includes the solid volume fraction multiplied by the gradient of gas pressure into the momentum equation of the solid phase. In the momentum equation of the gas phase, Ishii's model places the gas volume fraction outside of the pressure gradient operator and inside of the shear stress gradient operator. Whereas in Jackson's model both pressure and shear stress are treated equally where the gas volume fraction is assigned outside of the gradient operators. Van Wachem et al. concluded that Jackson's model is more suitable for the gas-solid two phase problem, whereas the developed model by Ishii is more appropriate for gas-liquid two phase flow [72]. These two models are listed in Table 2.1. From Equations that are listed in Table 2.1, ρ is density, ε is volume fraction, τ is stress tensor, U is velocity, P_g is gas pressure, g is gravity, P_m is solid pressure, and I_{gm} is momentum transfer between gas and solid phases. The indices g and m represent the gas and solid phase, respectively. While the indices i and j are both from 1 to 3 which denote the coordinate directions for x, y, and z directions.

The averaging procedure in deriving the governing equations of the Two-Fluid Model, as proposed by Anderson-Jackson and Ishii, leads to such closure problems which must be completed in order to solve the governing equations of the Two-Fluid Model. The closure

Table 2.1: Comparison between Jackson's and Ishii's model

Jackson model [31]

Momentum equation for gas phase :

$$\frac{\partial}{\partial t} (\epsilon_g \rho_g U_{gi}) + \frac{\partial}{\partial x_j} (\epsilon_g \rho_g U_{gj} U_{gi}) = -\epsilon_g \frac{\partial P_g}{\partial x_i} + \epsilon_g \frac{\partial \tau_{gij}}{\partial x_j} - I_{gmi} + \epsilon_g \rho_g g_i \quad (2.3)$$

Momentum equation for solid phase :

$$\frac{\partial}{\partial t} (\epsilon_m \rho_m U_{mi}) + \frac{\partial}{\partial x_j} (\epsilon_m \rho_m U_{mj} U_{mi}) = \epsilon_m \frac{\partial \tau_{gij}}{\partial x_j} - \frac{\partial P_m}{\partial x_i} - \epsilon_m \frac{\partial P_g}{\partial x_i} + \frac{\partial \tau_{mij}}{\partial x_j} + I_{gmi} + \epsilon_m \rho_m g_i \quad (2.4)$$

Ishii model [29]

Momentum equation for gas phase :

$$\frac{\partial}{\partial t} (\epsilon_g \rho_g U_{gi}) + \frac{\partial}{\partial x_j} (\epsilon_g \rho_g U_{gj} U_{gi}) = -\epsilon_g \frac{\partial P_g}{\partial x_i} + \frac{\partial \epsilon_g \tau_{gij}}{\partial x_j} - I_{gmi} + \epsilon_g \rho_g g_i \quad (2.5)$$

Momentum equation for solid phase :

$$\frac{\partial}{\partial t} (\epsilon_m \rho_m U_{mi}) + \frac{\partial}{\partial x_j} (\epsilon_m \rho_m U_{mj} U_{mi}) = -\epsilon_m \frac{\partial P_g}{\partial x_i} + \frac{\partial \epsilon_m \tau_{mij}}{\partial x_j} + I_{gmi} + \epsilon_m \rho_m g_i \quad (2.6)$$

problems include the constitutive relations for each phase and the interactions between interpenetrating phases (momentum transfer between gas and solid phases). Another consequence of this averaging procedure is the information loss at the scale of the solid particle diameter due to the used region/volume/area in the averaging procedure which is by far larger than the solid particle size.

The governing equations of the Two-Fluid Model need constitutive laws to close the system due to several unknown terms arise in the equations. The models of unknown terms are called the constitutive equations which basically relate the physical parameters of a phase and describe how gas and solid interact with each other. For the solid phase, the important flow parameters which represent the rheology of the solid phase are solid viscosity, μ_m , solid bulk viscosity, μ_b , and solid pressure, P_m . These flow parameters of the solid phase depend strongly on the behaviours of local solid phase such as solid volume fraction, ε_m , solid translation and collision. The complexity of the local behaviours of the solid phase causes difficulties to determine these flow parameters.

In the literature, there are two different ways of modelling the important flow parameters of the solid phase as mentioned before. The first approach is by assuming the flow parameter as a constant or by using an empirical model based on the solid properties and local solid volume fraction. The constant value of the flow parameter is obtained by several experiments and empirical correlations. In the early development of the Two-Fluid Model, several researchers had applied this approach. Different researchers utilized different methods to calculate solid viscosity and solid shear stress which govern the tangential forces in solid particle aggregation. In order to calculate the solid viscosity, Enwald et al. employed a linear relationship of a mixture viscosity, μ_{mix} , as shown by Equation 2.7 [20].

$$\mu_m = \frac{\mu_{mix} - \mu_g \varepsilon_g}{1 - \varepsilon_g} \quad (2.7)$$

Once the mixture viscosity is obtained, the solid viscosity could be calculated. There are several models proposed to determine the mixture viscosity, two of them are the models proposed by Einstein and Ishii. Einstein's model for calculating the mixture viscosity, μ_{mix} ,

is expressed as Equation 2.8 [19]:

$$\mu_{mix} = \mu_g(1 + 2.5\varepsilon_m) \quad (2.8)$$

While Ishii model is shown by Equation 2.9. [30]:

$$\mu_{mix} = \mu_g \left(1 - \frac{\varepsilon_m}{\varepsilon_m^*}\right)^{-2.5\varepsilon_m^* \frac{\mu_m + 0.4\mu_g}{\mu_m + \mu_g}} \quad (2.9)$$

In their work on computing the flow patterns in circulating fluidized beds, Tsuo and Gidaspow used a constant for the solid viscosity value [71]. For 520 and 76 μm solid particles, the constant solid viscosities which based on measurements in circulating fluidized beds are 0.509 and 0.724 Pa.s, respectively.

Whereas solid viscosity and solid shear stress govern the tangential force in the solid particles, solid pressure contributes on the normal stress working on the surface of solid particles. When individual solid particles impact each other either by short-duration collision or long-duration contact, then the solid particles transmit such a force on the normal direction of their surfaces. These events originate the arising of the solid pressure [11]. Campbell and Wang measured the solid pressure in a bubbling fluidized bed and the sketch of the acquired solid pressure is shown by Figure 2.5. Observed from the figure, the solid pressure decreases with the increasing superficial gas velocity until the minimum fluidization gas velocity, U_{mf} , is reached. The decreasing of the solid pressure is caused by the increasing of drag force working on the solid particles which mitigates the long-duration contact between solid particles. When the gas velocity keeps increasing, the bed is expanded by the gas momentum and the particle's contacts lose their role. The further increasing of gas velocity beyond the minimum fluidization gas velocity leads to the increasing of the solid pressure due to the increasing in the solid particle's collisions.

In the first approach of determining the flow parameters by a constant or such an empirical model, researchers introduced some models in order to obtain the solid pressure. One of the models is proposed by Kuiper et al. [38]. They used an empirical equation to calculate the

gradient of solid pressure as follows [38]:

$$\frac{\partial P_m}{\partial x_i} = G(\varepsilon_g) \frac{\partial \varepsilon_g}{\partial x_i} \quad (2.10)$$

Based on the correlation by Bouillard et al., the generalized solid phase elastic modulus, $G(\varepsilon_g)$, is calculated as [9]:

$$G(\varepsilon_g) = -G_o \{ \exp[c(\varepsilon_g^* - \varepsilon_g)] \} \quad (2.11)$$

In their model, Kuipers et al. set up the value of the normalizing unit factor, $G_o = 1Pa$; the compacting modulus, $c = 100$; and the compacting gas phase volume fraction, $\varepsilon_g^* = 0.45$ [38]. In another way, the equation of the generalized solid phase elastic modulus, Equation 2.11, can be expressed as a function of the solid volume fraction, ε_m , as follows:

$$G(\varepsilon_m) = -G_o \{ \exp[c(\varepsilon_m - \varepsilon_m^*)] \} \quad (2.12)$$

where $\varepsilon_m^* = 0.55$ is the maximum packing limit of the solid volume fraction.

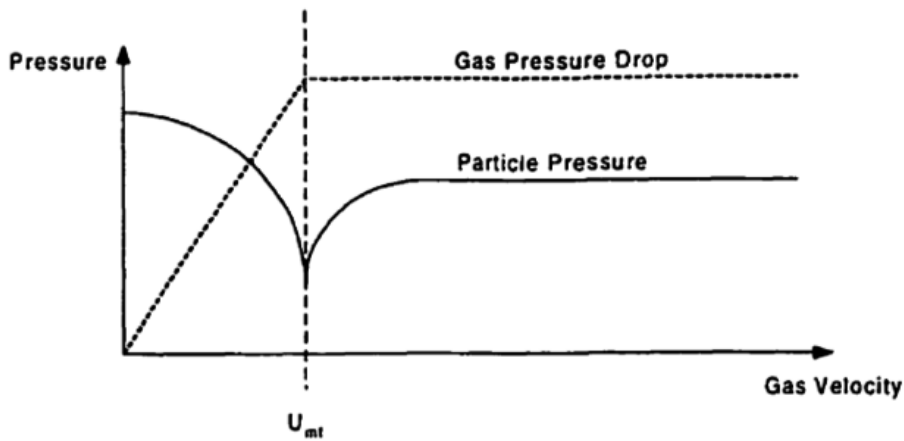


Figure 2.5: Sketch of solid pressure profile in fluidized beds [11]

The above references are some of many works which were dedicated to obtain the flow parameters of the solid phase using the first approach. The advantage of the first approach is

its simplicity such that it is very easy to be implemented into computer code and less demanding in computation time. Due to its simplicity, this approach is not able to explain the rheology behaviour of the solid phase clearly, for instance the effects of particle's collisions.

The second approach for determining the flow parameters of the solid phase is by using the kinetic theory of granular flow (KTGF). Basically, the kinetic theory of granular flow relies on the classical kinetic theory of gases by Chapman and Cowling [14]. The motion of the solid particle in the gas-solid multiphase flow could be analogous to the motion of the gas molecules. By using the kinetic theory of granular flow, the rheology behaviour of the solid phase could be explained by more fundamental aspects such as the particle-particle interaction (collisions) and particle-wall interaction. A more detailed explanation of the kinetic theory of granular flow will be discussed in Chapter 3.

The work on the kinetic theory of granular flow was firstly started by Savage and Jeffrey [59]. Jenkins and Savage [33], Lun et al. [48] and Johnson and Jackson [35] continued the development of this approach. Sinclair and Jackson first applied the kinetic theory of granular flow to calculate a fully-developed gas-solid flow in a vertical pipe with solid particles interaction [64]. Ding and Gidaspow developed the model to calculate solid viscosity and solid pressure for dense gas-solid flows based on kinetic theory and applied the model to simulate a bubbling fluidized bed. The model obtained a good agreement to the experimentally measured time-averaged solid volume fraction in two-dimensional fluidized bed. Using uniform inlet gas velocity, it predicted the bubbles formation and solids flow pattern in agreement with measurement and observations [18]. Nieuwland et al. simulated two-dimensional gas-solid flow in a circulating fluidized bed using their model which is based on the kinetic theory of granular flow. The simulation results showed a satisfactory agreement with experimental data, though the model slightly underpredicts the solids phase segregation and tends to an axial solid velocity profile with a more parabolic slope in comparison with the experimental data [51].

Comparing those two different ways of modelling the flow parameters of the solid phase, the kinetic theory of granular flow is more powerful than the constant value or empirical model approach. The kinetic theory of granular flow is applicable to cover a wide range of

problems and gives a fundamental analysis on the rheology behaviour of the solid phase. In their publications, Patil et al. [56] and Johnson et al. [34] explained that the simulation results using the kinetic theory of granular flow obtained a much better agreement to the experimental results than the results obtained by using the constant value or empirical model approach. In the present work, the kinetic theory of granular flow will be implemented in developing a computational fluid dynamics software which is dedicated to simulate gas-solid two-phase flow in the riser of circulating fluidized beds.

3 Two-Fluid Model for Gas-Solid Riser Flow

3.1 The Governing Equations of Two-Fluid Model

As described in Section 2, a set of governing equations for describing gas-solid two phase flow is derived by averaging of a local instantaneous of the equations of motion of a single solid particle and the Navier-Stokes equations for fluid motion over a region. As the result, a set of Navier Stokes equations for both phases will be solved numerically in order to simulate gas-solid two phase flows. By assuming the simulated system is isothermal, there is no mass transfer between gas and solid phases, the solid particles are mono-sized and perfectly spherical, the Navier-Stokes equations consist of the conservation equation of mass and momentum for both phases.

The conservation equations of mass for both phases are presented below.

Conservation of mass for gas phase :

$$\frac{\partial}{\partial t} (\varepsilon_g \rho_g) + \frac{\partial}{\partial x_i} (\varepsilon_g \rho_g U_{gi}) = 0 \quad (3.1)$$

Conservation of mass for solid phase :

$$\frac{\partial}{\partial t} (\varepsilon_m \rho_m) + \frac{\partial}{\partial x_i} (\varepsilon_m \rho_m U_{mi}) = 0 \quad (3.2)$$

Volume fractions comply with :

$$\varepsilon_g + \varepsilon_m = 1 \quad (3.3)$$

While the conservation equations of momentum for both phases are listed below.

Conservation of momentum for gas phase :

$$\frac{\partial}{\partial t} (\varepsilon_g \rho_g U_{gi}) + \frac{\partial}{\partial x_j} (\varepsilon_g \rho_g U_{gj} U_{gi}) = -\varepsilon_g \frac{\partial P_g}{\partial x_i} + \frac{\partial \tau_{gij}}{\partial x_j} - I_{gmi} + \varepsilon_g \rho_g g_i \quad (3.4)$$

Conservation of momentum for solid phase :

$$\frac{\partial}{\partial t} (\varepsilon_m \rho_m U_{mi}) + \frac{\partial}{\partial x_j} (\varepsilon_m \rho_m U_{mj} U_{mi}) = -\frac{\partial P_m}{\partial x_i} - \varepsilon_m \frac{\partial P_g}{\partial x_i} + \frac{\partial \tau_{mij}}{\partial x_j} + I_{gmi} + \varepsilon_m \rho_m g_i \quad (3.5)$$

From Equations 3.1 to Equation 3.5, ρ is density, ε is volume fraction, τ is stress tensor, U is velocity, P_g is gas pressure, g is gravity, P_m is solid pressure, and I_{gm} is momentum transfer between gas and solid phases. The indices g and m represent the gas and solid phase, respectively. While the indices i and j are both from 1 to 3 which denote the coordinate directions for x, y, and z directions. The conservation of momentum for both phases shows that the left two terms represent the force per unit volume due to the acceleration of the phase. The force per unit volume in the left side of the equations is balanced by the force per unit volume in the right side which consists of normal force by pressure, tangential force by viscosity, body force by gravity and interphase force by momentum transfer between the two phases.

3.2 The Constitutive Equations

In order to solve the set of equations presented in the previous section, Section 3.1, there are several unknown terms which should be determined by appropriate models. These models of unknown terms are called constitutive equations which relate the physical parameters of a phase and which describe how gas and solid interact with each other. The constitutive equations used in this study refer to Benyahia et al. [8].

3.2.1 Viscous Stress Tensor for gas phase

By assuming the flow is incompressible, the gas phase stress tensor is obtained from the classical Newtonian stress-strain relation as:

$$\tau_{gij} = 2\mu_g S_{gij} \quad (3.6)$$

in which the gas strain-rate tensor is defined by

$$S_{gij} = \frac{1}{2} \left[\frac{\partial U_{gi}}{\partial x_j} + \frac{\partial U_{gj}}{\partial x_i} \right] - \frac{1}{3} \frac{\partial U_{gi}}{\partial x_i} \delta_{ij} \quad (3.7)$$

The gas phase viscosity in Equation 3.6 is usually set to a constant value.

3.2.2 Viscous Stress Tensor for solid phase

Similar to the gas phase, the solid phase stress tensor is derived from the Newtonian stress-strain relation. The stress tensor expression for the solid phase as follows:

$$\tau_{mij} = \left[n\mu_b \frac{\partial U_{mi}}{\partial x_i} \right] \delta_{ij} + 2\mu_m S_{mij} \quad (3.8)$$

where the solid strain-rate is

$$S_{mij} = \frac{1}{2} \left[\frac{\partial U_{mi}}{\partial x_j} + \frac{\partial U_{mj}}{\partial x_i} \right] - \frac{1}{3} \frac{\partial U_{mi}}{\partial x_i} \delta_{ij} \quad (3.9)$$

Comparing the stress tensor expression between the gas phase, Equation 3.6, and the solid phase, Equation 3.8, there is a difference between them. For the gas phase, the contribution of the gas bulk viscosity on the gas stress tensor is ignored, in accordance with Stokes' assumption, e.g. Panton [54]. Practically, the lack of reliable measurement techniques is the reason for neglecting the bulk viscosity [20]. Nevertheless, the solid bulk viscosity, μ_b , is accounted for its contribution on the stress tensor of the solid phase and is determined theoretically using the kinetic theory of granular flow. While the notation of n in Equation 3.8 will be explained in Chapter 3.2.5.

For the solid phase stress tensor (Equation 3.8), several physical solid phase properties are needed to be determined. These properties (transport variable properties) refer to solid viscosity, μ_m , and solid bulk viscosity, μ_b . In order to determine these properties, also for solid

pressure, there are two different approaches that could be employed as discussed in Section 2.3. The first approach is assuming the variables as a constant and the second approach is by using the kinetic theory of granular flow (KTGF). A detailed explanation of the kinetic theory of granular flow will be presented in Chapter 3.2.5.

3.2.3 Pressure for gas phase

The gas pressure is set equal to the static pressure. It can be calculated by using the Ideal Gas law as below.

$$P_g = \rho_g RT_g \quad (3.10)$$

3.2.4 Interphase Momentum Transfer

In the Two-Fluid Model for gas-solid two phase flow, the interaction between gas and solid phases is presented by the interphase force per unit volume or interphase momentum transfer which is expressed by an momentum exchange coefficient, β_{gm} , multiplied by the relative velocity between gas and solid phases:

$$I_{gmi} = \beta_{gm}(U_{gi} - U_{mi}) \quad (3.11)$$

The momentum exchange coefficient may be contributed by four different forces: Basset force, lift force, added mass force, and drag force. The Basset force arises from the diffusion of vorticity away from the solid particle when the solid particle changes its velocity. When the flow is non-uniform or having a velocity gradient and if the particle is rotating then these situations lead to a lift force on a particle. The lift force direction is perpendicular to the relative velocity between the phases. The effects of the added mass force occurs if one phase accelerates in relation to another phase. The accelerating phase has to overcome the inertia of the mass that lies in its path. The drag force is referred as the drag coefficient for one particle in a suspension. If the ratio between solid phase density and fluid or gas phase density is larger or equal to about 1000, the effects of the Basset and added mass force could be neglected [66]. In this study, this ratio meets with the simulated cases. For instance

the investigated case from the experiment of K.M. Luo [49], the ratio between solid phase density and gas phase density is 2183.3. Whereas the lift force really depends on the solid particle diameter. If the scale of the cell or mesh of the computed system is much larger than the solid particle diameter, usually the drag force magnitude is by far stronger than the lift force. Thus, the lift force contribution can be ignored and the coefficient of momentum exchange between phases is only contributed by the drag force. By this assumption, the forces that work on a single solid particle sphere are the gravitational force and the drag force as shown by Figure 3.1.

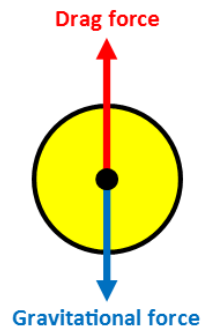


Figure 3.1: Free body diagram of forces acting on a solid particle sphere

The value of interphase momentum transfer depends on the relative velocity of the phases and the volume fraction of the solid phase. Due to its dominant and important role in the conservation equation of momentum for both phases, the appropriate model for the drag force coefficient is a must. In the literature, there are several models which could be employed to calculate the drag force coefficient and all of them are expressed as empirical equations and correlations. In this study, three models proposed by Wen and Yu, Syamlal and OBrien, and Gidaspow will be employed to calculate the drag force coefficient. The comparison of different models of the momentum exchange coefficient, β_{gm} , is shown by Figure 3.2 in which the calculation of different models based on a solid particle diameter of $520 \mu\text{m}$ and a density of 2620 kg m^{-3} , and the relative velocity between the phases is assumed to be 0.5 m s^{-1} . Figure 3.2 shows the same trend line for the three different models of momentum exchange coefficient within the solid volume fraction range of 0-0.12 (a typ-

ical range for dilute flow in a riser). By increasing the solid volume fraction, the Wen and Yu model has the lowest positive gradient of the trend line whereas Syamlal et al. model produces the highest positive gradient.

3.2.4.1 Wen and Yu model

The Wen and Yu drag model is presented below [74]:

$$\beta_{gm} = \frac{3}{4} C_D \frac{\rho_g \varepsilon_g \varepsilon_m |U_g - U_m|}{d_m} \varepsilon_g^{-2.65} \quad (3.12)$$

$$\left. \begin{array}{l} \frac{24}{Re} (1 + 0.15 Re^{0.687}) \quad \text{if } Re < 1000 \\ 0.44 \quad \text{if } Re \geq 1000 \end{array} \right\} = C_D \quad (3.13)$$

$$Re = \frac{\rho_g \varepsilon_g |U_g - U_m| d_m}{\mu_g} \quad (3.14)$$

3.2.4.2 Syamlal and O'Brien model

The Syamlal and O'Brien drag model is listed as [68]:

$$\beta_{gm} = \frac{3\rho_g \varepsilon_g \varepsilon_m}{4V_{rm}^2 d_m} (0.63 + 4.8 \sqrt{\frac{V_{rm}}{Re_m}})^2 |U_g - U_m| \quad (3.15)$$

$$V_{rm} = 0.5(A - 0.06 Re_m + \sqrt{(0.06 Re_m)^2 + 0.12 Re_m (2B - A) + A^2}) \quad (3.16)$$

$$A = \varepsilon_g^{4.14} \quad (3.17)$$

$$\left. \begin{array}{l} 0.8 \varepsilon_g^{1.28} \quad \text{if } \varepsilon_g \leq 0.85 \\ \varepsilon_g^{2.65} \quad \text{if } \varepsilon_g > 0.85 \end{array} \right\} = B \quad (3.18)$$

$$Re_m = \frac{\rho_g |U_g - U_m| d_m}{\mu_g} \quad (3.19)$$

3.2.4.3 Gidaspow model

The Gidaspow drag model is presented below [25]:

$$\left. \begin{aligned} & \frac{3}{4} C_D \frac{\rho_g \varepsilon_g \varepsilon_m |U_g - U_m|}{d_m} \varepsilon_g^{-2.65} \quad \text{if } \varepsilon_g \geq 0.80 \\ & \frac{150 \varepsilon_m (1 - \varepsilon_g) \mu_g}{\varepsilon_g d_m^2} + \frac{1.75 \rho_g \varepsilon_m |U_g - U_m|}{d_m} \quad \text{if } \varepsilon_g < 0.8 \end{aligned} \right\} = \beta_{gm} \quad (3.20)$$

$$\left. \begin{aligned} & \frac{24}{Re} (1 + 0.15 Re^{0.687}) \quad \text{if } Re < 1000 \\ & 0.44 \quad \text{if } Re \geq 1000 \end{aligned} \right\} = C_D \quad (3.21)$$

$$Re = \frac{\rho_g \varepsilon_g |U_g - U_m| d_m}{\mu_g} \quad (3.22)$$

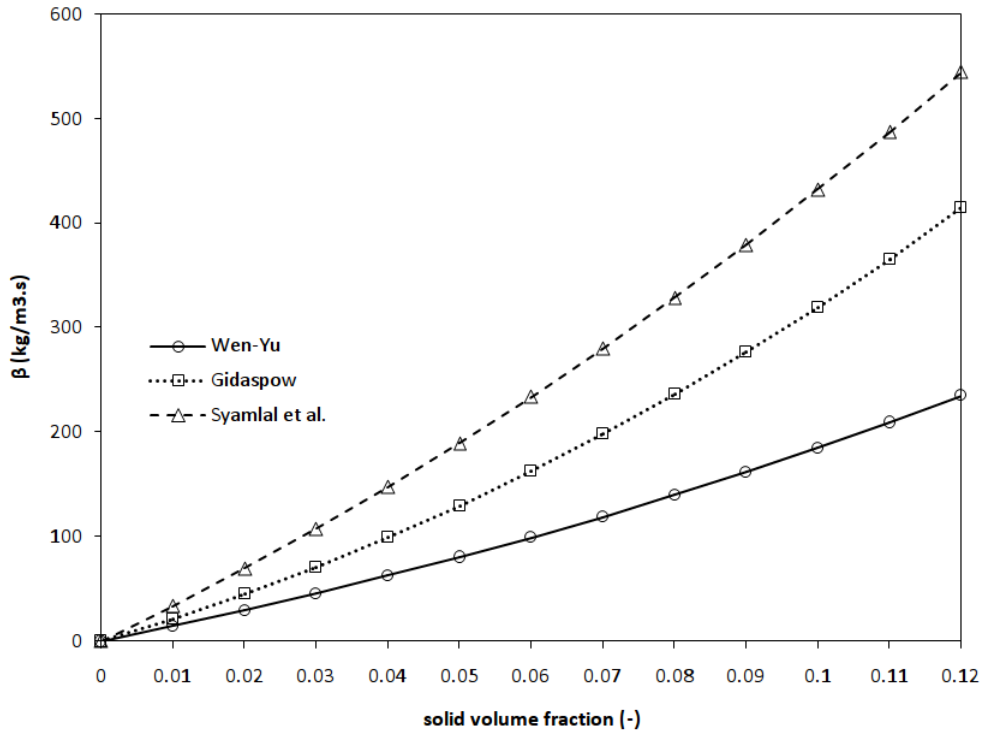


Figure 3.2: Comparison of different models of the momentum exchange coefficient

3.2.5 Kinetic Theory of Granular Flow (KTGF)

As described in the previous section, the kinetic theory of granular flow is employed to determine the parameters of solid phase flow such as solid viscosity and solid pressure. Basically, the kinetic theory of granular flow relies and follows the kinetic theory of gases by Chapman and Cowling [14]. The motion of the solid particle in the gas-solid multiphase flow could be analogous to the motion of the gas molecules. In the basics of the kinetic theory of dense gases, the gas molecules are assumed to be very small relative to the distance between molecules, having random motion and frequently collide with each other. The kinetic energy of the gas motion is measured by the gas temperature. The higher the gas temperature, the greater the gas molecules motion or the gas molecules kinetic energy. This fundamental theory of the kinetic theory of dense gases could be implemented analogously to the motion of the solid particles. In the kinetic theory of dense gases the gas temperature represents the kinetic energy of the random motion of gas molecules, whilst the kinetic theory of granular flow introduces a term called pseudo-temperature or granular temperature to represent the kinetic energy of the random solid particle motion.

When several forces (pressure force, gravity force, drag force by gas phase, other external forces) act on a solid particle assembly, the shearing motion is induced. The solid shearing motion then converts a part of its kinetic energy associated with the mean motion continuously into the solid particle fluctuating velocity. At this condition, the local instantaneous solid velocity can be decomposed into a local mean velocity and a random fluctuating velocity as shown by Equation 3.23. The granular temperature is to measure the kinetic energy of the random fluctuating velocity part of the solid phase. Sinclair and Jackson [64] reported that the solid fluctuating velocity then generates normal and tangential forces which act on the solid particles surfaces. These two forces, normal and tangential forces, fundamentally reflect the effective solid pressure and the effective solid viscosity, respectively. Consequently, the value of the solid pressure and solid viscosity will be strongly affected by the granular temperature or fluctuating velocity of the solid phase. Furthermore, the energy leading to the fluctuating velocity is dissipated by a gas-solid friction and inelastic particle collisions. All of these processes are showed by Figure 3.3 and it is clear that the value of granular temperature is a balance between the generation of the fluctuating energy due to

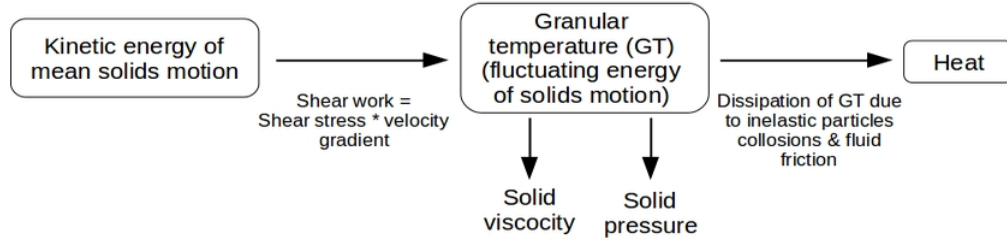


Figure 3.3: The granular temperature concept based on kinetic theory of granular flow [36]

shear work and its dissipation at any time.

As explained before, the local instantaneous solid velocity could be decomposed into a local mean velocity and a random fluctuating velocity, Equation 3.23.

$$U_m = u_m + u'_m \quad (3.23)$$

Analogous to the thermodynamic temperature for gases where the gas temperature is introduced as a measure of the gas molecular velocity fluctuations and is calculated as [25]:

$$T_g = \frac{1}{3} \frac{m_g}{k_B} \langle u'_g u'_g \rangle \quad (3.24)$$

where $\langle . \rangle$ means the local averaging, $k_B = 1.3805 \cdot 10^{-23} J/K$ is the Boltzmann constant that converts kinetic energy into temperature, then the granular temperature can be expressed as a measure of the particle velocity fluctuations and is determined as follows [25]:

$$\theta_m = \frac{1}{3} \langle u'_m u'_m \rangle \quad (3.25)$$

In addition, the kinetic energy of a gas molecule is expressed as:

$$\frac{3}{2} k_B T_g = \frac{1}{2} m_g \langle u'_g u'_g \rangle \quad (3.26)$$

As the analogy between the gas temperature and the granular temperature, the granular energy of the solid can be defined as:

$$\frac{3}{2}\theta_m = \frac{1}{2}\langle u'_m u'_m \rangle \quad (3.27)$$

Since the solid stress depends on the magnitude of these solid velocity fluctuations, a new conservation equation which represents the balance of the solid kinetic energy due to the solid fluctuating velocity should be derived. The new conservation equation supplements the continuity and momentum balance for both phases. Based on Gidaspow [25], this new conservation equation, called the granular temperature equation, is defined as below.

$$\frac{3}{2} \left[\frac{\partial}{\partial t} (\varepsilon_m \rho_m \theta_m) + \frac{\partial}{\partial x_i} (\varepsilon_m \rho_m U_{mi} \theta_m) \right] = (-P_m \delta_{ij} + \tau_{mij}) : \frac{\partial U_m}{\partial x_i} - \frac{\partial}{\partial x_i} \left(k_{th} \frac{\partial \theta_m}{\partial x_i} \right) - \gamma + \zeta \quad (3.28)$$

There are six terms in Equation 3.28. The first two terms on the left side of Equation 3.28 describe the net change of the granular energy due to its time-dependent rate of change and convective motion of the solid particles, respectively. On the right side of Equation 3.28, the first term is the production of the granular energy due to shear work, the second term is the diffusion term due to the gradient of the granular temperature, and the last two terms represent the dissipation of the granular energy due to inelastic collisions and the fluctuating energy exchange between gas and solid phases, respectively.

In order to solve the granular temperature equation, Equation 3.28, there are two methods proposed by researchers. The first method is solving the partial differential equation of the granular temperature numerically. In doing so, several constitutive equations should be defined to obtain three transport coefficients arising in Equation 3.28: diffusion coefficient, k_{th} , coefficient of granular energy dissipation, γ , and coefficient of fluctuating energy exchange, ζ . Some researchers, such as Gidaspow [25]; Hrenya and Sinclair [28], proposed different models to calculate those coefficients. The second method is using an algebraic equation of the granular temperature, proposed by Syamlal et al. [69]. The derivation of the algebraic equation of the granular temperature is based on the assumption that at a local

equilibrium, the generation or the production and the dissipation of the granular energy are the most dominant parts in the conservation of the granular energy. As the consequence of this assumption, the convective, the diffusion, and the fluctuating energy exchange terms can be neglected. Thus, the retaining terms are the generating and dissipation terms, so that Equation 3.28 is simplified as:

$$0 = (-P_m \delta_{ij} + \tau_{mij}) : \frac{\partial U_m}{\partial x_i} - \gamma \quad (3.29)$$

Using the expression derived by Lun et al. [48], the coefficient of granular energy dissipation, γ , can be determined as:

$$\gamma = \frac{12(1 - e_m^2)g_{0,m}}{d_m \sqrt{\pi}} \rho_m \varepsilon_m^2 \theta_m^{3/2} \quad (3.30)$$

Such that Equation 3.29 can be re-written as follows:

$$0 = (-P_m \delta_{ij} + \tau_{mij}) : \frac{\partial U_m}{\partial x_i} - \frac{12(1 - e_m^2)g_{0,m}}{d_m \sqrt{\pi}} \rho_m \varepsilon_m^2 \theta_m^{3/2} \quad (3.31)$$

Syamlal [67] proposed the algebraic granular temperature of Equation 3.31 as:

$$\theta_m = \left\{ \frac{-\varepsilon_m K_{1m} D_{m,ii} + \sqrt{K_{1m}^2 D_{m,ii}^2 \varepsilon_m^2 + 4\varepsilon_m K_{4m} [K_{2m} D_{m,ii}^2 + 2K_{3m} D_{m,ij} D_{m,ij}]}}{2\varepsilon_m K_{4m}} \right\}^2 \quad (3.32)$$

$$K_{1m} = 2(1 + e_m) \rho_m g_{0,m} \quad (3.33)$$

$$K_{2m} = \frac{4\rho_m d_m (1 + e_m) \varepsilon_m g_{0,m}}{3\sqrt{\pi}} - \frac{2}{3} K_{3m} \quad (3.34)$$

$$K_{3m} = \frac{\rho_m d_m}{2} \left\{ \frac{\sqrt{\pi}}{3(3 - e_m)} [0.5(3e_m + 1) + 0.4(1 + e_m)(3e_m - 1)\varepsilon_m g_{0,m}] + \frac{8\varepsilon_m g_{0,m}(1 + e_m)}{5\sqrt{\pi}} \right\} \quad (3.35)$$

$$K_{4m} = \frac{12(1 - e_m^2)\rho_m g_{0,m}}{d_m \sqrt{\pi}} \quad (3.36)$$

$$D_{m,ii} = \left[\frac{\partial U_{m,i}}{\partial x_i} \right] \quad (3.37)$$

$$D_{m,ij} = \frac{1}{2} \left[\frac{\partial U_{m,i}}{\partial x_j} + \frac{\partial U_{m,j}}{\partial x_i} \right] \quad (3.38)$$

From Equation 3.33 to Equation 3.36, there are two constants that should be determined, namely the radial distribution function, $g_{0,m}$, and the restitution coefficient, e_m . These two constants are explained in Chapter 3.2.5.3 and 3.2.5.4, respectively. Once the granular temperature is obtained by Equation 3.32, the solid viscous stress tensor and the solid pressure can be calculated due to these properties as a function of the granular temperature.

3.2.5.1 Solid Viscosity

The shear stresses which act on the solid particle is recognized as the solid viscous stress. It is contributed by the solid viscosity arising from momentum exchange of the solid particle due to its translation and collision. The solid viscosity is expressed as:

$$\mu_m = \left(\frac{2 + \alpha}{3} \right) \left[\frac{\mu_m^*}{g_{0,m} n (2 - n)} \left(1 + \frac{8}{5} n \varepsilon_m g_{0,m} \right) \left(1 + \frac{8}{5} n (3n - 2) \varepsilon_m g_{0,m} \right) + \frac{3}{5} n \mu_b \right] \quad (3.39)$$

$$\mu_m^* = \frac{\rho_m \varepsilon_m g_{0,m} \theta_m \mu}{\rho_m \varepsilon_m g_{0,m} \theta_m + \left(\frac{2\beta\mu}{\rho_m \varepsilon_m} \right)} \quad (3.40)$$

$$\mu = \frac{5}{96} \rho_m d_m \sqrt{\pi \theta_m} \quad (3.41)$$

$$n = \frac{1 + e_m}{2} \quad (3.42)$$

From Equation 3.39, the value of the solid viscosity, μ_m , depends on the solid bulk viscosity, μ_b . The solid bulk viscosity accounts for the resistance of the solid particles to compression and expansion in which its value is calculated by Equation 3.43. The radial distribution function, $g_{0,m}$, and the restitution coefficient, e_m , are introduced in Chapter 3.2.5.3 and 3.2.5.4, respectively.

$$\mu_b = \frac{256}{5\pi} \mu \varepsilon_m \varepsilon_m g_{0,m} \quad (3.43)$$

3.2.5.2 Solid Pressure

The solid pressure is the normal stress which applies on the solid particle due to particle-particle interaction and is calculated by using Equation 3.44. Chapter 3.2.5.3 will discuss how to calculate the radial distribution function, $g_{0,m}$.

$$P_m = \varepsilon_m \rho_m \theta_m (1 + 4n\varepsilon_m g_{0,m}) \quad (3.44)$$

3.2.5.3 Radial Distribution Function

Another important property for calculating the solid stress tensor is the radial distribution function. It describes the probability of collision between solid particles. When the solid volume fraction increases then the probability of solid particles collisions increases as well. It means the denser such an area the higher the probability of solid particles collisions in that area. The radial distribution function equals to zero when the solid particles do not exist. At the maximum packing limit conditions where constant contact between solid particles exists, its value tends to infinity. The value of this property allows a control parameter in keeping the solid volume fraction never reach the maximum packing limit. There are several models proposed by researchers to express the radial distribution function such as Carnahan and Starling (Equation 3.45), Lun and Savage (Equation 3.46), Ding and Gidaspow (Equation 3.47), and Syamlal et al. (Equation 3.48). The comparison of these models is shown by Figure 3.4. These four different models of radial distribution function within a typical solid volume fraction range for the dilute flow in a riser, 0-0.12, almost generate the

same value of the radial distribution function except the Ding and Gidaspow model. But within the solid volume fraction range of 0.08-0.1, all models have almost the same value. By increasing the solid volume fraction, the radial distribution function increases as well. In the current study, the model proposed by Carnahan and Starling is appointed to calculate the radial distribution function.

Carnahan and Starling model [13]:

$$g_{0,m} = \frac{(1 - 0.5\varepsilon_m)}{(1 - \varepsilon_m)^3} \quad (3.45)$$

Lun and Savage model [48]:

$$g_{0,m} = \left(1 - \frac{\varepsilon_m}{\varepsilon_m^*}\right)^{-2.5\varepsilon_m^*} \quad (3.46)$$

Ding and Gidaspow model [18]:

$$g_{0,m} = \frac{3}{5} \left[1 - \left(\frac{\varepsilon_m}{\varepsilon_m^*}\right)^{\frac{1}{3}}\right]^{-1} \quad (3.47)$$

Syamlal et al. model [69]:

$$g_{0,m} = \frac{1}{1 - \varepsilon_m} + \frac{3\varepsilon_m}{2(1 - \varepsilon_m)^2} \quad (3.48)$$

where ε_m^* is the maximum packing limit of the solid volume fraction. The method for determining the value of the maximum packing limit of the solid volume fraction is the Random close packing. It is an empirical parameter used to characterize the maximum volume fraction of solid particles obtained when they are packed randomly. When a container is randomly filled with solid particles, then the container is shaken until the solid particles do not compact any further, at this point the packing state is the Random close packing. At this state, the volume taken by number of solid particles in a given space of volume is defined as the maximum packing limit of the solid volume fraction. In general the value of the maximum packing limit of the solid volume fraction is in the range of 0.6-0.63.

3.2.5.4 Coefficient of Restitution

One of the important parameters in describing the solid particles interactions is the coefficient of restitution which describes the ratio of the kinetic energy of the solid particle after

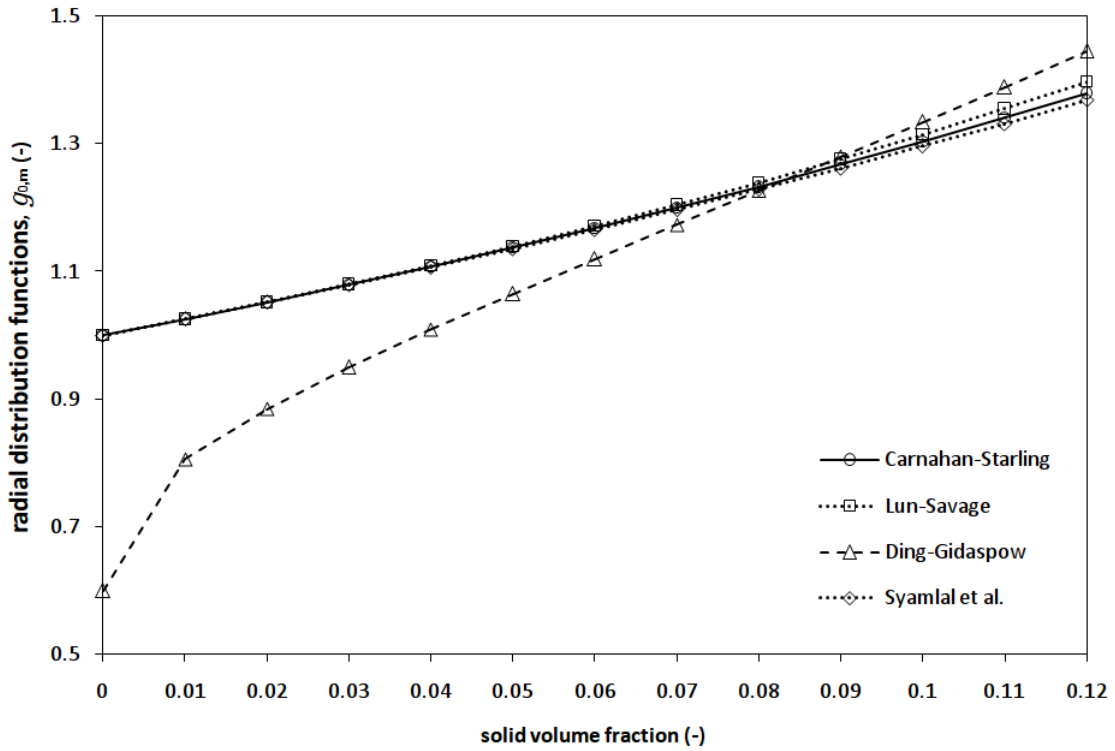


Figure 3.4: Comparison of different models of the radial distribution function

and before collision, as expressed by Equation 3.49. Once two solid particles collide, there are three possible conditions occurring after the collision. It can be that both solid particles do not move apart and coalesce. This is a perfectly inelastic collision and the kinetic energy of the collided solid particles is converted to other energy form (internal energy or heat energy of the solid particle). At this condition, the value of e_m is equal to 0. If the collided particles rebound each other with the same relative velocity when they approached, then no kinetic energy is converted or dissipated. This is a perfectly elastic collision and e_m is equal to 1. Mostly in the real application, the collision induces a dissipation of a part of the kinetic energy of the solid particles such that $0 < e_m < 1$. In the current study, the values of coefficient of restitution of 0.7 and 0.84, based on L. Cabezas-Gomez et al. [10] and Mohit P. Tandon et al. [70], are employed.

$$e_m = \frac{KE_{after}}{KE_{before}} \quad (3.49)$$

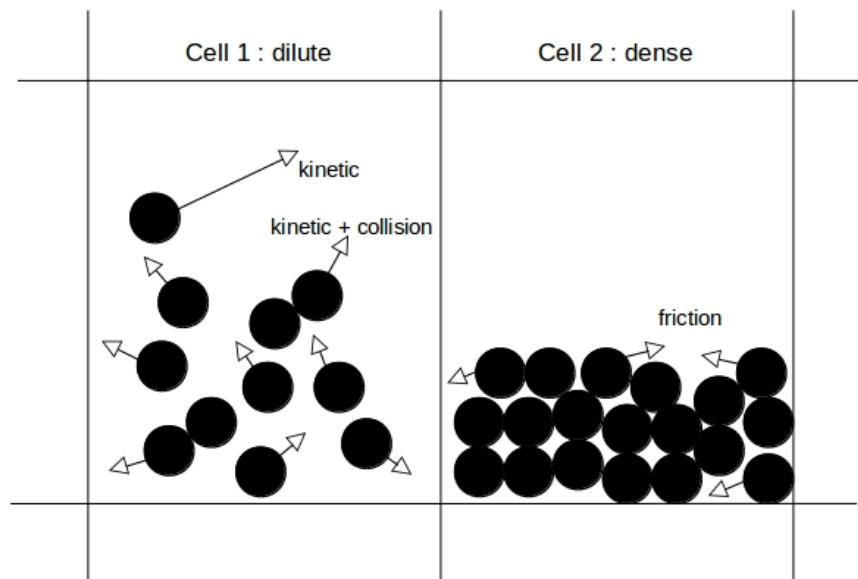


Figure 3.5: The hydrodynamics of solid particles on dilute and dense flow

3.2.6 Frictional Stress Model

In the dense flow condition, when the solid volume fraction is close to the maximum packing limit, the friction of the solid phase dominates its hydrodynamics behaviour, instead of the kinetic/translation and collision of individual particles as presented by Figure 3.5. In this situation, called as a critical condition, the interaction time between solid particles is much longer than at dilute flow such that the generating of solid stress is mostly contributed by frictions between solid phases. At the critical condition, the kinetic theory of the granular flow is not applicable to express the hydrodynamics behaviour of the solid phase. Therefore, a model has to be introduced to describe the behaviour of the solid phase in corresponding to solid pressure (normal stress) and solid viscosity (shear stress). There are some models proposed to calculate frictional solid pressure, P_f , and frictional solid viscosity, μ_f . In this study, the model proposed by Schaeffer [60] is appointed to determine these properties at critical condition, where the solid volume fraction exceeds the maximum packing limit of the solid volume fraction.

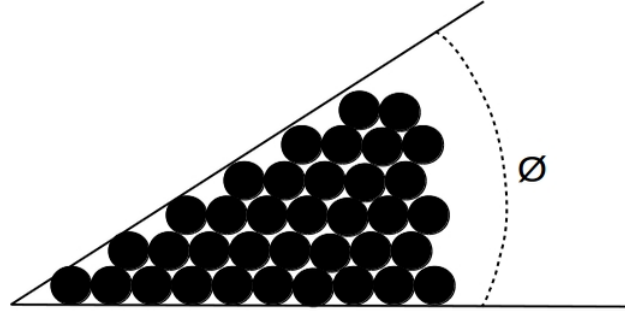


Figure 3.6: Internal friction angle

$$\left. \begin{array}{l} 10^{25}(\varepsilon_m^* - \varepsilon_g)^{10} \quad \text{if } \varepsilon_g < \varepsilon_m^* \\ 0 \quad \text{if } \varepsilon_g \geq \varepsilon_m^* \end{array} \right\} = P_f \quad (3.50)$$

$$\left. \begin{array}{l} \min\left(\frac{P_f \sin \phi}{\sqrt{4I_{2D}}}, 100\right) \quad \text{if } \varepsilon_g < \varepsilon_m^* \\ 0 \quad \text{if } \varepsilon_g \geq \varepsilon_m^* \end{array} \right\} = \mu_f \quad (3.51)$$

$$I_{2D} = \frac{1}{6}[(D_{m,11} - D_{m,22})^2 + (D_{m,22} - D_{m,33})^2 + (D_{m,33} - D_{m,11})^2] + D_{m,12}^2 + D_{m,23}^2 + D_{m,31}^2 \quad (3.52)$$

where $D_{m,ii}$ and $D_{m,ij}$ are calculated using Equation 3.37 and 3.38 ($i, j = 1, 2, 3$), ε_m^* is the maximum packing limit of the solid volume fraction, ϕ is the internal friction angle, and I_{2D} is the second invariant of the deviatoric stress tensor. The internal friction angle is a parameter used to describe the stability of a sloped surface of solid particles. It is the steepest slope angle of a solid particle pile relative to the horizontal surface that can be maintained without sliding, as shown by Figure 3.6. Finally in the dense flow condition, the total solid pressure and the total solid viscosity are calculated as :

$$P_{m,total} = P_m + P_f \quad (3.53)$$

$$\mu_{m,total} = \mu_m + \mu_f \quad (3.54)$$

where μ_m and P_m are calculated by equation 3.39 and equation 3.44, respectively.

3.2.6.1 $k-\epsilon$ Turbulence Model for the Gas Phase

In this study, for the turbulent simulation, the gas phase turbulence is modelled by using the standard $k - \epsilon$ turbulence model [40]. In turbulent flow, the total gas phase viscosity can be expressed as:

$$\mu_g = \mu_{g,l} + \mu_{g,tr} \quad (3.55)$$

where $\mu_{g,l}$ is the laminar gas viscosity which is a constant of $1.82 \times 10^{-5} \text{ kg m}^{-1} \text{ s}^{-1}$ in the current study and $\mu_{g,tr}$ is the turbulent gas viscosity which is determined by the standard $k - \epsilon$ turbulence model as follows:

$$\mu_{g,tr} = \rho_g C_\mu \frac{k^2}{\epsilon} \quad (3.56)$$

From Equation 3.56, the turbulence kinetic energy, k , the rate of turbulence energy dissipation, ϵ , and a constant of C_μ should be determined. The turbulence kinetic energy, k , and the rate of turbulence energy dissipation, ϵ , are obtained from the transport equations of 3.57 and 3.58, respectively. These transport equations are proposed by Launder and Spalding [40] and modified for the gas phase turbulence model in gas-solid flow as shown by Equation 3.57 and 3.58 [7]. The modification of the standard $k - \epsilon$ turbulence model for the gas phase turbulence model in gas-solid flow is carried out by introducing the gas volume

fraction, ε_g , into the k - and ϵ - equation.

$$\underbrace{\frac{\partial}{\partial t}(\varepsilon_g \rho_g k)}_{\text{rate of change of } k} + \underbrace{\frac{\partial}{\partial x_i}(\varepsilon_g \rho_g k U_{g,i})}_{\text{convective of } k} = \underbrace{\frac{\partial}{\partial x_j} \left[\varepsilon_g \left(\mu_g + \frac{\mu_{g,tr}}{\sigma_k} \right) \frac{\partial k}{\partial x_j} \right]}_{\text{diffusive of } k} + \underbrace{G_k}_{\text{production of } k} - \underbrace{\varepsilon_g \rho_g \epsilon}_{\text{dissipation of } k} \quad (3.57)$$

$$\underbrace{\frac{\partial}{\partial t}(\varepsilon_g \rho_g \epsilon)}_{\text{rate of change of } \epsilon} + \underbrace{\frac{\partial}{\partial x_i}(\varepsilon_g \rho_g \epsilon U_{g,i})}_{\text{convective of } \epsilon} = \underbrace{\frac{\partial}{\partial x_j} \left[\varepsilon_g \left(\mu_g + \frac{\mu_{g,tr}}{\sigma_\epsilon} \right) \frac{\partial \epsilon}{\partial x_j} \right]}_{\text{diffusive of } \epsilon} + \underbrace{\varepsilon_g C_{1\epsilon} \frac{\epsilon}{k} G_k}_{\text{production of } \epsilon} - \underbrace{\varepsilon_g C_{2\epsilon} \rho_g \frac{\epsilon^2}{k}}_{\text{dissipation of } \epsilon} \quad (3.58)$$

where G_k is the turbulent kinetic energy production due to the mean velocity gradients and is calculated by Equation 3.59, $C_{1\epsilon}$, $C_{2\epsilon}$, C_μ , are constants in which their values are listed in Table 3.1 as well as the value of the turbulent Prandtl numbers for k and ϵ , σ_k and σ_ϵ , respectively.

$$G_k = \mu_{g,tr} \left[\frac{1}{2} \left(\frac{\partial U_i}{\partial x_j} + \frac{\partial U_j}{\partial x_i} \right)^2 - \frac{2}{3} \left(\frac{\partial U_k}{\partial x_k} \right)^2 \right] \quad (3.59)$$

Table 3.1: Model constants for $k - \epsilon$ turbulence model [40]

$C_{1\epsilon}$	$C_{2\epsilon}$	C_μ	σ_k	σ_ϵ
1.44	1.92	0.09	1.0	1.3

3.3 The 3D CFD-code AIOLOS

AIOLOS is a CFD software which has been developed by IFK, Stuttgart University, Germany. AIOLOS is a CFD software dedicated for simulating pulverized coal combustion and solid fuel gasification from small-scale to full-scale industrial furnaces or boilers. It has a broad range of capability in calculating physical and chemical processes. The AIOLOS code consists of several packages which are able to solve hydrodynamics, chemical reactions or combustion, heat and mass transfer, and radiation problems. Nevertheless, the original AIOLOS package has not been able to simulate fluidized beds combustion process such as

BFB or CFB boilers yet. Beholding the important role of CFD in developing high-efficiency fluidized beds combustion, it is a challenging idea and task to develop the code for simulating fluidized beds combustion reactors like BFB and CFB boilers.

The Finite Volume Method (FVM) is the basis of the numerical method utilized by the software and the Fortran language is used for building the software. It is applicable for different coordinates system, either cartesian, cylindrical, or body fitted coordinates. The Semi-Implicit Method for Pressure-Linked Equations (SIMPLE) algorithm is employed to solve velocity-pressure coupling on Navier-Stokes equations. To prevent decoupling of velocity and pressure on the non-staggered grid, Date interpolation [16] is assigned to do so. The central difference scheme is used to calculate the convective fluxes. Moreover, the code is also capable to carry out parallel and vector computing as well as the domain decomposition approach. Utilizing this capability, the code is able to handle a large-scale domain discretization with up to million of computational cells such as full-scale industrial power-plant boiler. Further explanations about the code can be found elsewhere [21, 42].

In order to enhance the AIOLOS capability for solving multiphase flow problems, the current research develops AIOLOS for simulating gas-solid two phase flows in a riser by implementing the Eulerian-Eulerian approach or Two-Fluid Method (TFM). The developed AIOLOS is then tested to predict the hydrodynamics behaviour of gas-solid flow in a 3D cylindrical riser at transient condition. Afterwards, in order to validate the accuracy of the developed code, the time-averaged simulation results are compared to the empirical results which are achieved by experiments of another researcher. The current developed code is the first ever of AIOLOS development that dealing with gas-solid two phase flow. Thus, this code has some limitations which should be improved in the future such as uniform solid particle diameter assumption, applicable for riser flow with maximum solid fraction about 0.1 and turbulent regime. In general, the main differences calculation task or procedure between the existing AIOLOS code and the developed AIOLOS code (current study) is presented by Figure 3.7.

Existing AIOLOS	Modified AIOLOS (current work)
Steady state simulation	Transient simulation
Define gas properties	Define gas properties
	Calculate physical properties of solid: Granular temperature Solid viscosity Solid pressure Gas-Solid momentum exchange coeff.
Solve momentum equation of gas	Solve momentum equation of gas
	Solve momentum equation of solid
SIMPLE for gas	SIMPLE for gas
	Calculate solid pressure gradient
	Solve solid fraction equation
	Calculate gas fraction
Calculate convective part of gas	Calculate convective part of gas
	Calculate convective part of solid
Saving final result of calculation	Saving final result of calculation
	Saving intermediate result of calculation

Figure 3.7: The differences of calculation between the existing and the developed AIOLOS

4 Numerical Simulation Procedure

This chapter will explain the details of the numerical procedure which is implemented into the developed CFD code. It consists of the solution algorithm and the numerical scheme which are employed to solve and simulate gas-solid two phase flow. Furthermore, the developed code is employed to simulate two cases, namely the gas-solid flow in a cylindrical riser based on the experiments of K.M. Luo which were reported in his doctoral thesis [49] and its simulation by L. Cabezas-Gomez et al. [10] and the gas-solid flow in a rectangular riser based on the experiments of J. Zhou et al. [81] and its simulation by Tingwen Li et al. [47]. The comparisons of the current results with the previous works are made using radial profiles of the axial velocity of gas and solid phases and of the solid volume fraction.

4.1 Solution Algorithm

The solution algorithm is adopted from Syamlal et al. [69] with some modifications. The computational steps during a time step calculation are given below. Figure 4.1 shows the calculation flowchart used in the solution algorithm. In the current simulation, the convergence criteria are the minimum residual of $1.0e-04$ and the number of iterations of 10 for each time step. In Step 4 of the solution algorithm, the correction of the solid velocity is carried out by using a correlation that is adopted from Multiphase Flow with Interphase eXchanges (MFIx) CFD software [50]. This method is explained briefly in Chapter 4.2.

The solution algorithm :

1. Start time step
2. Calculate physical properties and exchange coefficients for gas and solid phase.

3. Solve momentum equations for both phases corresponding to the x, y, z directions.
4. Calculate gas pressure by using SIMPLE method:
 - a. Calculate gas pressure correction.
 - b. Update gas pressure.
 - c. Correct gas velocity.
5. Calculate solid pressure gradient with respect to solid volume fraction.
6. Solve solid volume fraction correction equation:
 - a. Calculate solid volume fraction correction.
 - b. Update solid volume fraction.
 - c. Calculate solid velocity correction and update the solid velocity.
7. Calculate gas volume fraction
8. Calculate convective part for both phases
9. Check the convergence: if the convergence criterion is satisfied then go to the next time step (Step 1), otherwise continue the iteration (back to Step 2).

4.2 Numerical Scheme

The governing equations described in Chapter 3 have a similar structure which can be expressed in a general form of transport equations for an arbitrary variable α :

$$\frac{\partial}{\partial t} (\alpha\rho) + \frac{\partial}{\partial x_i} (\alpha\rho U_i) = \frac{\partial}{\partial x_i} \left(\Gamma \frac{\partial \alpha}{\partial x_i} \right) + S_\alpha \quad (4.1)$$

where Γ is the coefficient of diffusion. Equation 4.1 has four terms namely transient and convective terms in the left hand side and diffusion and source terms in the right hand side. Due to the nature of gas-solid multi phase flow as highly fluctuating over the time, all of these terms will be considered during simulation.

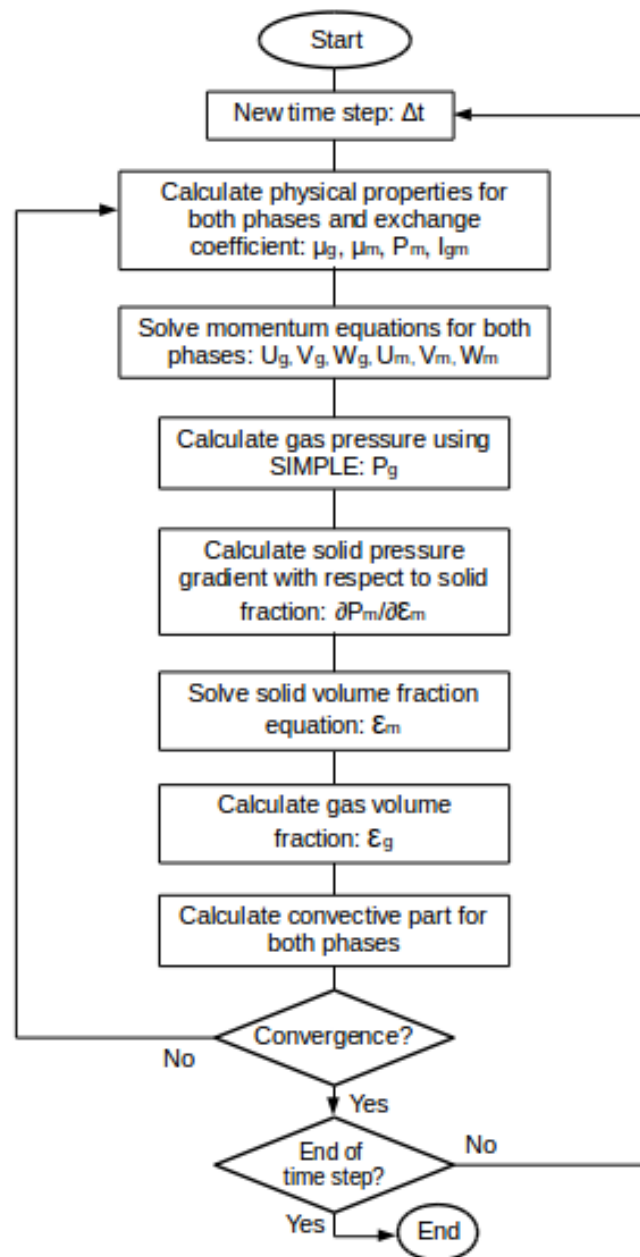


Figure 4.1: The solution algorithm

The general transport equation 4.1 will pretend in the computed domain. In order to solve the equation numerically, the Finite Volume Method is applied to discretise it over the domain. The discretisation produces a system of coupled linear equations as:

$$A_P \cdot \alpha_P = \sum_{nb} (A_{nb} \cdot \alpha_{nb}) + S_\alpha \cdot V \quad (4.2)$$

where:

$$A_P = \sum_{nb} A_{nb} \quad (4.3)$$

In the present work, the Cartesian coordinate system with non-staggered structured grid is used and shown by Figure 4.2. The capital letter of P represents the center of the calculated cell while E, W, N, S show the center of its neighbouring cells, namely East, West, North, and South, respectively. The non-capital letters, e, w, n, s , describe the face of the neighbouring cells which are adjacent with the calculated cell P . A collocated grid arrangement which means all properties either scalar or vector are stored in the cell-center is utilized in the CFD code. Considering Equation 4.2 and Figure 4.2, in 2D-coordinate system, cell P has four neighbouring cells ($nb = e, w, t, b$) and coefficient A_{nb} is contributed by diffusive and convective parts of Equation 4.1. Whilst the source term $S_\alpha \cdot V$ is contributed by forces such as pressure and gravitational forces.

Since all properties are stored in the cell-center, an interpolation scheme should be employed to calculate the properties at the cell-face. Some interpolation schemes are available, namely First order upwind, Central difference, Power law, Second-order upwind, Hybrid, and Quadratic upwind interpolation for convective kinematics (QUICK). In the current study, in order to calculate the diffusive and convective part at the cell-face, the Central difference scheme is appointed to be implemented into the CFD code. It is easy but quite accurate and it needs less computing demand. The interpolation calculation of the Central difference scheme is shown by Figure 4.3.

For dealing with the pressure-velocity coupling problem, the extension of the Semi-Implicit Method for Pressure Linked Equations (SIMPLE) is used [55]. The method was developed by Brian Spalding and Suhas Patankar in the early 1970s. The Date interpolation scheme is utilised to prevent decoupling of velocities and pressure on the non-staggered grid system

[16]. The iterative solution of Equation 4.2 needs a stability such that under-relaxation has to be introduced. Mostly the source term in Equation 4.2 is a function of the dependent variable α itself. Since the discretisation equation produces a coupled linear equation system and it will be solved by a technique for linear algebra, considering a linear dependence of the source term over the variable α is acceptable. Thus, the linearisation of the source term in Equation 4.2 could be expressed as:

$$S_{\alpha} = S_{\alpha,C} + S_{\alpha,P} \cdot \alpha_P \quad (4.4)$$

where $S_{\alpha,C}$ stands for the constant part of S_{α} and $S_{\alpha,P}$ is the coefficient of α_P . The important rule of this linearization is that the coefficient $S_{\alpha,P}$ must always be less than or equal to zero [55].

An iterative solver is utilized to solve a coupled linear equation system produced by this discretisation procedure. There are some available iterative solvers, namely Successive Over-Relaxation (SOR), SOR Red Black, Strongly Implicit Procedure (SIP), Bi-Conjugate Gradient Stabilized (BiCGSTAB), Conjugate Gradient Squared with ILU-Factorization (ILU CGS), Bi-Conjugate Gradient Stabilized with Incomplete LU-Factorization (ILU BiCGSTAB), and Generalized Minimal Residual (GMRES). In this study, the Successive Over-Relaxation (SOR) Red Black iterative solver is employed to solve the linear equation system. In the developed CFD code, the segregated solution procedure is selected to be implemented. The segregated method solves an equation for a certain variable for all cells and then the equation for the next variable is solved for all cells.

In step 6 of the solution algorithm, the correction of the solid velocity is carried out by using a correlation that is adopted from Multiphase Flow with Interphase eXchanges (MFIx) CFD software [50]. This correlation calculates the coefficient of the solid velocity correction as follows:

$$U_{m,corr} = U_{acorr} U_{bcorr} \quad (4.5)$$

where:

$$U_{acorr} = \frac{A}{A_{P,m}} \quad (4.6)$$

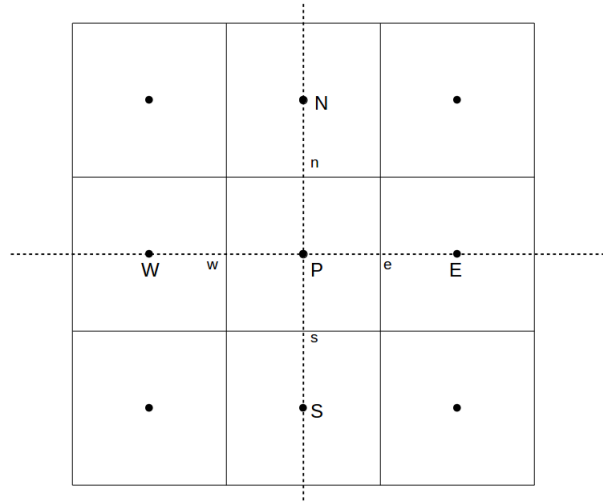


Figure 4.2: Non-staggered grid

$$U_{bcorr} = 10^{25} \{ \max [0.0, (0.4 - \varepsilon_g)] \}^9 \varepsilon_m \quad (4.7)$$

in which A is the cross-section area of the computed cell, $A_{P,m}$ is Equation 4.3 for solid phase.

4.3 Solving Solid Phase Continuity Equation

As mentioned in Chapter 3.1, one of the governing equations of the Two-Fluid Model is the mass conservation of the solid phase as follows:

$$\frac{\partial}{\partial t} (\varepsilon_m \rho_m) + \frac{\partial}{\partial x_i} (\varepsilon_m \rho_m U_{mi}) = 0 \quad (4.8)$$

In order to obtain the solid volume fraction, Equation 4.8 should be discretized and solved. This task is carried out by step 6 in the solution algorithm (Chapter 4.1). In this study, for handling this task the technique implemented by Syamlal et al. called The Solid Volume Fraction Correction Equation is adopted [69]. The technique is mainly based on the idea to incorporate the effect of solid pressure in calculating the solid volume fraction due to the strong correlation between these two properties. In doing so, a equation of state that

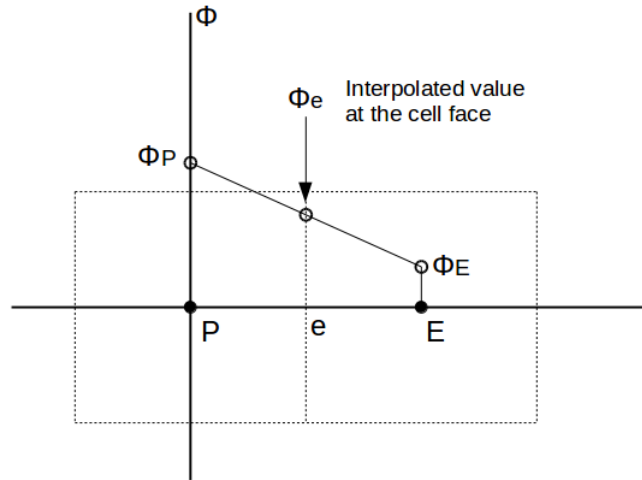


Figure 4.3: The central difference scheme

correlates solid pressure to solid volume fraction is introduced as:

$$P_m = P_m(\varepsilon_m) \quad (4.9)$$

Such a coefficient which expresses the change of solid pressure due to the change of solid volume fraction is defined as:

$$K_m = \frac{\partial P_m}{\partial \varepsilon_m} \quad (4.10)$$

Thus, any small change in solid pressure could be calculated from a change in solid volume fraction as expressed by Equation 4.11.

$$P'_m = K_m \varepsilon'_m \quad (4.11)$$

If the convective term of Equation 4.8 is discretized on a grid as shown by Figure 4.2, then it leads to Equation 4.12.

$$\int \frac{d}{dx} (\varepsilon_m \rho_m U_m) dV = (\varepsilon_m \rho_m U_m)_e A_e - (\varepsilon_m \rho_m U_m)_w A_w \quad (4.12)$$

For calculating the fluxes on faces $(\varepsilon_m \rho_m U_m)_e$ and $(\varepsilon_m \rho_m U_m)_w$, such a formulation should be defined. Denoting the actual solid velocity on the east face of the control volume as:

$$(U_m)_e = (U_m^*)_e + (U'_m)_e \quad (4.13)$$

where $(U_m^*)_e$ is the solid velocity obtained from step 3 of the solution algorithm in Chapter 4.1 and $(U'_m)_e$ is the solid velocity correction that is related to the correction in the solid pressure field and expressed by Equation 4.14. In Equation 4.14, the coefficient of the solid volume fraction correction, e_e , is calculated by Equation 4.15 [50].

$$(U'_m)_e = e_e \left((P'_m)_P - (P'_m)_E \right) \quad (4.14)$$

$$e_e = \frac{A_e}{A_{P,m}} \quad (4.15)$$

Substituting Equation 4.11 to Equation 4.14 such that:

$$(U'_m)_e = e_e \left((K_m)_P (\varepsilon'_m)_P - (K_m)_E (\varepsilon'_m)_E \right) \quad (4.16)$$

As well as the solid velocity, the solid volume fraction can be described as a sum of the current value and a correction:

$$(\varepsilon_m)_e = (\varepsilon_m^*)_e + (\varepsilon'_m)_e \quad (4.17)$$

Combining Equation 4.16 and Equation 4.17, the fluxes on face e can be expressed as:

$$\begin{aligned} (\varepsilon_m \rho_m U_m)_e &\approx \rho_m [(\varepsilon_m)_e (U_m)_e] \\ &\approx \rho_m \left[(\varepsilon_m^*)_e (U_m^*)_e + (\varepsilon'_m)_e (U_m^*)_e + (\varepsilon_m^*)_e (U'_m)_e + (\varepsilon'_m)_e (U'_m)_e \right] \end{aligned} \quad (4.18)$$

By neglecting the correction product $(\varepsilon'_m)_e (U'_m)_e$, Equation 4.18 can be expressed as:

$$\begin{aligned}
 (\varepsilon_m \rho_m U_m)_e &\approx \rho_m \left[(\varepsilon_m^*)_e (U_m^*)_e + (\varepsilon'_m)_e (U_m^*)_e + (\varepsilon_m^*)_e (U'_m)_e \right] \\
 &\approx \rho_m \left[(\varepsilon_m^*)_e (U_m^*)_e + (\varepsilon'_m)_e (U_m^*)_e \right] \\
 &\quad + \rho_m \left[(\varepsilon_m^*)_e e_e \left((K_m)_P (\varepsilon'_m)_P - (K_m)_E (\varepsilon'_m)_E \right) \right]
 \end{aligned} \tag{4.19}$$

The discretisation of the transient part of the mass conservation of solid phase, Equation 4.8, is expressed by Equation 4.20 as below. The superscript notation of zero, 0, in Equation 4.20 represents the related properties from the previous time step iteration.

$$\begin{aligned}
 \int \frac{d}{dt} (\varepsilon_m \rho_m) dV &= \left[(\varepsilon_m)_P (\rho_m)_P - (\varepsilon_m)_P^0 (\rho_m)_P^0 \right] \Delta V \Delta t^{-1} \\
 &= \left[\left((\varepsilon_m^*)_P + (\varepsilon'_m)_P \right) (\rho_m)_P - (\varepsilon_m)_P^0 (\rho_m)_P^0 \right] \Delta V \Delta t^{-1} \\
 &= (\varepsilon'_m)_P (\rho_m)_P \Delta V \Delta t^{-1} \\
 &\quad + \left[(\varepsilon_m^*)_P (\rho_m)_P - (\varepsilon_m)_P^0 (\rho_m)_P^0 \right] \Delta V \Delta t^{-1}
 \end{aligned} \tag{4.20}$$

5 Numerical Simulation of 3D Gas-Solid Flow in Cylindrical Riser

5.1 Simulation Parameters

The test case for gas-solid multiphase flow simulation in this study is based on the experiments of K.M. Luo which were reported in his doctoral thesis [49] and its simulation by L. Cabezas-Gomez et al. [10]. The case is a 3D-cylindrical riser with height of 5.5 m and diameter of 0.076 m in which solid particles with average diameter of 520 μm and density of 2620 kg m^{-3} flow into it. The detailed parameters used in this study are listed in Table 5.1. The geometry of the simulation test case is shown by Figure 6.1, while Figure 5.2 shows two different rectangular meshing of the computation domain. The detail of boundary conditions (BC) of the simulation, namely inlet BC, outlet BC, wall BC, for gas and solid phases are explained below.

- a The inlet boundary conditions for gas and solid phases and its properties are listed below:

Gas phase

$$\mu_g : 1.82 \times 10^{-5} \text{ kg m}^{-1} \text{ s}^{-1}$$

$$\rho_g : 1.225 \text{ kg m}^{-3}$$

$$\varepsilon_g : 0.9754$$

$$U_{g,x} : 4.979 \text{ m s}^{-1}$$

Solid phase

$$d_m : 520 \mu\text{m}$$

$$\rho_m : 2620 \text{ kg m}^{-3}$$

$$\varepsilon_m : 0.0246$$

$$U_{m,x} : 0.386 \text{ m s}^{-1}$$

Concerning the riser dimension and the uniform inlet gas velocity entering the riser, it represents that the gas flow inside the riser is turbulent due to its Reynolds number is 2.55×10^4 . This bed riser is then identified as the turbulent bed regime. Regarding the properties of the solid phase, it can be concluded that the used solid particle is classified as Geldart particle Group B.

b Outlet boundary condition:

The zero gradient at outlet for any property is set up as the outlet boundary condition as expressed by Equation 6.1

$$\left(\frac{\partial \alpha}{\partial x_i} \right)_{outlet} = 0 \quad (5.1)$$

where α is the respective property or variable.

c Wall boundary condition:

For both phases, gas and solid phase, a no slip boundary condition is utilized.

5.2 Simulation Results and Discussion

Firstly the simulations are carried out for the laminar condition. The simulations are carried out from 0 s to 40 s with several variations of the simulation parameters in which each simulation variant is computed on a single computer. The simulation results from 30-40 s are then averaged in order to be compared with the experiment by K.M Luo [49] and its simulation by L. Cabezas-Gomez et al. [10]. The time-averaged results are obtained from the highlighted position in the riser as shown by Figure 5.3. In the current study, four parameters are examined during the simulations in order to analyse the effects on the hydrodynamics of the gas-solid flow in the riser. These parameters are the drag model, radial distribution function, coefficient of restitution, and time step. In the next sub-chapters,

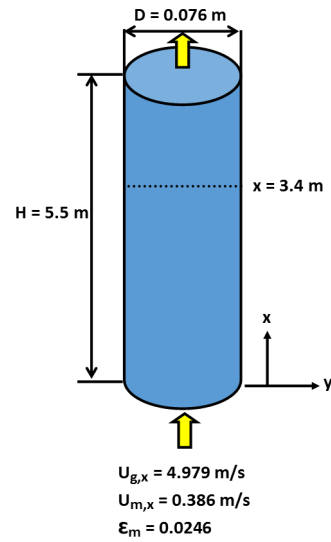


Figure 5.1: Geometry and boundary conditions used in simulations (presented in 2D-plane)

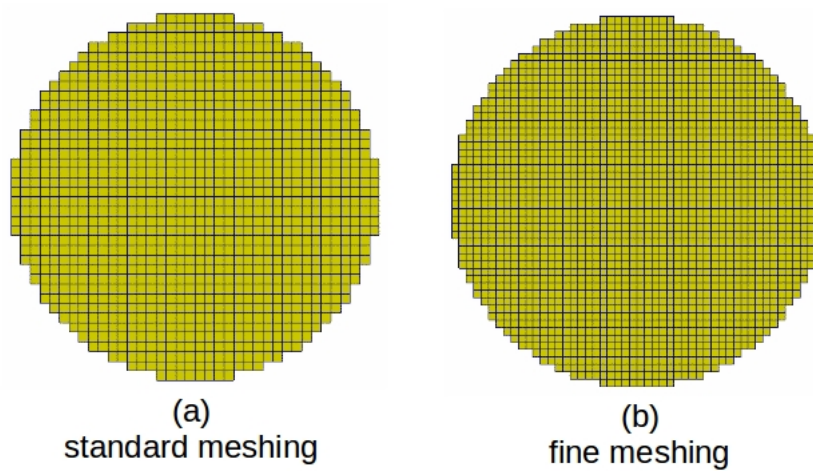


Figure 5.2: Two different meshings

Table 5.1: Simulation parameters of 3D gas-solid flow in cylindrical riser

Parameter	
Riser geometry	height of 5.5 m, diameter of 0.076 m
Meshing (cells)	standard: 168600, fine: 948480
Flow condition	transient (unsteady)
Time step (s)	0.0001, 0.00015
Time interval of simulation (s)	0-40
Range of time-averaged results (s)	30-40
Drag model (cf. Chapter 5.2.4)	Wen-Yu, Syamlal et al., Gidaspow
Radial distribution model (cf. Chapter 5.2.5)	Carnahan-Starling, Syamlal et al.
Restitution coefficient (cf. Chapter 5.2.6)	0.7, 0.84
Gas phase viscous	laminar, turbulent

the influence of these parameters will be discussed. The comparisons of numerical results with experimental data are made using radial profiles of the axial velocity of gas and solid phases and of the solid volume fraction. An important notation for the experimental data by K.M Luo [49] should be considered. They were measured from one side of the riser to its center only. Therefore, it is not certain that the experimental data were symmetric. After examining the simulation results of the laminar condition, the turbulent condition are then simulated and examined as described in sub-chapter 5.2.9.

5.2.1 The Influence of Meshing

Determining a proper mesh for the computation is really important. The trade-off between meshing scheme which closely represents the actual condition of the computation domain and the required computing resource is always arising in any simulation. In this study, us-

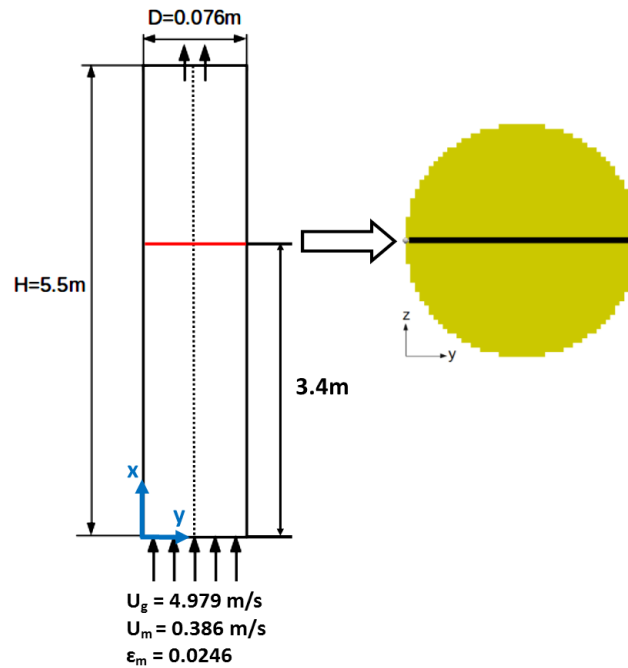


Figure 5.3: The highlighted position for capturing the simulation results

ing Gidaspow drag model, Carnahan-Starling radial distribution function model, restitution coefficient of 0.7, time step of 0.0001 s, two different meshes are examined in order to find an optimum point. These two meshes are shown by Figure 5.2 that represent a standard and a fine meshing, respectively. The standard meshing, Figure 5.2(a), consists of 168600 cells while the fine meshing, Figure 5.2(b), is composed by 948480 cells. In order to compare the effect of different meshes, a simulation up to 10 s is carried out on a single computer and its results are then compared in respect to solid velocity and solid volume fraction properties. The comparison of the solid velocity profile is shown by Figure 5.4, while Figure 5.5 represents the solid volume fraction profile. After simulation of 10 s, either solid velocity profile or solid volume fraction profile for both meshes shows a qualitatively good agreement. In Figure 5.4, the deviation of solid velocity between the two meshes is significant enough in the riser center but in the area close to the riser wall, the deviation can be ignored. Whereas the deviation of the solid volume fraction as shown by Figure 5.5 is somewhat large in the area close to the riser wall. But from 5 s to 10 s this value is significantly decreasing. The asymmetrical solid volume fraction profiles may be due to the flow condition inside the riser which is not yet steady. Furthermore, the comparison of computation resource in terms of

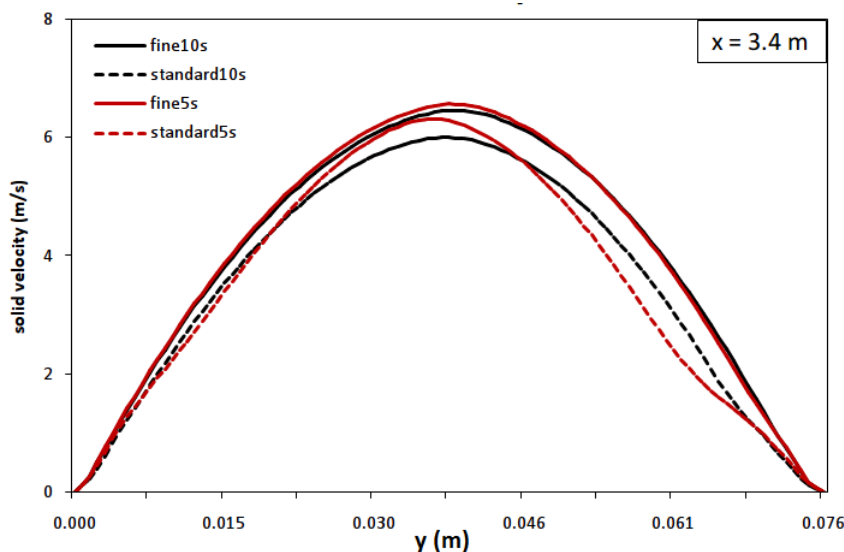


Figure 5.4: Solid velocity profile obtained by two different meshes: standard and fine

calculation time, the fine meshing is much more time demanding than the standard meshing. While the difference of cell numbers is about 779880 cells between the two different meshes, the fine meshing needs 38 days of computation time whilst the standard meshing only demands 10 days for the simulation up to 10 s. Taking into consideration the simulation results and the computation time, the standard meshing looks more appropriate than the fine meshing for discretization of the simulation domain. Thus, the standard meshing is employed for a full 40 s simulation.

5.2.2 The Influence of Initial Condition

In this section, different initial conditions are examined in order to understand their effect on the simulation of the hydrodynamics behaviour of the gas-solid flow in the riser. Three different initial conditions are employed to simulate the gas-solid flow in the riser up to 6 s using Syamlal et al. drag model, Syamlal et al. radial distribution function model, restitution coefficient of 0.84, and time step of 0.0001 s. The first is "high" initial value which means the axial gas velocity, the axial solid velocity, and the solid volume fraction are determined as 3 m/s, 2.5 m/s, and 0.0002 respectively. The second initial condition is "low" which means the axial gas velocity, the axial solid velocity, and the solid volume fraction are fixed as 0.002 m/s, 0.001 m/s, and 0.0002 respectively. The "standard" initial condition assigns the axial

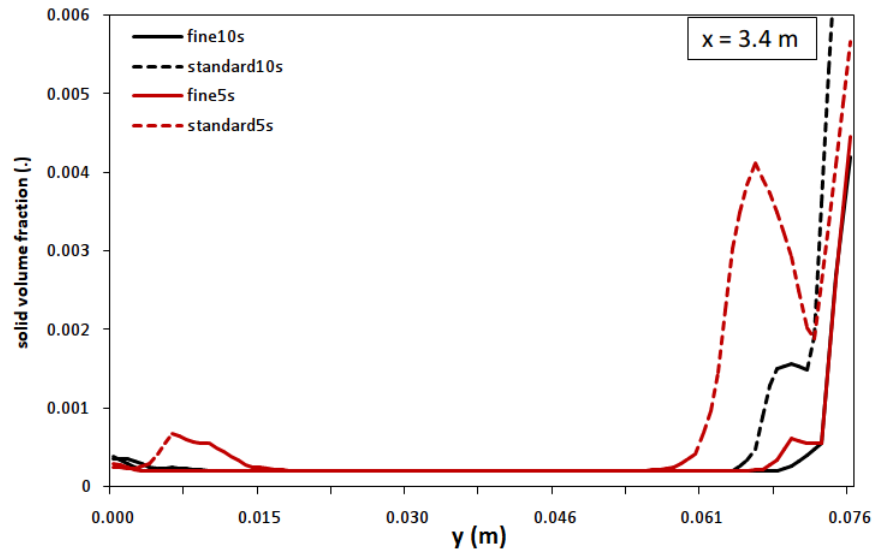


Figure 5.5: Solid volume fraction profile obtained by two different meshes: standard and fine

gas velocity, the axial solid velocity, and the solid volume fraction as 3 m/s, 0.001 m/s, and 0.0002, respectively. After 6 s of calculation, it can be concluded that the initial conditions have no significant effect on the hydrodynamics of the gas-solid flow in the riser. Figure 5.6 and Figure 5.7 show quantitatively good agreement of solid velocity and solid volume fraction for three different initial conditions. Therefore, it could be deduced that the effect of the initial condition used in the current simulations tends to disappear after a certain calculation time. This conclusion shows a consistency with the result reported by Benyania et al. [6]. For a full 40 s simulation, the "standard" initial condition is employed to simulate the gas-solid flow in the riser.

5.2.3 The Variation of Simulation Parameters

The simulation parameters which are examined in this study are 3 different drag models, 2 different radial distribution function models, and 2 different coefficient of restitution values. The combination of these 3 parameters yields 12 variations of the simulation parameters as listed in Figure 5.8. In order to understand the effects of these parameters on the hydrodynamics of gas-solid flow, these 12 variations are simulated with different time steps, 0.0001 s and 0.00015 s, thus in total there are 24 variations of the simulations. Due to the limitation

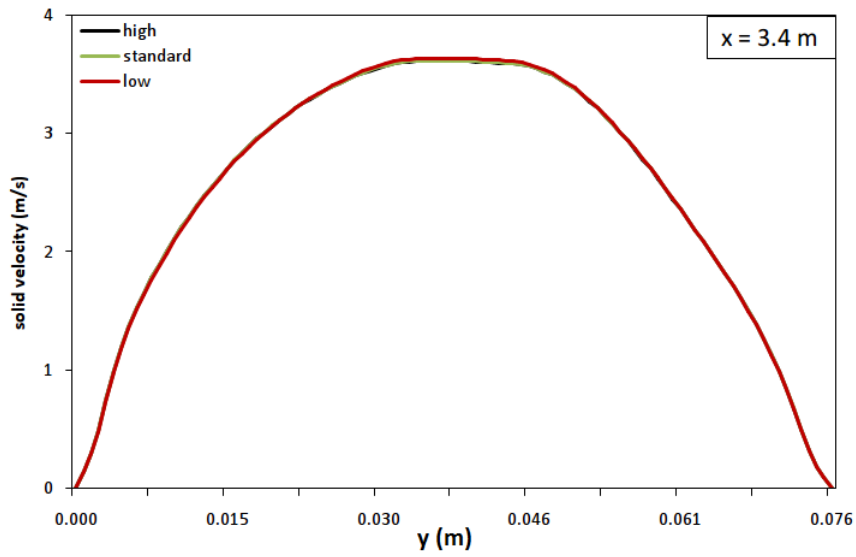


Figure 5.6: Solid velocity profile obtained by different initial conditions

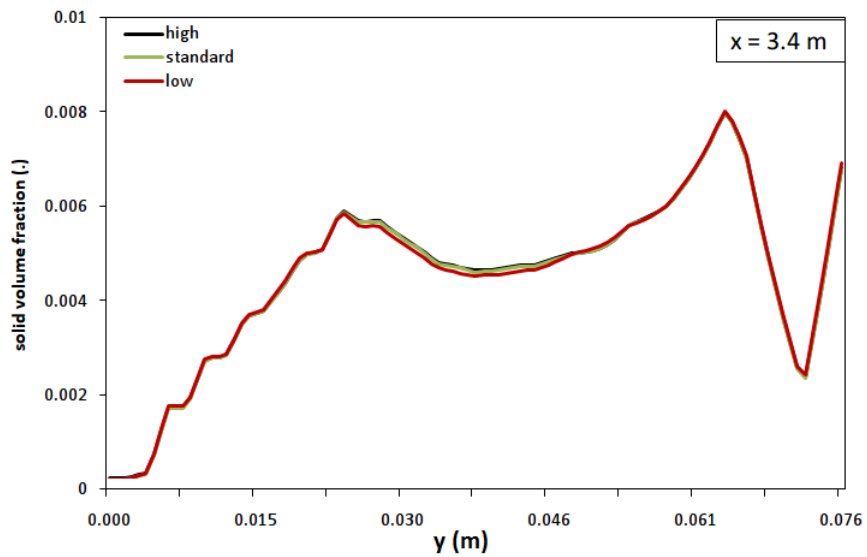


Figure 5.7: Solid volume fraction profile obtained by different initial conditions

of the computational resource, these 24 variations are simulated up to 6 s and its results are compared with each other. The objective of this comparison is in order to categorize those 24 variations into several groups which will afterwards be fully simulated up to 40 s.

				Drag model		
				Gidaspow [G]	Syamlal et al. [S]	Wen-Yu [W]
Radial Distribution Function [D]	Carnahan- Starling [D1]	Coefficient of Restitution [E]	0.84 [E2]	GD1E2	SD1E2	WD1E2
			0.70 [E3]	GD1E3	SD1E3	WD1E3
	Syamlal et al. [D2]	Coefficient of Restitution [E]	0.84 [E2]	GD2E2	SD2E2	WD2E2
			0.70 [E3]	GD2E3	SD2E3	WD2E3

Figure 5.8: The combination of simulation parameters

For the time step of 0.0001 s, the 12 variations of the simulation can be categorized into 5 typical groups as shown by Figure 5.9. The solid velocity and solid volume fraction contour in Figure 5.9 are at height of 3.4 m from the riser inlet. It can be seen that group II and group III have a similar solid volume fraction contour in which the solid phase occupies one of the side walls and almost a half of the riser cross section area. Whereas group IV and group V results tend to have a similar solid volume fraction. The solid phase in these groups scatter almost all of the cross section area of the riser. A contrasting result is shown by group I which has a less distributed solid phase. However, all of the group results show the same trend where the solid phase only exists in one of the side walls and its value is the maximum value of the solid volume fraction as shown by Figure 5.10 (refer Figure 5.3 for the highlighted position). For the solid velocity contour, all variations show that in the riser center the solid velocity is maximum. Comparing the maximum solid velocity in the riser center obtained by all variations, group I has the highest maximum solid velocity, while group V has the lowest maximum solid velocity. Figure 5.11 shows the solid velocity distribution for all variations. Comparing the contours of the solid volume fraction and the contour of the solid velocity, it shows that the contours of the solid volume fraction is very poor in terms of the symmetricity. The parameter combination of the radial distribution function of Syamlal et al. (D2) and the restitution coefficient of 0.7 (E3) tends to achieve a more uniform solid phase distribution in the riser cross section area. While the parameter combination of the radial distribution function of Carnahan-Starling (D1) and the restitution coefficient of 0.84 (E2) tends to obtain a poor solid phase distribution in the riser cross section area. Thus, the parameter combination of D2E3 may accelerate the spread of the solid phase inside the riser.

Figure 5.12 shows the solid volume fraction and solid velocity contour for 12 variations of the simulation with time step of 0.00015 s. The simulation results could be clustered into 4 groups in which group III and group IV look very similar with each other. In both groups, the solid phase occupies almost all of the cross section area of the riser and its solid velocity in the riser center is lower than the solid velocity in the riser center of the other groups, group I and group II. The group II shows a more distributed solid phase than group I in which the solid phase only exists in one side of the riser cross section. The profiles of the solid volume fraction and solid velocity for the simulation with time step of 0.00015 s are shown by Figure 5.13 and Figure 5.14, respectively.

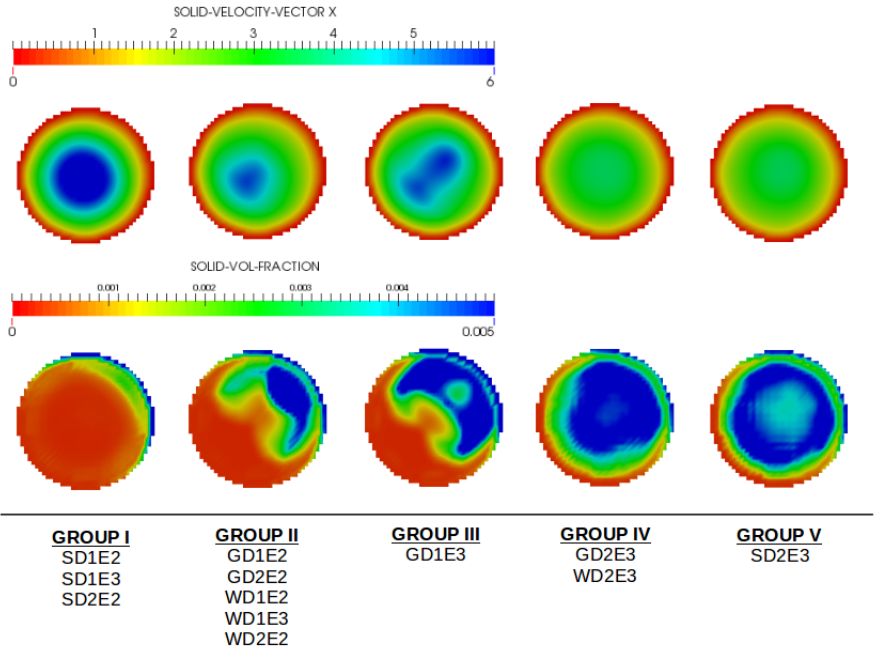


Figure 5.9: The solid velocity and solid volume fraction contour for different model combinations at time step 0.0001 s

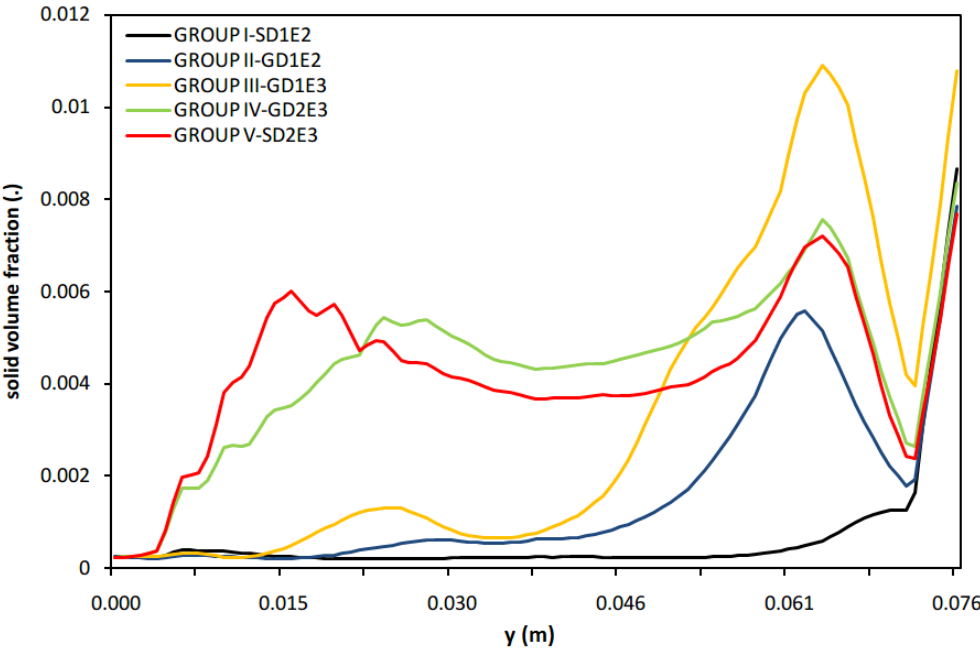


Figure 5.10: The solid volume fraction profile for different model combinations at time step 0.0001 s

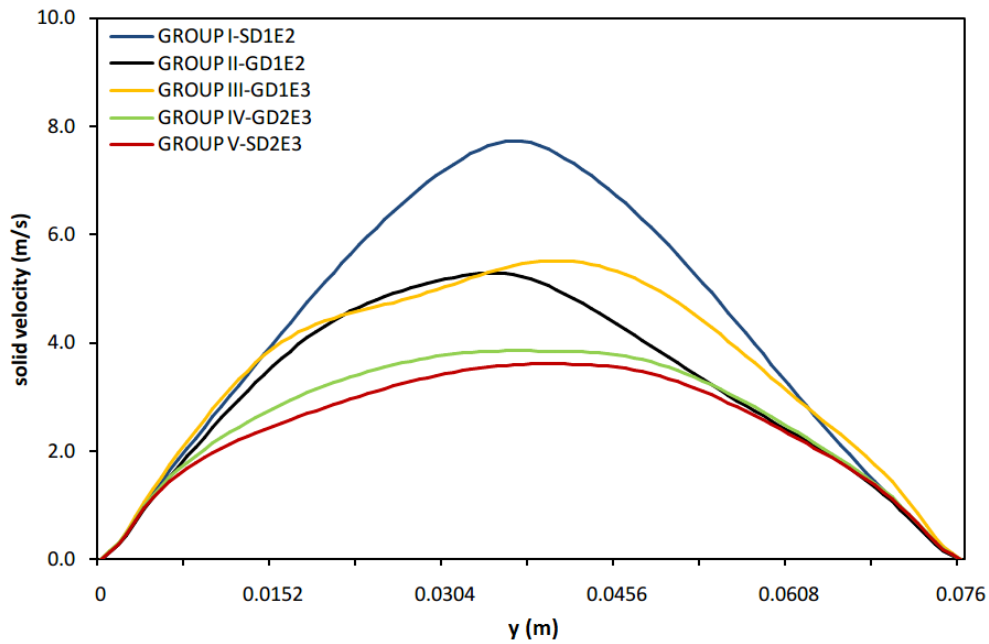


Figure 5.11: The solid velocity profile for different model combinations at time step 0.0001 s

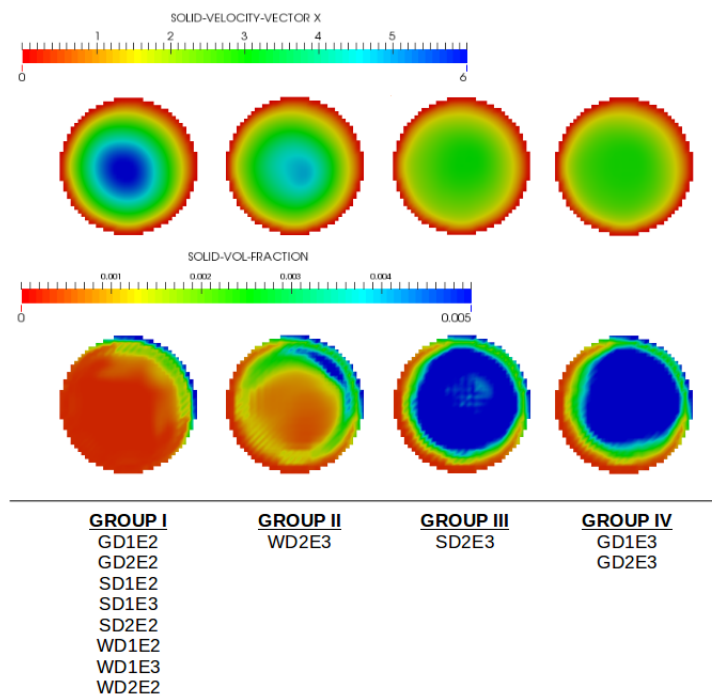


Figure 5.12: The solid velocity and solid volume fraction contour for different model combinations at time step 0.00015 s

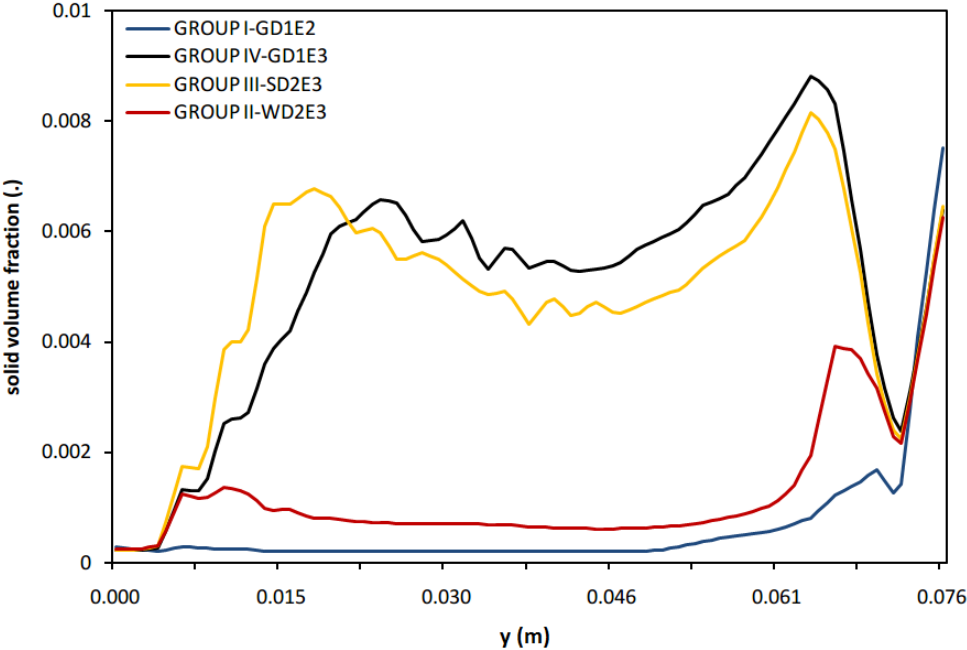


Figure 5.13: The solid volume fraction profile for different model combinations at time step 0.00015 s

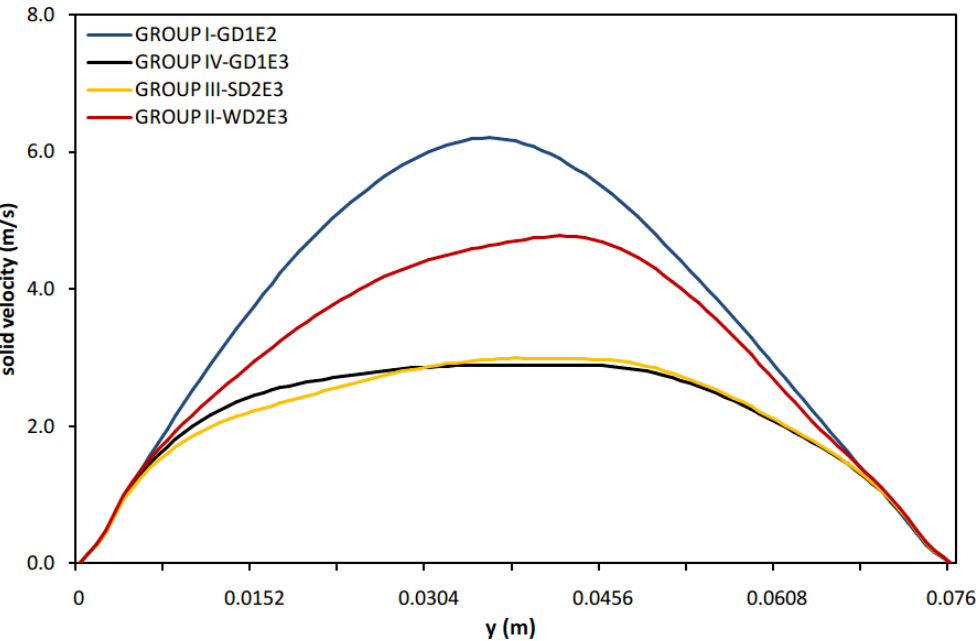


Figure 5.14: The solid velocity profile for different model combinations at time step 0.00015 s

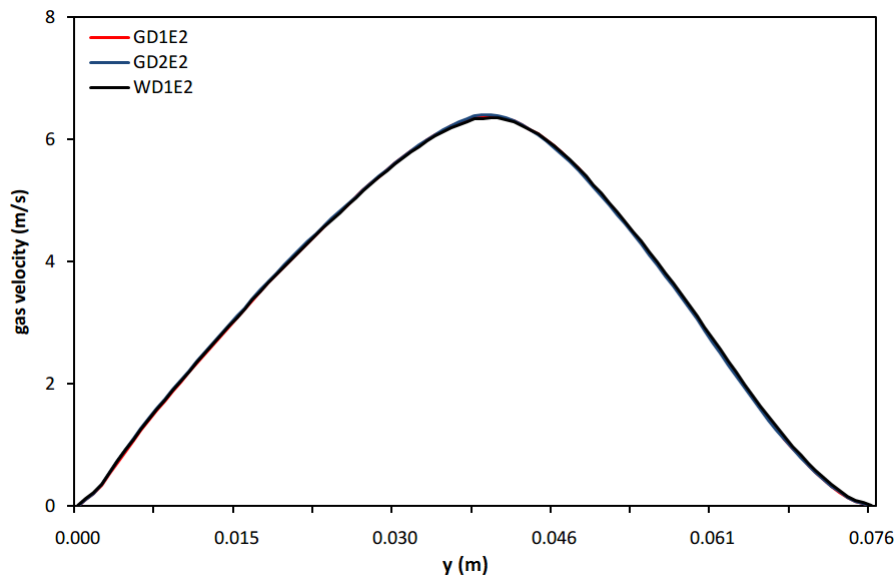


Figure 5.15: The comparison of gas velocity profile of group II after 40 s simulation with time step of 0.0001 s

In order to measure the accuracy of the above categorization, full 40 s simulations of several variations are carried out for two typical groups of time step 0.0001 s and 0.00015 s. For time step of 0.0001 s, three different variations of group II are fully simulated for up to 40 s, namely GD1E2; GD2E2; WD1E2. Figure 5.15, Figure 5.16, and Figure 5.17 show the gas velocity profile, solid velocity profile, and solid volume fraction profile of these simulations, respectively. The gas velocity profile and solid volume fraction profile show a very good agreement between the three different variations. Whereas for the solid velocity profile, a qualitatively good agreement is achieved by the three different variations. But in terms of quantitative value, a slightly different value of WD1E2 and the others is detected, especially in the area of the riser center.

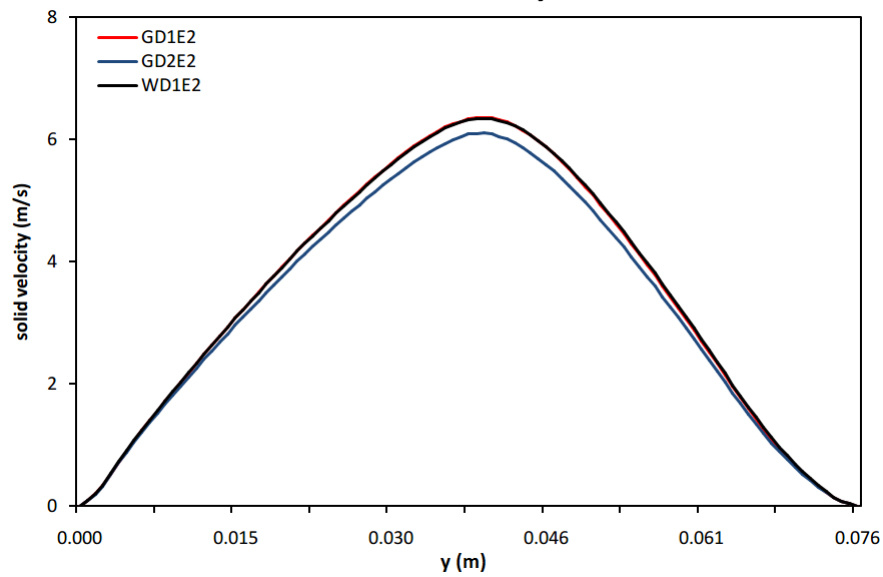


Figure 5.16: The comparison of solid velocity profile of group II after 40 s simulation with time step of 0.0001 s

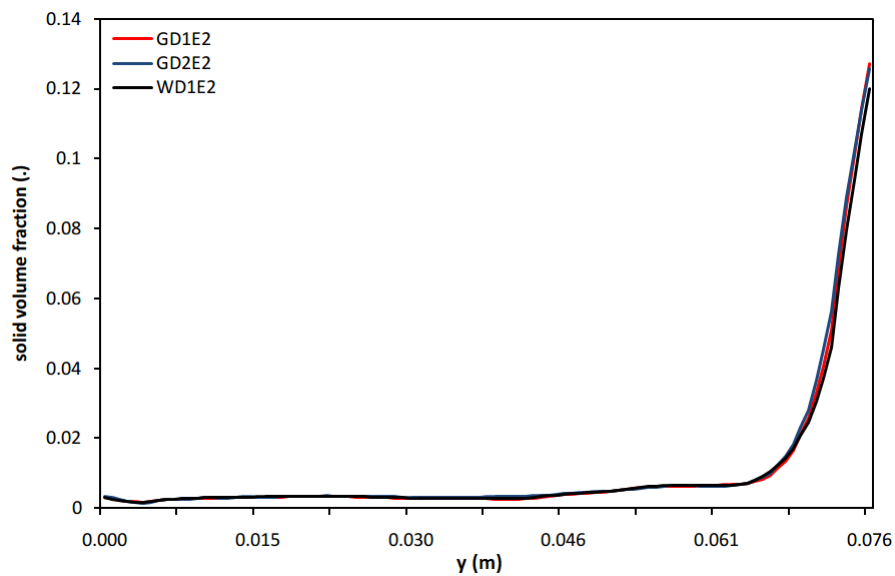


Figure 5.17: The comparison of solid volume fraction profile of group II after 40 s simulation with time step of 0.0001 s

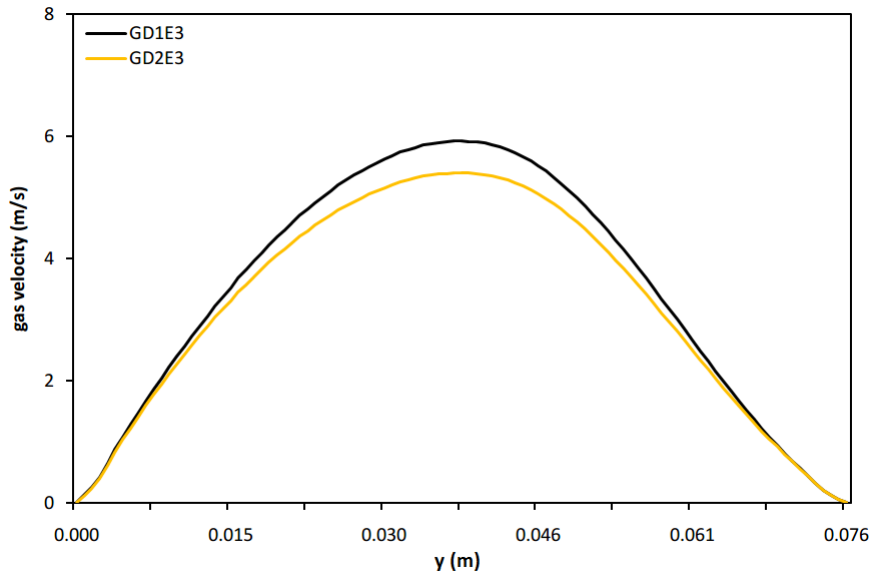


Figure 5.18: The comparison of gas velocity profile of group IV after 40 s simulation with time step of 0.00015 s

Therefore for time step of 0.00015 s, two different variations of group IV are fully simulated for up to 40 s, namely GD1E3, GD2E3. The gas velocity profile, solid velocity profile, and solid volume fraction profile of these simulations are shown by Figure 5.18, Figure 5.19, and Figure 5.20, respectively. The solid volume fraction profile shows a good agreement between the two different variations, even though in the area close to one of the side walls there is a small difference value among them. While the gas velocity profile and the solid velocity profile show that in the area of the riser center either the gas or the solid velocity of combination GD2E3 is lower than combination GD1E3. From the previous comparison of group II with simulation time step of 0.0001 s, it is observed that the velocity of combination GD2E2 is lower than combination GD1E2. These two comparisons tell a coincidence fact that the radial distribution function of Syamlal et al. (D2) obtains a lower gas and solid velocity in the area of the riser center than the radial distribution function of Carnahan-Starling (D1) does.

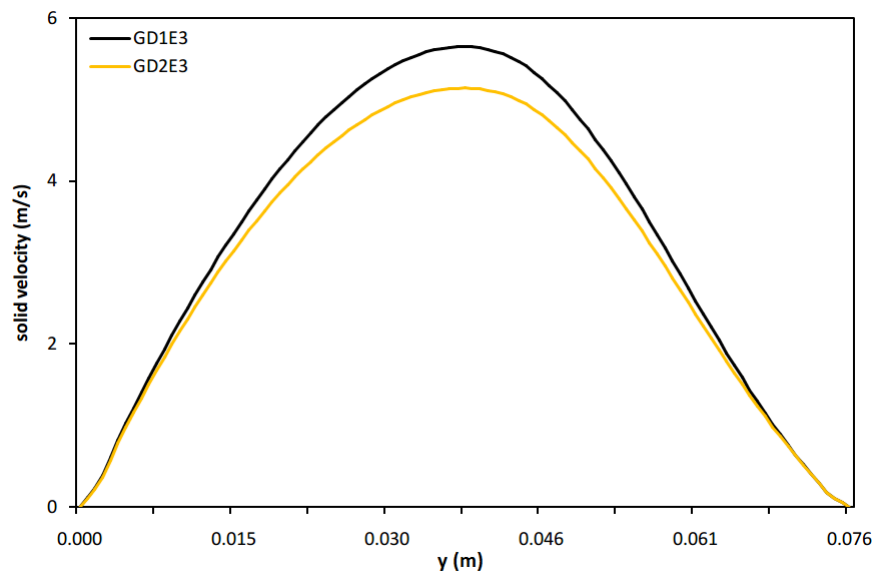


Figure 5.19: The comparison of solid velocity profile of group IV after 40 s simulation with time step of 0.00015 s

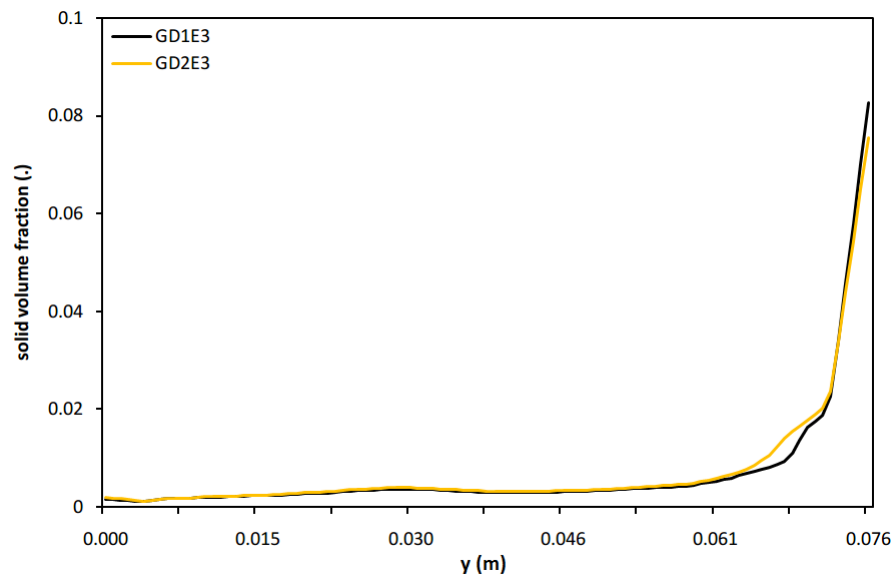


Figure 5.20: The comparison of solid volume fraction profile of group IV after 40 s simulation with time step of 0.00015 s

5.2.4 The Effect of Drag Model

In this sub-chapter, the influence of different drag models is examined. There are three different drag models that are compared in this study, namely the drag models proposed by Gidaspow [25], Syamlal et al. [68], and Wen-Yu [74]. The result of each drag model is evaluated and then compared to the other models. For each time step, three different simulations with the three different drag models are carried out for up to 40 s with the same parameters for radial distribution function and coefficient of restitution. For time step of 0.0001 s, the radial distribution function of the Carnahan-Starling model and coefficient of restitution of 0.84 are employed. Whilst the radial distribution function of the Syamlal et al. model and coefficient of restitution of 0.70 are used for the simulation with time step of 0.00015 s. For the radial distribution function of the Syamlal et al. model and coefficient of restitution of 0.84 with time step of 0.0001 s, figures in Chapter 5.2.5 show the result comparison from different drag models too.

Due to the time dependent hydrodynamics phenomena in real conditions or applications, the simulations of gas-solid riser flow are carried out in unsteady or transient conditions. The data analysis of the results obtained from simulations is usually obtained at "steady" condition which can be determined by such a parameter. In this study, the fluctuation of the solid mass flux, q_m , at the highlighted position, at height of 3.4 m above the riser inlet, is used to measure how "steady" the gas-solid flow inside the riser is. If the solid mass flux, q_m , tends to be less fluctuating then the flow seems to be at "steady" condition and vice versa. From the simulation variation of GD1E2, GD2E2, and WD1E2, Figure 5.21 shows the solid mass flux, q_m , at the highlighted position from simulation time at 30 s until 40 s. It can be seen that the solid mass flux, q_m , is less fluctuating such that the flow can be considered at "steady" condition. Thus, the time-averaged results which will be compared to experimental data of K.M. Luo [49] are obtained from the simulation time at 30 s until 40 s.

Figure 5.22 and Figure 5.23 show the contours of the solid velocity and the solid volume fraction obtained by simulation of variation GD1E2 at the planes of different height above the inlet riser ($H = 0.5, 2.0, 3.4, 5.0$ m) and at different simulation time ($t = 5, 10, 20, 40$

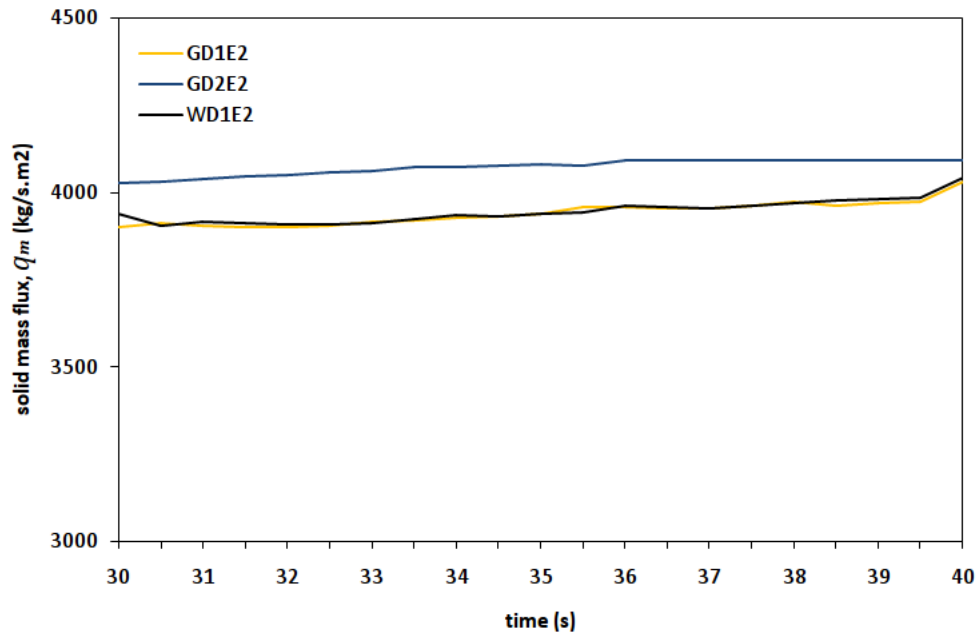


Figure 5.21: Solid phase mass flux, q_m , from 30 - 40 s at the highlighted position (at height of 3.4 m above the riser inlet)

s). From Figure 5.22 it can be seen that the higher solid velocity arises at the riser center and gradually decreases from the center to the riser wall. The contours of velocity for both phases are similar such that only one of them is shown here. Figure 5.23 shows the contour of solid volume fraction. At the simulation time of 20 s and 40 s the contours are quite similar such that assuming a "steady" condition from the simulation time of 30 s is acceptable. At the simulation time of 40 s which is assumed at "steady" flow condition, for half of the cross-sectional area, it is observed that the concentration of the solid phase in the region close to the wall is much higher than the concentration of solid phase in the riser center.

5.2.4.1 Time Step of 0.0001 s

For the simulations using the time step of 0.0001 s, Carnahan-Starling model of the radial distribution function and restitution coefficient of 0.84 are employed. Using these parameters, the simulation variations based on Figure 5.8 are GD1E2, SD1E2, WD1E2 for Gidaspow, Syamlal, and Wen-Yu drag model, respectively. Figure 5.24, Figure 5.25, and Figure 5.26 are

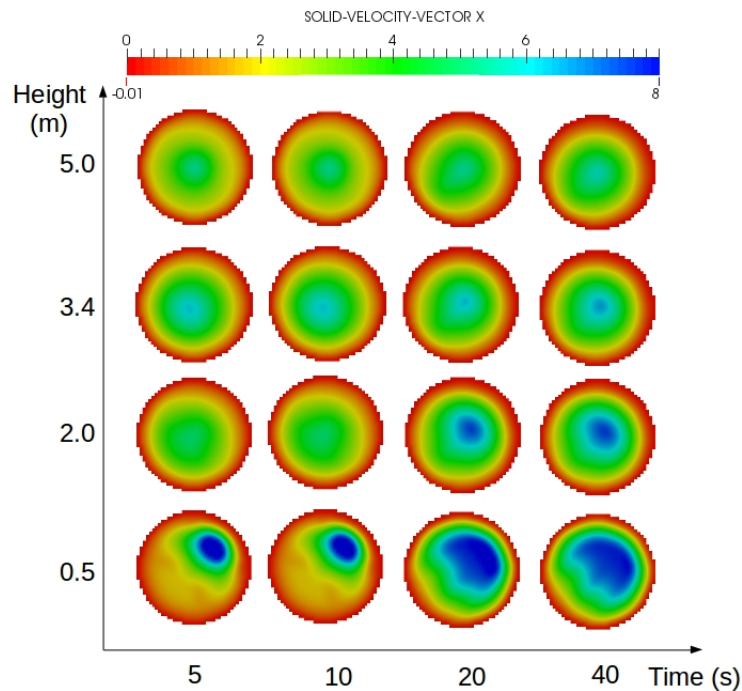


Figure 5.22: Solid velocity contour at different time and riser height
[based on Gidaspow drag model]

the time-averaged radial profiles of the axial gas velocity, the axial solid velocity, and the solid volume fraction from the simulations with time step of 0.0001 s, respectively. From Figure 5.24, it is shown that all different drag models have a symmetrical profile of the gas velocity. The gas velocity profile resulted by Gidaspow and Wen-Yu model coincide with each other while Syamlal model generates a higher value profile in general. Comparing the simulation results to the experimental data of K.M. Luo, notable discrepancies between all simulations with different drag models and the experiment are discovered even though at some points they coincide. These diverging results could be induced by several factors such as the employed mathematical model and a less fine enough grid near the side wall that significantly affects the flow around the riser wall.

Figure 5.25 shows the comparison of the time-averaged radial profiles of the axial solid velocity in which all different drag models have a symmetrical profile. It is observed that all simulations have a similar velocity profile as the experimental data but quantitatively there is a significant difference between simulations and experimental results. The simulation

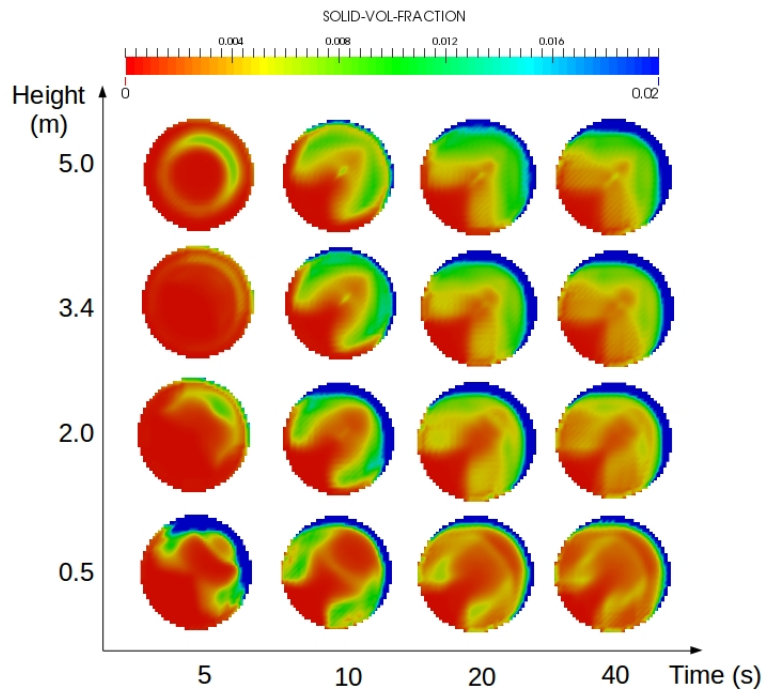


Figure 5.23: Solid volume fraction contour at different time and riser height
[based on Gidaspow drag model]

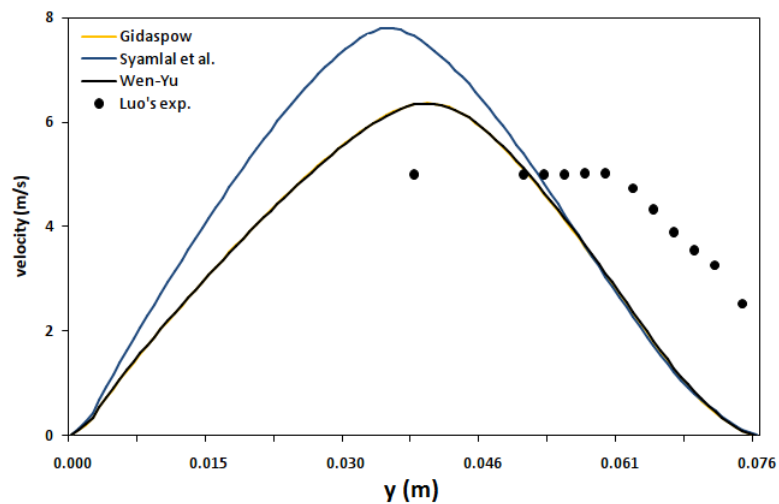


Figure 5.24: Time-averaged of gas phase velocity profiles for simulations with different
drag models and time step of 0.0001 s

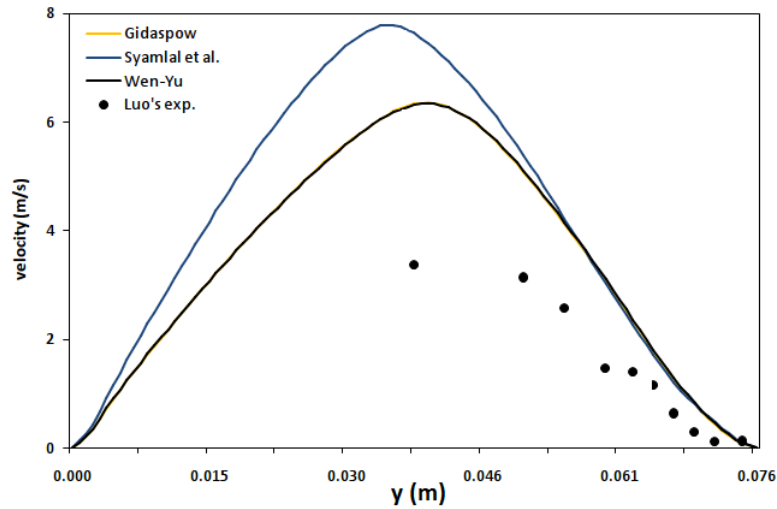


Figure 5.25: Time-averaged of solid phase velocity profiles for simulations with different drag models and time step of 0.0001 s

values are higher than the experimental data especially in the riser center region. In the region close to the wall, the simulation results are close to the experimental result. As the gas velocity profile, the solid velocity profiles of Gidaspow and Wen-Yu model coincide while the profile resulted by Syamlal model has higher values than the two other models.

The comparison of the time-averaged radial profile of the solid volume fraction is represented by Figure 5.26. In general, the simulation using Gidaspow and Wen-Yu model have a good agreement with the experimental result while the simulation using Syamlal model predicts a lower value than the experimental result. It shows that the three different drag models obtained non-symmetrical solid volume fraction profile in which a denser solid volume fraction was captured only in one of the riser walls. This phenomenon could be the outcome of geometrically improper inlet conditions for the solid phase.

Figure 5.27, Figure 5.28, and Figure 5.29 show the contour of gas velocity, the contour of solid velocity, and the contour of solid volume fraction at different height of riser at simulation time of 40 s. At that time, the riser condition is assumed to be in "steady" condition. The gas velocity and solid velocity contours are very similar with each other. This phenomenon might be due to the drawback of the current solution algorithm when dealing with the momentum transfer between gas and solid phases. When solving the momentum equations

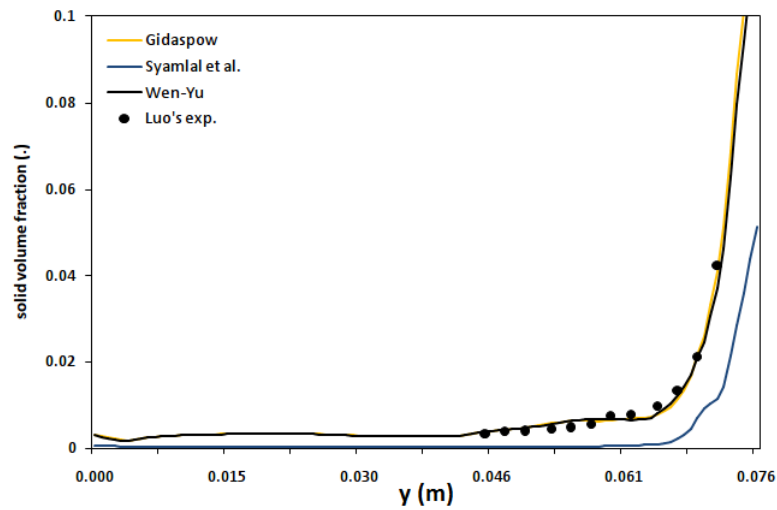


Figure 5.26: Time-averaged of solid volume fraction profiles for simulations with different drag models and time step of 0.0001 s

for both phases, step 3 of the solution algorithm in sub-chapter 4.1, the momentum transfer between gas and solid phases is explicitly included as the source term. The problem arises when calculating the momentum transfer between two phases due to its dependency on the relative velocity between two phases. This problem occurs when determining the coefficient of the momentum transfer or the drag force (step 2 of the solution algorithm in sub-chapter 4.1) too. In this study, for solving the momentum equations for both phases at n^{th} time step, the relative velocity between two phases is calculated based on the gas and solid velocities from the previous time step, $(n - 1)^{th}$ time step, because the gas and solid velocities for n^{th} time step are not solved yet.

Generally for all properties it is observed that the contours produced by Gidaspow model and Wen-Yu model are very similar. Except for the contour of solid volume fraction, a such symmetrical contour is found at height of 3.4 m and 5.0 m for the gas and solid velocity. For the solid volume fraction, in general the solid concentration in the region close to the wall is much higher than the solid concentration in the riser center. None of the drag models captures a symmetrical solid volume fraction contour. At height of 3.4 m, the drag models of Gidaspow and Wen-Yu show that about 65% of the riser walls are occupied by a high concentration of the solid phase. While Syamlal drag model only captures about 30% of the riser walls which are infested by highly concentrated solid phase.

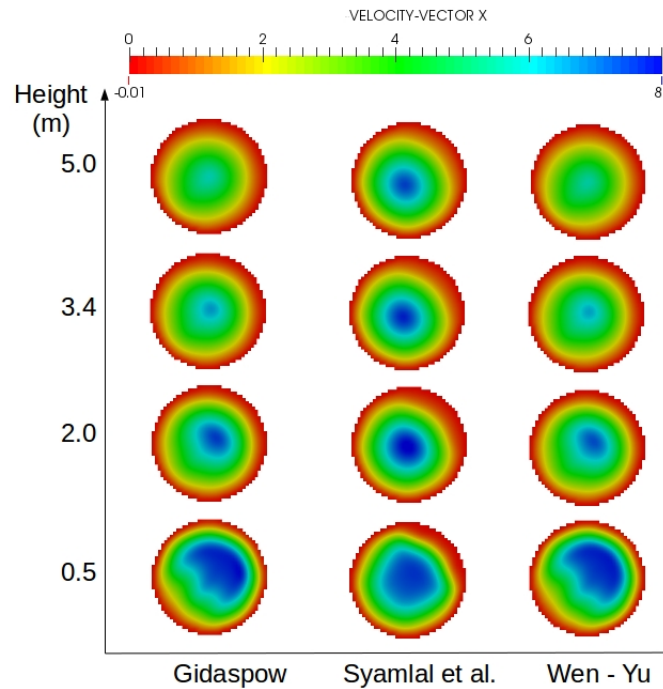


Figure 5.27: Comparison of the gas velocity distribution at time=40 s for simulations with different drag models and time step of 0.0001 s

5.2.4.2 Time Step of 0.00015 s

For the simulations using the time step of 0.00015 s, the radial distribution function of Syamlal model and coefficient of restitution of 0.70 are used. Using these parameters, the simulation variations based on Figure 5.8 are GD2E3, SD2E3, WD2E3 for Gidaspow, Syamlal, and Wen-Yu drag model, respectively. Figure 5.30, Figure 5.31, and Figure 5.32 are the time-averaged radial profiles of the axial gas velocity, the axial solid velocity, and the solid volume fraction from the simulations with time step of 0.00015 s, respectively. Figure 5.30 tells that Gidaspow model and Wen-Yu model have a symmetrical profile of the gas velocity while for Syamlal et al. model an asymmetric gas velocity profile is captured. The Gidaspow model has the highest value than the two other models, Syamlal et al. model and Wen-Yu model. Comparing the simulation results to the experimental data of K.M. Luo, significant differences between all simulation variations and the experimental data are discovered. The value of Gidaspow model is close to the experiment even though the profile does not fit with each other, whilst the two other variations underestimate the experimental value.

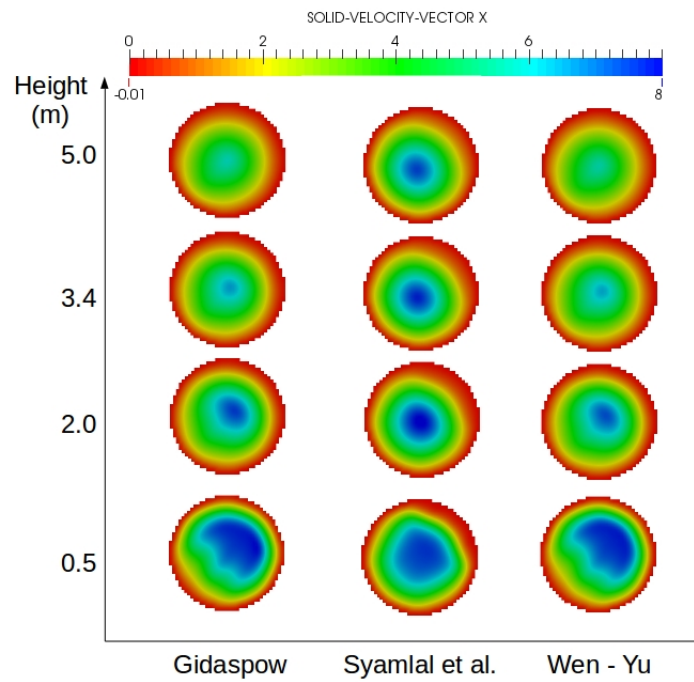


Figure 5.28: Comparison of the solid velocity distribution at time=40 s for simulations with different drag models and time step of 0.0001 s

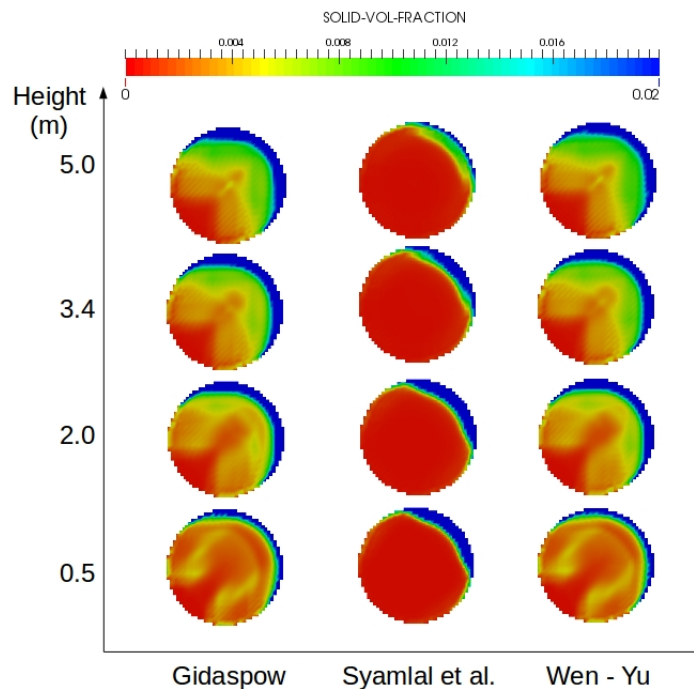


Figure 5.29: Comparison of the solid volume fraction distribution at time=40 s for simulations with different drag models and time step of 0.0001 s

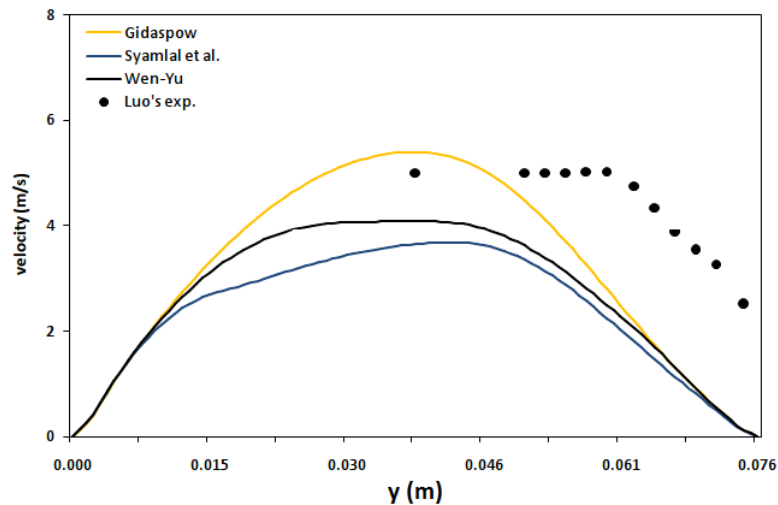


Figure 5.30: Time-averaged gas phase velocity profiles for simulations with different drag models and time step of 0.00015 s

Figure 5.31 shows the comparison between the time-averaged radial profile of the axial solid velocity of the simulations and the experiment of K.M. Luo. In general the solid velocity profile calculated by the simulation is similar to the gas velocity profile. It can be recognized from Figure 5.31 that the result obtained by Syamlal et al. model has a quantitatively good agreement with the experimental data. The Wen-Yu model obtains a close result to the experiment, too. Furthermore, a symmetrical profile and an overestimated result are achieved by Gidaspow model.

The comparison of the time-averaged radial profile of the solid volume fraction is represented by Figure 5.32. In general, the simulations using Gidaspow and Syamlal et al. model obtain a close result to the experimental result while the simulation using Wen-Yu model achieves a lower value than the experimental result. Figure 5.32 shows that the three different drag models obtain a denser solid volume fraction in the region close to the wall than in the riser center. However, the radial solid volume fraction obtained by the simulations does not show a symmetrical profile.

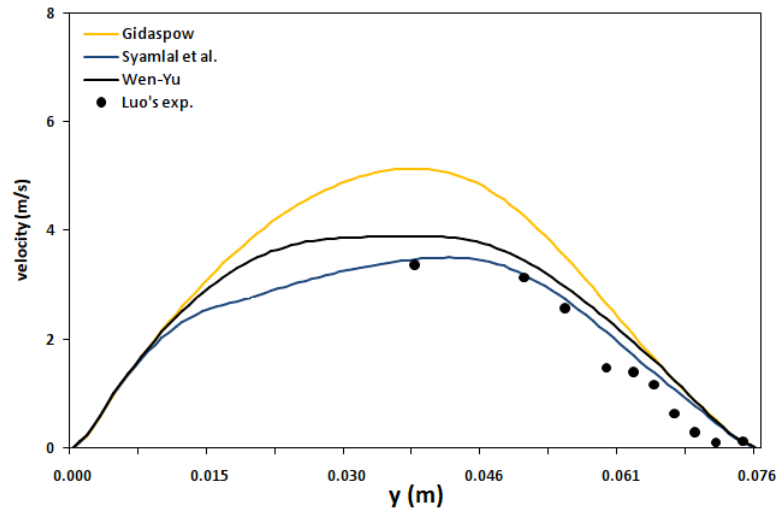


Figure 5.31: Time-averaged solid phase velocity profiles for simulations with different drag models and time step of 0.00015 s

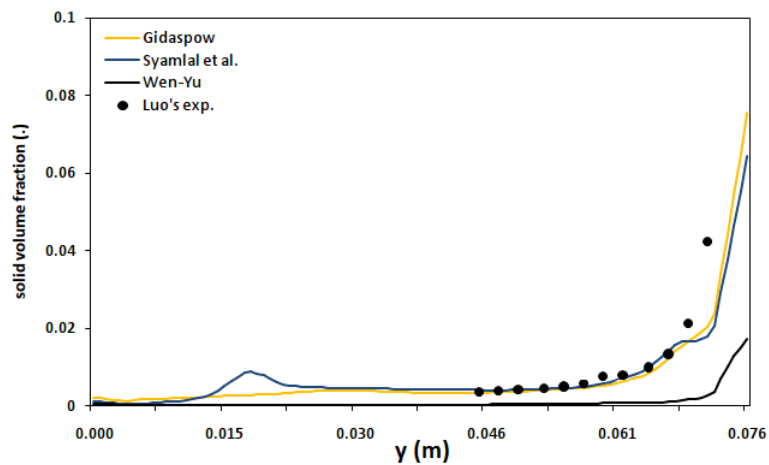


Figure 5.32: Time-averaged solid volume fraction profiles for simulations with different drag models and time step of 0.00015 s

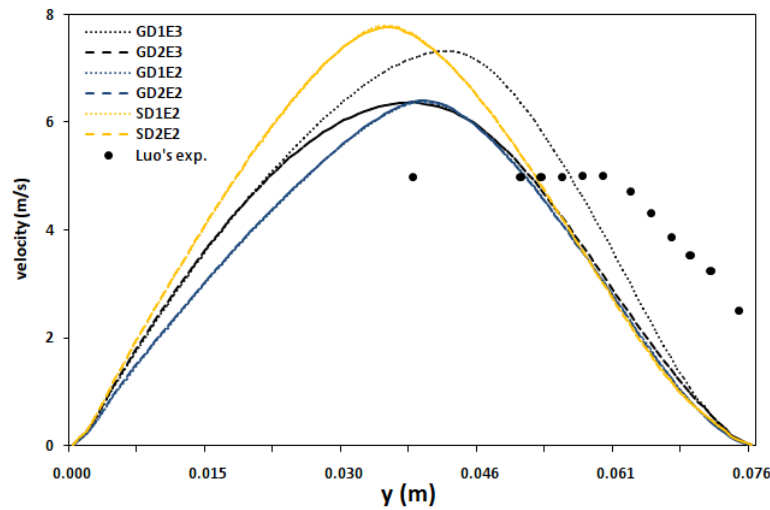


Figure 5.33: Time-averaged gas phase velocity profile for simulations with different models of radial distribution function and time step of 0.0001 s

5.2.5 The Effect of Radial Distribution Function Model

There are two different models utilized to calculate the radial distribution function, namely Carnahan-Starling model and Syamlal et al. model. This section tries to analyse the effect of different models of the radial distribution function. The analysis is based on six different simulations with time step of 0.0001 s. The comparison of the radial profile of the axial gas velocity and the radial profile of the solid volume fraction are shown by Figure 5.33 and Figure 5.35, respectively. From these two comparison figures a similar fact is found. The simulations which use the coefficient restitution of 0.84 (E2) are not dependent on the utilised model for calculating the radial distribution function. Both Carnahan-Starling model (D1) and Syamlal et al. model (D2) yield almost the same value either for the axial gas velocity and the solid volume fraction. Therefore, the radial profile of GD1E2 coincides with the radial profile of GD2E2 and the radial profile of SD1E2 coincides with the radial profile of SD2E2. Whilst the simulation that uses the coefficient restitution of 0.7 (E3), the effect of different models for radial distribution function is significant in which Carnahan-Starling model has a higher value either for the axial gas velocity or the solid volume fraction (in the area close to the wall, 0.076 m) than Syamlal et al. model has, as shown by Figure 5.33 and Figure 5.35.

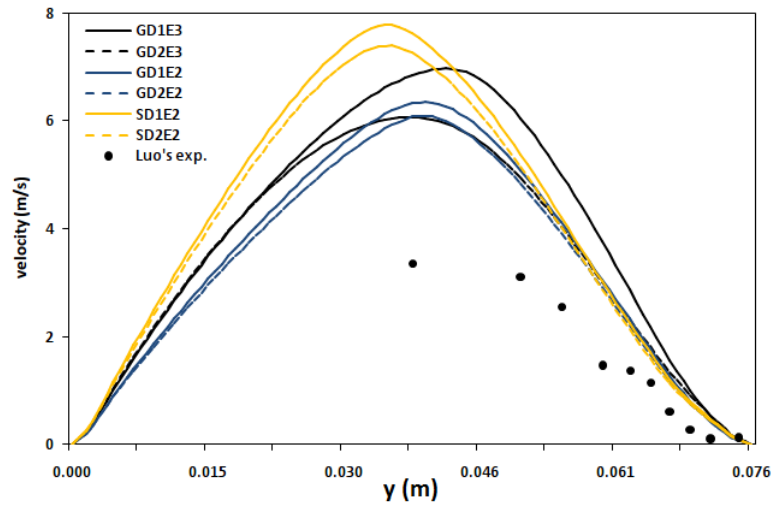


Figure 5.34: Time-averaged solid phase velocity profile for simulations with different models of radial distribution function and time step of 0.0001 s

For the radial profile of axial solid velocity as presented by Figure 5.34, the simulations which employ the coefficient restitution of 0.84 (E2) qualitatively have a good agreement. Both Carnahan-Starling model (noted as D1) and Syamlal et al. model (D2) yield the same profile as shown by the variation of GD1E2-GD2E2 and the variation of SD1E2-SD2E2. While the utilisation of the coefficient of restitution of 0.7 results in a significant difference between the different models of the radial distribution function, especially in the area close to the riser center. By analyzing Figure 5.33, 5.34, and 5.35, utilizing the coefficient of restitution (CoR) of 0.7 results in a significant difference between the different models of the radial distribution function. Using CoR of 0.7 means the solid particles have less kinetic energy after inter-solid particle collision than using CoR of 0.84. With its less kinetic energy, the solid particles tend to be less moving randomly. This condition will increase the solid volume fraction at certain location. Regarding Figure 3.4, the value of the different radial distribution function will differ more significant when the value of solid volume fraction increase. Thus, it will change the gas-solid flow behavior inside the riser.

In addition, an interesting fact is revealed in this radial distribution function model examination. Generally a good agreement either for the axial gas velocity profile, the axial solid velocity profile, or the solid volume fraction profile between GD1E2-GD2E2 and SD1E2-SD2E2 confirms that the categorization of 24 variations into several groups as discussed

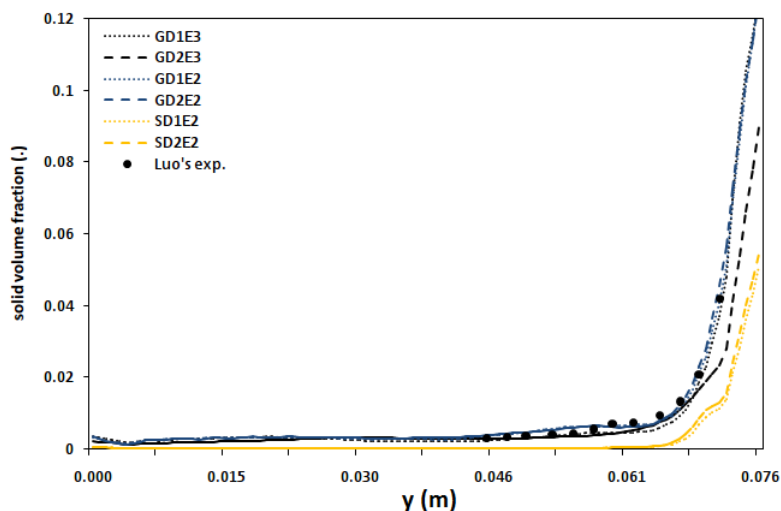


Figure 5.35: Time-averaged solid volume fraction profile for simulations with different models of radial distribution function and time step of 0.0001 s

in section 5.2.3 maybe accurate enough to predict the similarity of the hydrodynamics behaviour of such a fully simulated system (the simulation that reaches steady condition). From section 5.2.3, the simulation variation of GD1E2-GD2E2 are categorized into Group II while the simulation variation of SD1E2-SD2E2 are typically included into Group I as listed by Figure 5.9. After a full 40 s simulation, either the simulation variation of GD1E2-GD2E2 and the simulation variation of SD1E2-SD2E2 show good agreement of the results. Thus, the categorization as discussed in section 5.2.3 is valid enough to cast the steady behaviour of the riser flow hydrodynamics.

5.2.6 The Effect of Restitution Coefficient Value

The current section discusses the effect of restitution coefficient between solid particles. The inter-particle coefficient of restitution is an important parameter in computational fluid dynamics which utilize the kinetic theory of granular flow models. The coefficient is a measurement characteristic of the elasticity degree of the solid particle collisions. The coefficient value could be determined from zero for representing perfectly inelastic collisions to one for elastic collisions. In this study, two different values of coefficient of restitution are employed for simulating the gas solid riser flow, namely 0.7 and 0.84. Figure 5.36 shows the radial profile of the solid volume fraction for three different simulation variations. Listed in

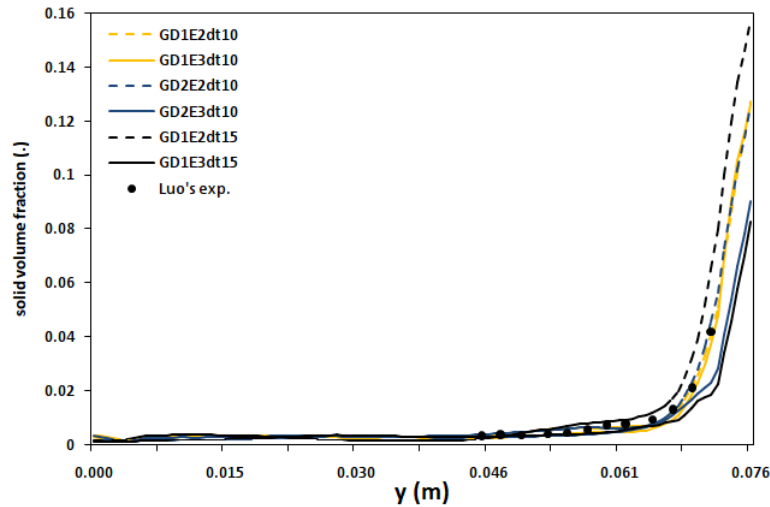


Figure 5.36: Time-averaged solid volume fraction profile for simulations with different restitution coefficients and time steps

Figure 5.8, the simulation variations with E2 mean the restitution coefficient of 0.84 while E3 represents the restitution coefficient of 0.7. From Figure 5.36 it can be recognized that the increase of the restitution coefficient leads to an increase of the solid volume fraction in the area close to the riser wall. This result is in a good agreement with the conclusions by Pita and Sundaresan [57] and the simulation result by Xi Gao et al. [22]. In addition, an increase in the restitution coefficient will generally increase the granular temperature as shown by Figure 5.37. Using a high value of the restitution coefficient means the dissipation of fluctuating energy due to particle-particle collision will decrease considerably. Figure 5.37 tells that the granular temperature is very low in the dense flow regions.

5.2.7 The Effect of Simulation Time Step

In this study, two different simulation time steps are employed, namely 0.0001 s and 0.00015 s. This section tries to examine the effect of different simulation time steps on the calculation result. Three different simulation variations are calculated and then their results are compared, i.e. GD1E2, GD1E3, GD2E3. Figure 5.38 and Figure 5.39 show the comparison of the radial profile of the time-averaged axial gas velocity and the radial profile of the time-averaged axial solid velocity. From both radial profiles, it explains that the variation of GD1E2 is less dependent to the simulation time step because its profile for simulation

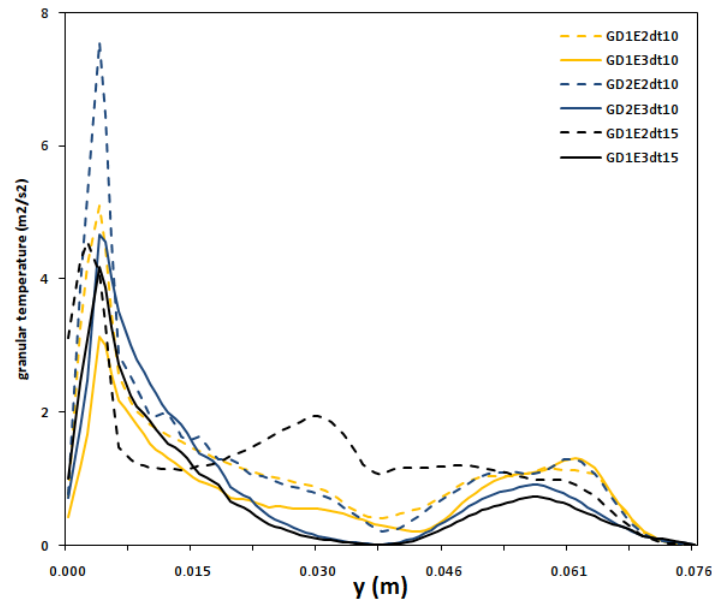


Figure 5.37: Time-averaged granular temperature profile for simulations with different restitution coefficients and time steps

time step of 0.0001 s and time step of 0.00015 s almost coincide. Whereas for the variation of GD1E3 and GD2E3, the differences of the values are significant in which the simulation time step of 0.0001 s captures a higher velocity than the time step of 0.00015 s does.

Furthermore, the comparison of the radial profile of solid volume fraction is shown by Figure 5.40. In the area close to the riser center, generally there is not an obvious difference between the different time steps. But from the riser center to the area close to the riser wall (0.076 m), the discrepancy between the results of the two different time steps is evident. The variation of GD1E2 predicts a higher solid volume fraction resulted by the time step of 0.00015 s. In contrary for the variation of GD1E3 and GD2E3, the time step of 0.0001 s produces a higher solid volume fraction in the area close to the riser wall (0.076 m). From these three radial profile comparisons it can be resumed that the effect of different simulation time steps depends on the combination of the simulation parameters.

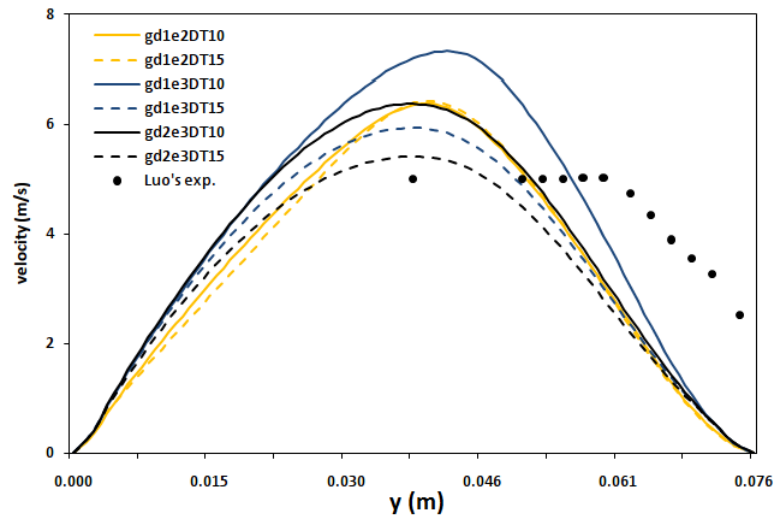


Figure 5.38: Time-averaged gas phase velocity profile for simulations with different time steps

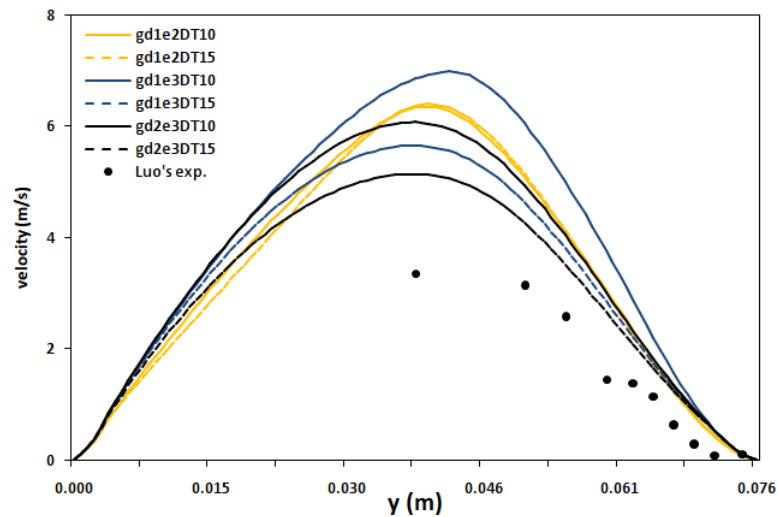


Figure 5.39: Time-averaged solid phase velocity profile for simulations with different time steps

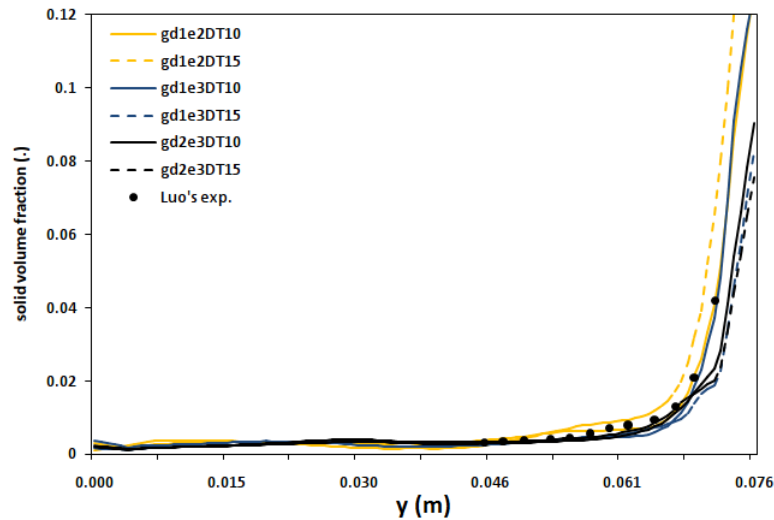


Figure 5.40: Time-averaged solid volume fraction profile for simulations with different time steps

5.2.8 Comparison of the Current Simulation with L. Cabezas's Result

In this study, in total there are 13 simulation variations depending on the used simulation parameters as listed in Figure 5.8 that are fully simulated up to 40 s. From these 13 simulations, the best four simulation variations which have better agreement to the experimental result than the other variations have been identified. These four variations are SD2E3; GD2E3 with the simulation time step of 0.00015 s and SD2E3; GD2E2 with 0.0001 s as the simulation time step. The experiment of K.M Luo [49] was already simulated by L. Cabezas-Gomez et al. [10]. In this section the comparison between three different results, namely the results achieved by the experiment of K.M Luo [49], the simulation of L. Cabezas-Gomez et al. [10], and the current simulations, is presented. In addition, there are some fundamental differences between the current simulation and L. Cabezas-Gomez et al. simulation [10]. The simulation of L. Cabezas-Gomez et al. [10] was carried out on a two-dimensional (2D) domain. Instead of using the kinetic theory of granular flow (KTGF), they applied a conventional approach or empirical approach in order to determine the solid viscosity and solid pressure. A constant solid viscosity which was obtained by an experimental measurement is utilised. The solid phase pressure was modelled using the empirical correlation of Jayaswal [32]. The drag model proposed by Gidaspow [25] was employed to calculate the

momentum transfer between gas phase and solid phase. In the momentum equation of the solid phase, the role of the gas phase pressure was ignored.

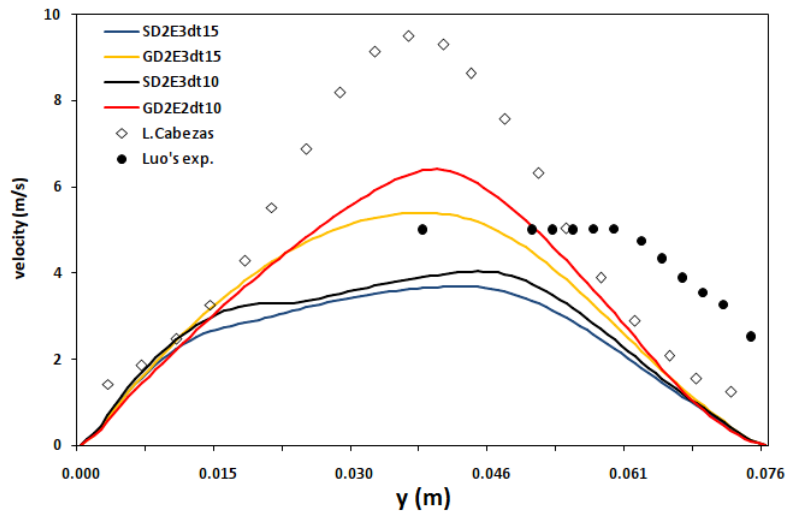


Figure 5.41: Time-averaged gas phase velocity profile comparison between L. Cabezas-Gomez et al. [10] and the current study

Figure 5.41, Figure 5.42, and Figure 5.43 are the results of the comparison of the axial gas velocity, the axial solid velocity, and the solid volume fraction, respectively. Comparing the best variations of the current simulation to the simulation of L. Cabezas-Gomez et al., a better time-averaged radial profile of the axial gas velocity results is achieved by the current simulation. The radial gas velocity profile of the current simulations has much less deviation to the experimental result than the simulation of L. Cabezas-Gomez et al. has as shown in Figure 5.41.

Figure 5.42 shows the comparison of the time-averaged radial profile of the axial solid velocity of the current simulations with L. Cabezas-Gomez et al. simulation. At least two significant diversities are found. The first, the overall value of the solid velocity profile of the current simulations is higher than the simulation of L. Cabezas-Gomez et al. The second, the simulation of L. Cabezas-Gomez et al. clearly shows the presence of an annular flow pattern with negative solid velocity in the regions close to the wall, even though this is not obviously seen on the experiment of K.M. Luo. The simulation of L. Cabezas-Gomez et al. captured the annular flow phenomenon in the riser. The annular flow pattern is characterized by two phenomena, namely a denser solid fraction in the region close to the wall than in the riser center and a negative solid velocity in the regions close to the wall.

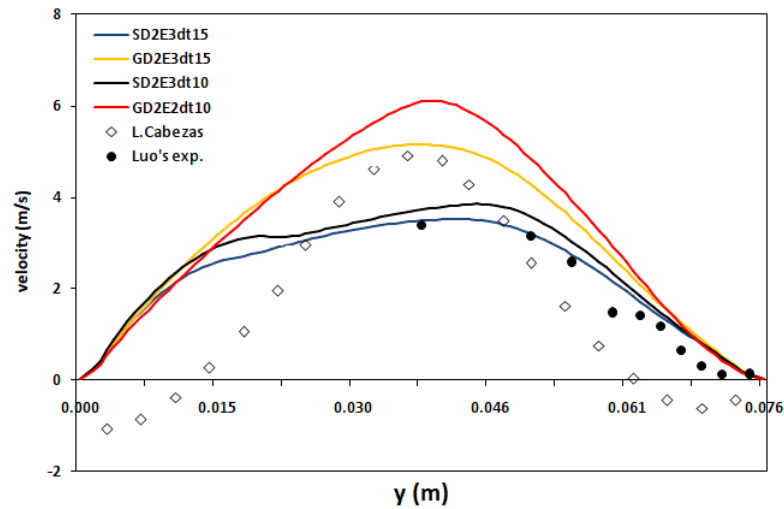


Figure 5.42: Time-averaged solid phase velocity profile comparison between L. Cabezas-Gomez et al. [10] and the current study

The comparison of the time-averaged radial profile of the solid volume fraction is presented by Figure 5.43. In general, the current simulation has a better agreement with the experimental result than the simulation of L. Cabezas-Gomez et al. has. It shows a dense area with a high solid concentration near to the wall as obtained by experiment. However, the radial solid volume fraction obtained by the current simulations does not show a symmetrical profile. As mentioned earlier in this chapter the experimental data by K.M. Luo was measured from one side of the riser to its center only. Therefore, it is not certain that the experimental data were symmetric. Whereas the simulation of L. Cabezas-Gomez et al. indicates a symmetrical radial profile of the solid volume fraction although its value in the region close to the wall does not fit well to the experiment.

5.2.9 Comparison of Laminar and Turbulent Simulation

From the previous laminar simulations, some remarks could be concluded as follows: the simulation parameters of GD2E3 predicts the experimental data of the gas velocity profile a bit better than the simulation parameters of SD2E3 as presented in Figure 5.41, Figure 5.42 shows that the simulation parameters of SD2E3 achieves a much closer result to the experimental data than the simulation parameters of GD2E3, while Figure 5.43 shows that the simulation parameters of GD2E3 and SD2E3 obtain almost the same result. From these

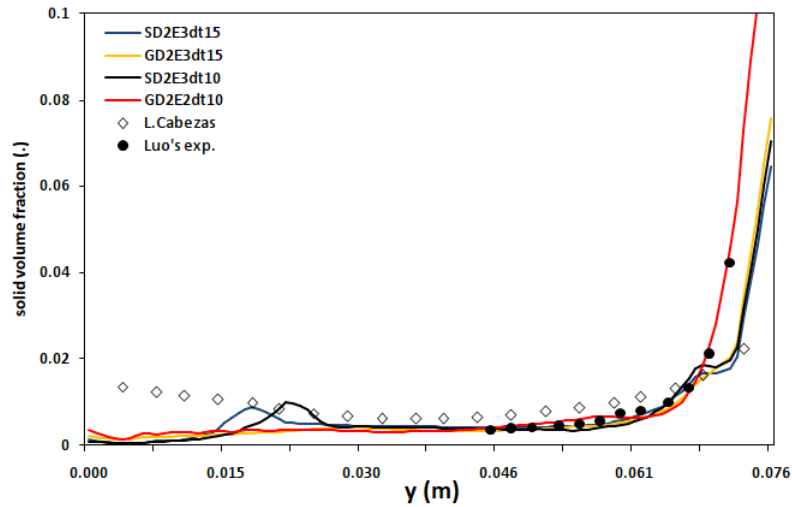


Figure 5.43: Time-averaged solid volume fraction profile comparison between L. Cabezas-Gomez et al. [10] and the current study

remarks, the simulation parameters of SD2E3 that means the used parameters are the drag force model of Syamlal et al. (S), the radial distribution function of Syamlal et al. (D2), and the restitution coefficient of 0.7 (E3) is then employed for the turbulent simulation too. Using the time step of 0.00015 s, the simulation results of the laminar and turbulent simulation are then compared with each other.

Figure 5.44 shows the comparison of time-averaged gas velocity profiles for laminar and turbulent simulation. The turbulent simulation obtains a symmetric gas velocity profile while the laminar simulation profile is an asymmetric profile. The value of turbulent simulation is closer to the experiment than the laminar simulation, even though the turbulent profile does not fit with the experimental value. While the laminar value underestimates the experimental value. From this comparison, the turbulent simulation achieves a better result of the gas velocity profile than the laminar simulation.

The comparison of the time-averaged solid velocity profile between the laminar and turbulent simulation is shown by Figure 5.45. It can be recognized from Figure 5.45 that the result obtained by the laminar simulation has a quantitatively good agreement with the experimental data. Furthermore, a symmetrical profile and an overestimated result are achieved by the turbulent simulation. Either the laminar or the turbulent simulation does not capture

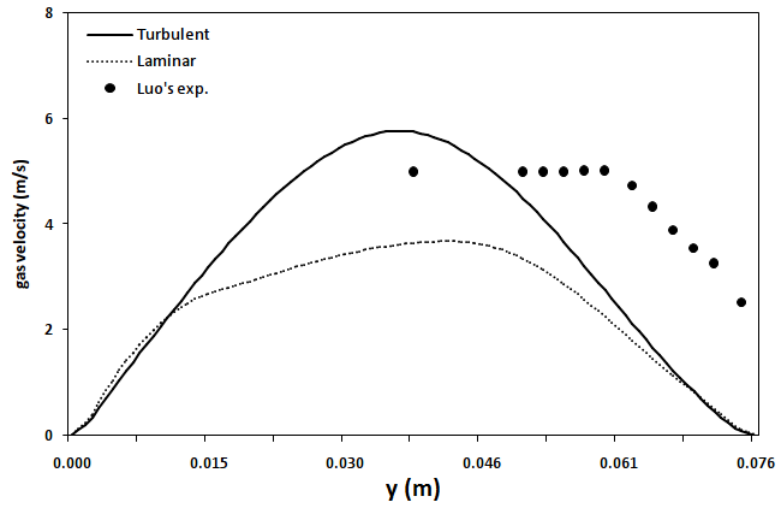


Figure 5.44: Time-averaged gas phase velocity profiles for laminar and turbulent simulation

a solid down flow phenomenon at the riser wall. Generally, it can be concluded that the laminar simulation captures a better result for the solid velocity profile than the turbulent simulation. Comparing the velocity profile, either gas or solid phase, it can be recognized that the profiles of laminar and turbulent simulation are not similar. The reason behind this should be studied intensively. But one possible reason may correlate to the turbulence model used. In this study, the $k - \epsilon$ turbulence model, Equation 3.57 and 3.58, are employed. But in these equations, the effect of dispersed solid particles on the gas phase turbulent kinetic energy and dissipation rate is not accounted yet. Thus, it may improve the simulation result once the effect of disperse solid particles is included into the equations (called as the $k - \epsilon$ dispersed model). Another possibility for improving the simulation result is by utilizing the $k - \epsilon$ per phase model in which the turbulent kinetic energy and dissipation rate are calculated for both phases.

From Figure 5.44 and 5.45, the gas velocity and solid velocity contours are very similar with each other. This phenomenon might be due to the drawback of the current solution algorithm when dealing with the momentum transfer between gas and solid phases. When solving the momentum equations for both phases, step 3 of the solution algorithm in subchapter 4.1, the momentum transfer between gas and solid phases is explicitly included as the source term. The problem arises when calculating the momentum transfer between two phases due to its dependency on the relative velocity between two phases. This problem

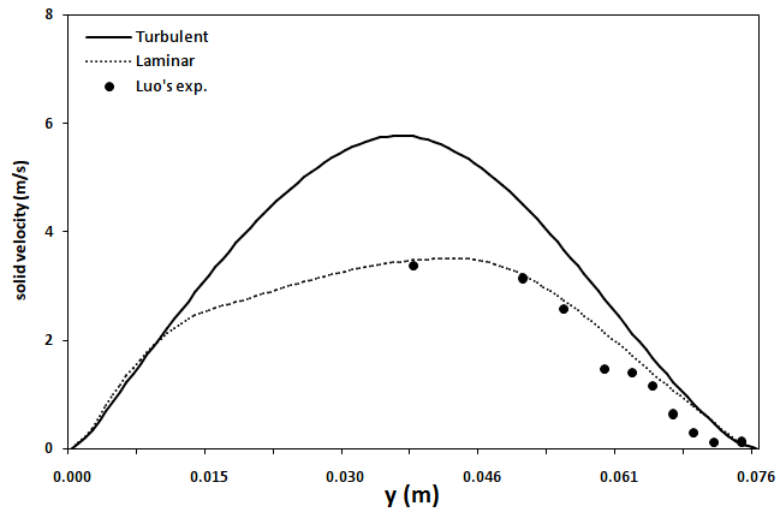


Figure 5.45: Time-averaged solid phase velocity profiles for laminar and turbulent simulation

occurs when determining the coefficient of the momentum transfer or the drag force (step 2 of the solution algorithm in sub-chapter 4.1) too. In this study, for solving the momentum equations for both phases at n^{th} time step, the relative velocity between two phases is calculated based on the gas and solid velocities from the previous time step, $(n - 1)^{th}$ time step, because the gas and solid velocities for n^{th} time step are not solved yet.

The comparison of the time-averaged solid volume fraction is represented by Figure 5.46. In general, both simulations obtain a close result to the experimental data. But there is a noticeable fact in the area near the riser wall. A significant discrepancy of the solid volume fraction value between the laminar and turbulent result is captured. The turbulent simulation obtains a higher solid volume fraction at the riser wall, 0.12, than the laminar simulation, 0.065. This might be due to the deficiencies of the near-wall turbulence model. Furthermore, the solid volume fraction profiles obtained by both simulations do not show a symmetrical profile.

Figure 5.47 shows the contour of the solid velocity, Figure 5.47(a), and the contour of the solid volume fraction, Figure 5.47(b), at the simulation time of 40 s. The contours are captured from the riser cross section area that is located at 3.4 m above the riser inlet. As previously discussed, the solid velocity of the turbulent simulation shows a more symmetrical

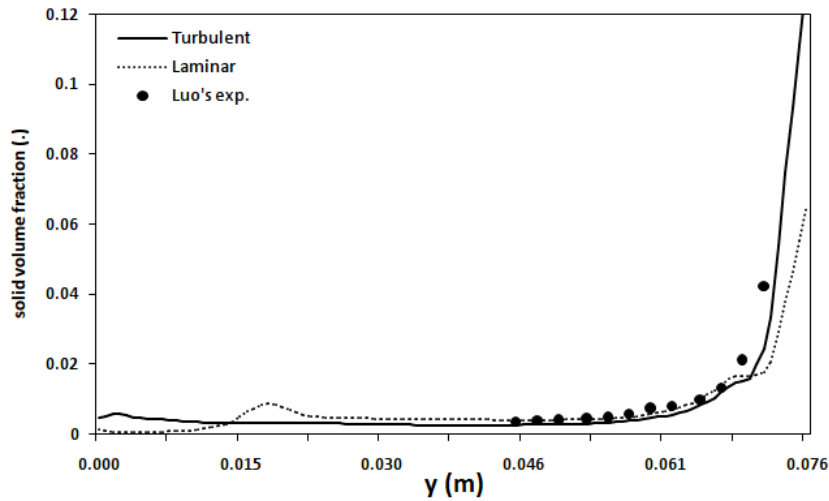


Figure 5.46: Time-averaged solid volume fraction profiles for laminar and turbulent simulation

contour than the laminar simulation. For the solid volume fraction, in general the solid concentration in the region close to the wall is much higher than the solid concentration in the riser center. Neither laminar nor turbulent simulation captures a symmetrical solid volume fraction contour. The turbulent simulation shows that about 65% of the riser walls are occupied by a high solid phase concentration. While the laminar simulation only captures about 40% of the riser walls which are filled by highly concentrated solid phase. Thus, by using the turbulent model the spread of the solid phase is more prevalent in the riser wall than with the laminar model.

5.2.10 Discussion

5.2.10.1 Wall Boundary Condition

There are several alternatives of wall boundary conditions that could be employed in the simulation. In gas-solid riser flow simulation, three commonly used boundary conditions are no-slip, free-slip and partial-slip boundary condition. The same or different boundary conditions may be implemented for both phases. In the present study no-slip boundary condition is used for both phases. Using this boundary condition, the current simulation fails to capture the core-annulus flow in the riser. Shah et al. [62] reported that the selec-

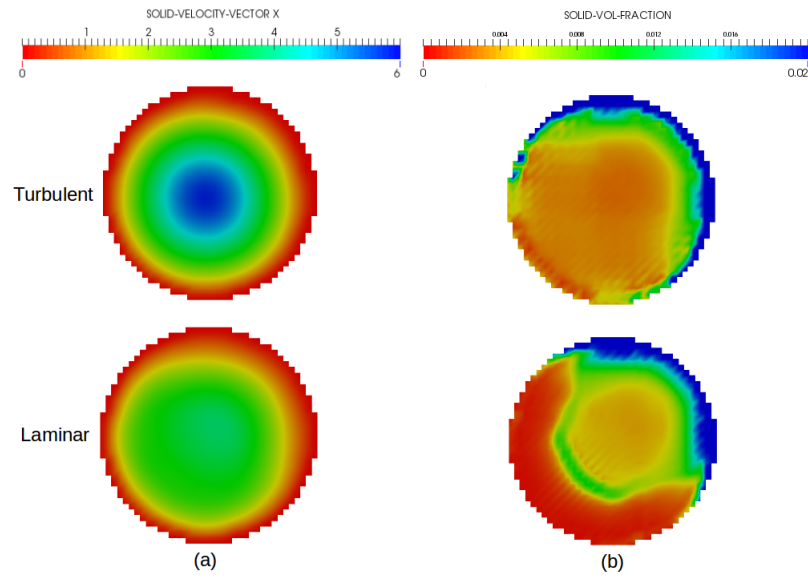


Figure 5.47: Comparison of the solid velocity and the solid volume fraction distribution at time=40 s between turbulent and laminar simulation

tion of the wall boundary conditions for the solid phase rules the solid velocity and solid volume fraction near the wall such that an appropriate wall boundary condition is very critical for capturing the core-annulus phenomenon. The report notes an important point in which many previous studies utilized the Johnson and Jackson [35] wall boundary condition for the solid phase in simulating gas solid riser flow. Using the Johnson and Jackson wall boundary condition a core-annulus flow is successfully recognized in the riser.

The Johnson and Jackson boundary condition is adopted to describe the solid particle-wall interactions. The wall shear contributed by the solid phase is generated by rate of axial momentum transferred to the wall by the solid particles in a thin layer adjacent to the wall surface [35]. Using this boundary condition, the wall shear contributed by the solid phase is formulated as :

$$\mu_m \frac{\partial U_m}{\partial n} = \frac{U_{m,t} \sqrt{3\theta} \phi \rho_m \varepsilon_m g_0}{6\varepsilon_{m,max}} \quad (5.2)$$

where $U_{m,t}$, ε_m , $\varepsilon_{m,max}$ are the tangential velocity of the solid phase at the wall, the solid volume fraction, and the maximum solid volume fraction, respectively. μ_m , θ , ρ_m , g_0 , n are solid phase viscosity, solid granular temperature, solid density, radial distribution function,

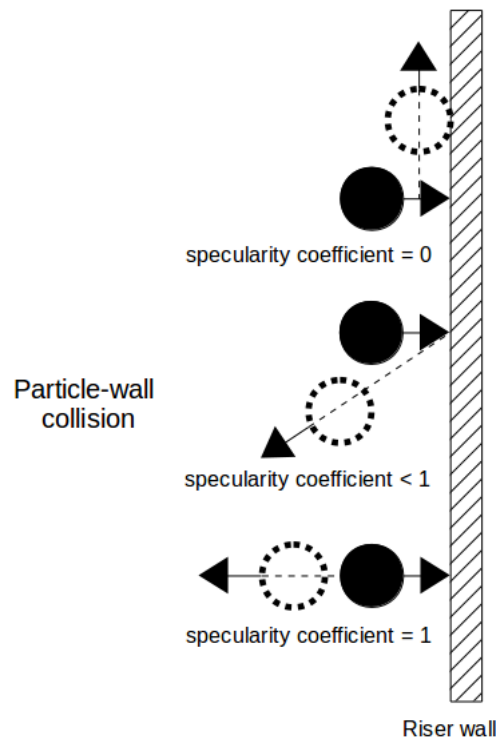


Figure 5.48: A suggested wall boundary condition

and normal of the wall surface, respectively [35]. φ is the specularity coefficient which is an empirical parameter quantifying the nature of solid particle-wall collisions and it describes the average tangential momentum transfer from solid particle to the wall. Its value range is from 0 to 1 depending on the solid particle and the wall properties such as the wall roughness. The specularity coefficient of 0 means perfect specular collisions or denotes free slip wall. Using this value, after the collisions, the solid axial velocity at the wall is 0 while the solid tangential velocity at the wall is greater than 0, as shown by Figure 5.48 (the post-collision of the solid motion is shown by the dash line). While the specularity coefficient of 1 describes perfectly diffuse collisions or no-slip wall (even though the study by Zhong [80] suggests that it is not recommended to describe the specularity coefficient of 1 as no-slip solid phase wall boundary condition). From figure 5.48, for the specularity coefficient of 1, the post-collision of the solid motion shows the solid axial velocity at the wall is greater than 0 while the solid tangential velocity at the wall is 0. Many researchers have reported that the value of specularity coefficient on the solid phase wall boundary condition strongly affects the predicted hydrodynamic behaviour in gas-solid riser flow.

5.2.10.2 Drag Model

In the present study, three different drag models are examined, namely Wen-Yu model; Gidaspow model; and Syamlal et. al model. These three drag models are conventionally employed for gas solid riser flow simulation. The Wen-Yu drag model is an empirical correlation that was derived from experimental observations on settling velocities of a single solid particle in the liquid. The Gidaspow drag model utilises Wen-Yu model for dilute conditions, $\varepsilon_g > 0.8$, and Ergun model for $\varepsilon_g < 0.8$. The Ergun model is calculated from an experimental study on pressure drops inside the packed bed of solids. Either Wen-Yu model or Gidaspow model uses the drag model for single solid particles derived by Schiller and Naumann [61] to calculate drag force of a multi-particle system in riser. Comparing Wen-Yu model and Gidaspow model, for dilute condition when $\varepsilon_g > 0.8$, both models use the same empirical correlation in calculating the drag force because Gidaspow model is adopted from Wen-Yu model for dilute conditions. From Figure 5.24, Figure 5.25, and Figure 5.26 in section 5.2.4 it can be seen that the radial profile from Wen-Yu model (WD1E2) and Gidaspow model (GD1E2) coincide.

Furthermore, the Syamlal et al. drag model is determined from two correlation equations by Richardson and Zaki [58] and Garside and Al-Dibouni [23]. The correlation equation by Richardson and Zaki [58] is a correlation between ratio of terminal velocity of multi-particle to that of single particle with the gas volume fraction. While the correlation equation by Garside and Al-Dibouni [23] is about the correlation between ratio of terminal velocity of multi-particle to that of single particle and particle Reynolds number. The Syamlal et al. model employs a drag model for single solid particle derived by Dallavalle [15] to calculate drag model of multi-particle system in riser.

The discrepancy of the results between the experimental data and the present simulation could be attributed to the lack of the conventional drag models used in the simulation in taking into account the presence of solid clusters near riser wall. Several previous studies have shown the existence of solid cluster formation in gas solid riser flow [27, 78, 79]. These clusters interact with the surrounding dilute phase. The presence of clusters may lead to a higher pseudo solid diameter and then the terminal velocity of solid clusters becomes

higher. Some reports said that this leads to down flow of solid phase and higher segregation of the solids near the wall [52, 53]. In order to overcome the drawback of conventional drag models in considering the cluster presence, an alternative drag model called the energy minimization multi-scale (EMMS) model is proposed [45, 46]. This alternative drag model divides the gas solid mixture condition in the riser into three different pseudo levels. The first level is the dilute phase which represents individual solid particles in the gas phase, the second level is the dense phase that indicates solid particles and gas remaining inside clusters, and the third level is the suspended cluster which reflects an entity of a solid particle package as a cluster moving in the gas phase. All the pseudo levels are calculated using conventional Wen-Yu drag model with differences in considering the particle diameter for Wen-Yu model. The first and second pseudo levels use the solid particle itself as the particle diameter for Wen-Yu model, while the third pseudo level uses the cluster diameter. The cluster diameter can be estimated by a semi-empirical expression which its detail can be found in Sreekanth Pannala et al. [65]. Thus, implementing the EMMS drag model may improve the simulation results of the present study in the future.

5.2.10.3 Gas Phase Viscous Model

In gas solid riser flow simulation, calculating the viscous stress or the viscosity of the gas phase relies on two different models, namely the laminar and the turbulent model. The laminar model is usually dedicated to a smooth flow with low Reynolds number. While for a chaotic flow with high Reynolds number, the turbulent model is applied. In real applications or implementations, the structure of the gas-solid flow in the riser is the combination between dense and dilute region. In the dilute region, the gas flow is expected to be in turbulent condition, whilst in the dense region with a high solid volume fraction; a narrow distance between particles; a boundary layer around cluster, the gas flow maybe in laminar or turbulent condition. For the gas phase, the characteristic length for the Reynolds number is the riser diameter such that the gas phase Reynolds number could vary from $10e+4$ to $10e+6$ which means the gas flow is in the turbulent regime. Whilst for the solid phase, using solid particle diameter as the characteristic length of Reynolds number, the solid phase Reynolds number is less than 100 and it yields a laminar regime [62]. However, in the dense region, the gas velocity could be very low due to solid particle resistance and then the gas phase

flow becomes laminar. Thus, these two different regimes, laminar and turbulent, coexist in the riser. These complex situations are the argument of using either laminar or turbulent model for calculating the gas phase viscous stresses in computational fluid dynamics. In the present study, the laminar model is utilised to calculate the gas viscous stress for all 13 variations of full 40 s simulations.

In order to have a confidence level in utilizing the laminar model, the observation of previous studies is necessary. Benyahia et al. [7] have observed two different gas-solid turbulence models, namely the model of Balzer et al. [3] and the model of Cao and Ahmadi [12], and the laminar model. The investigation has found only small diversity in radial profiles predicted between the turbulent and laminar calculation. Another comparison of predicted profiles between turbulent and laminar has been summarized by Almuttahir and Taghipour [1]. The report explains that radial distributions of the solids volume fraction calculated by the laminar model are closer to the experimental results than those from the turbulent model. For all properties, the comparisons show that the laminar model simulations have a better agreement with the experimental data [1]. Shah et al. [63] have also compared the laminar and turbulent simulation for gas-solid flow in a riser. The conclusion is that either laminar or turbulent model produce reasonable agreement with the experimental data.

6 Numerical Simulation of 3D Gas-Solid Flow in Rectangular Riser

6.1 Simulation Parameters

The test case for gas-solid multiphase flow simulation in this chapter is based on the experiments of J. Zhou et al. [81] and its simulation by Tingwen Li et al. [47]. The case is a 3D-rectangular riser and the detailed simulation parameters are listed in Table 6.1. The geometry of the simulation test case is shown by Figure 6.1, while Figure 6.2 shows the rectangular meshing of the computation domain. The details of boundary conditions (BC) of the simulation, namely inlet BC, outlet BC, wall BC, for gas and solid phases are explained below.

- a The inlet boundary conditions for gas and solid phases and its properties are listed below:

Gas phase

$$\mu_g : 1.82 \times 10^{-5} \text{ kg m}^{-1} \text{ s}^{-1}$$

$$\rho_g : 1.225 \text{ kg m}^{-3}$$

$$\varepsilon_g : 0.90$$

$$U_{g,x} : 5.5 \text{ m s}^{-1}$$

Solid phase

$$d_m : 213 \text{ } \mu\text{m}$$

$$\rho_m : 2640 \text{ kg m}^{-3}$$

$$\varepsilon_m : 0.10$$

$$U_{m,x} : 0.1515 \text{ m s}^{-1}$$

Concerning the riser dimension and the uniform inlet gas velocity entering the riser, it shows that the gas flow is turbulent due to its Reynolds number is 5.43×10^4 . This bed riser is then identified as the turbulent bed regime. Regarding the properties of the solid phase, it can be concluded that the used solid particle is classified as Geldart particle Group B.

b Outlet boundary condition:

The zero gradient at outlet for any property is set up as the outlet boundary condition as expressed by Equation 6.1

$$\left(\frac{\partial \alpha}{\partial x_i} \right)_{outlet} = 0 \quad (6.1)$$

where α is the respective property or variable.

c Wall boundary condition:

For both phases, gas and solid phase, a no slip boundary condition is utilized.

Table 6.1: Simulation parameters of 3D gas-solid flow in rectangular riser

Parameter	
Riser geometry (rectangular)	0.146x0.146x9 m
Meshing (cells)	146168
Flow condition	transient (unsteady)
Time step (s)	0.00015
Time interval of simulation (s)	0-40
Range of time-averaged results (s)	30-40
Drag model model	Syamlal et al.
Radial distribution model	Syamlal et al.
Restitution coefficient	0.7
Gas phase viscous	laminar

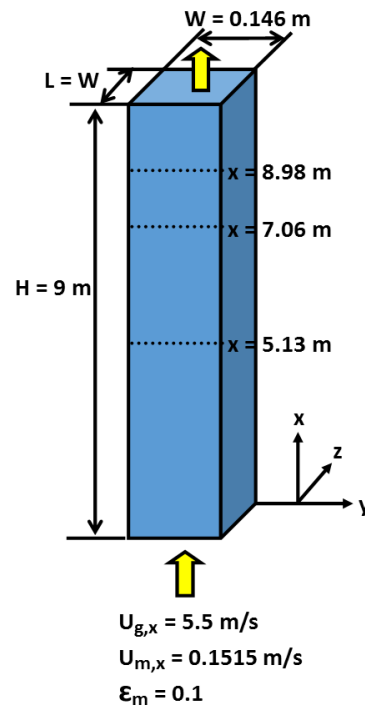
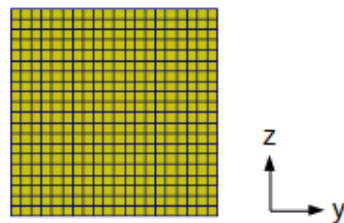


Figure 6.1: Geometry and boundary conditions used in simulations

Figure 6.2: Domain meshing in y,z -plane

6.2 Simulation Results and Discussion

The simulation is carried out from 0 s to 40 s using Syamlal et al. drag model, the radial distribution function of Syamlal et al., the restitution coefficient of 0.7, and time step of 0.00015 s. The simulation is computed on a single computer. The simulation result from 30-40 s is then averaged in order to be compared with the experiment by J. Zhou et al. [81]. The comparisons of numerical results with experimental data are made using lateral profiles of the solid phase velocity and lateral profiles of the gas volume fraction.

6.2.1 Solid Velocity Lateral Profile

The time-averaged lateral profiles of the solid velocity are examined at 5.13 m above the inlet riser as shown by Figure 6.3. At this position, two different lateral profiles of the solid velocity at $z=0.073$ m and 0.1 m are highlighted as shown by Figure 6.4. For $z=0.073$ m, an asymmetric solid velocity profile is captured, as shown by "sim.1". While for $z=0.1$ m, the solid velocity profile is presented by "sim.2" and it is an asymmetric solid velocity profile as well. Comparing the simulation results to the experimental data of J. Zhou et al. [81], significant differences are discovered for both positions. The simulation result overestimates the experimental value at both positions, namely "exp.1" and "exp.2". Furthermore, the simulation is not able to capture the solid down flow phenomenon near the wall. In general, a poor agreement between the simulation prediction and the experiment is achieved for the lateral profile of the solid velocity.

One possible reason of these discrepancies is the coarse nature of the grid and probably the flow properties of the inlet boundary condition. In this study, the number of cells for the calculated domain is 146168. Using this mesh, the calculation time for 40 s simulation is about 40 days. Increasing the number of cells such that the mesh becomes finer will absolutely increase the simulation time. This drawback can be solved if the simulation is performed on a parallel computer. From the experiment, the solid mass flux is the only available data at the inlet for the solid phase. During the simulation, if the solid volume fraction of the inlet boundary condition is too low then the solid velocity of the inlet boundary condition becomes higher than the actual solid velocity. This situation leads to a higher solid velocity

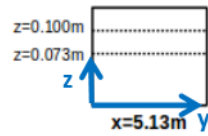


Figure 6.3: The highlighted position for capturing the solid phase velocity profiles

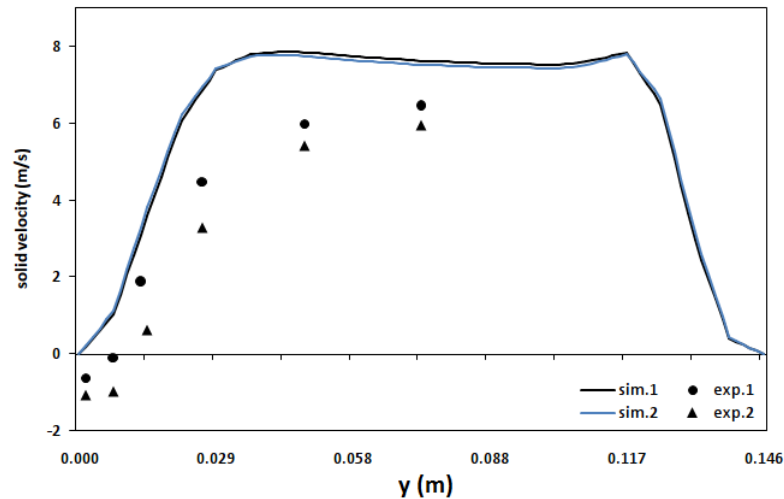


Figure 6.4: Time-averaged lateral profiles of the solid phase velocity at $z=0.073$ m and 0.1 m as shown by Figure 6.3

inside the riser due to a higher solid flow momentum at the inlet. In this study, the solid volume fraction of the inlet boundary condition is set up as 0.1, based on the work of Tingwen Li et al. [47]. Increasing the solid volume fraction of the inlet boundary condition may decrease the solid velocity inside the riser such that the simulation prediction can be closer to the experiment. As discussed in Chapter 5, the drag model and the wall boundary condition may also contribute to the poor prediction of the simulation to the experiment of J. Zhou et al. [81].

6.2.2 Gas Volume Fraction Lateral Profile

This sub-chapter compares the time-averaged lateral profiles of the gas volume fraction between the simulation prediction and the experiment at $z=0.073$ m as shown by Figure 6.5. At this position, two different lateral profiles of the gas volume fraction at $x=7.06$ m and $x=8.98$

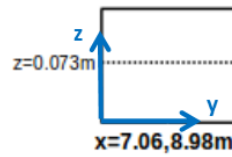


Figure 6.5: The highlighted position for capturing the gas volume fraction lateral profiles

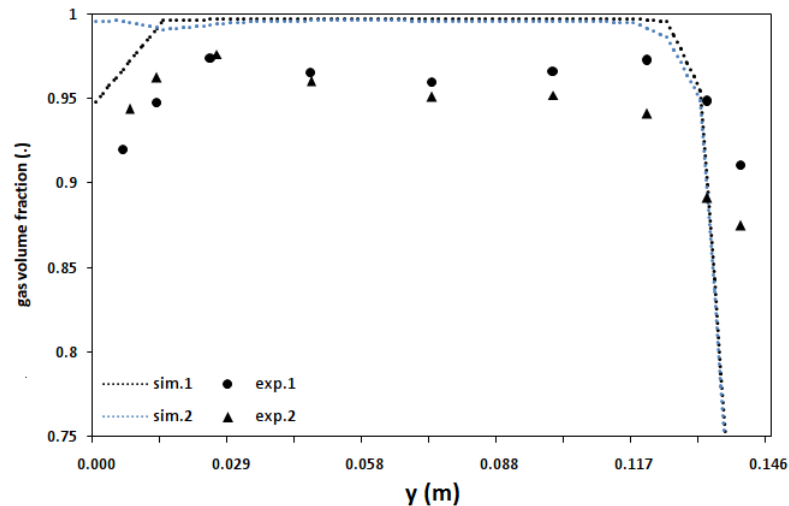


Figure 6.6: Time-averaged lateral profiles of the gas volume fraction at $x=7.06$ m and 8.98 m as shown by Figure 6.5

m above the riser inlet are examined as shown by Figure 6.6. For $x=7.06$ m and $x=8.98$ m, an asymmetric gas volume fraction profile is captured, as shown by "sim.1" and "sim.2", respectively. Comparing the simulation predictions to the experimental data of J. Zhou et al. [81], the current simulation has a poor agreement with the experimental result at both positions, "exp.1" and "exp.2". The simulation shows a dense area with a low gas volume fraction near to one side of the riser walls. The lateral profiles of the gas volume fraction obtained by the simulations do not show a symmetrical profile. Furthermore, an asymmetrical profile and generally an overestimated result are achieved by the simulation for both positions. The reason of the poor agreement between the simulation and the experiment of J. Zhou et al. [81] can be found from one of the reasons as discussed in the previous sub-chapter 6.2.1 or the combination of them.

7 Conclusions and Outlook

7.1 Conclusions

A Computational Fluid Dynamics software for simulating gas-solid riser flow has been developed. Two-Fluid Method or Eulerian-Eulerian approach is implemented into the developed code, called AIOLOS. The developed AIOLOS is then tested to predict the hydrodynamics behaviour of gas-solid flow in a 3D cylindrical and a 3D rectangular riser at transient conditions. Afterwards, the time-averaged simulation results are compared to the experimental results which are obtained by another researcher.

For the case of a 3D cylindrical riser, the investigation of the effect of different simulation parameters, meshing; initial condition; drag model; radial distribution function; restitution coefficient; simulation time step, discovers some important clues. These important findings are as follows:

1. Two different meshes are examined in order to find an optimum point. The coarser meshing looks more appropriate than the fine meshing for discretization of the simulation domain. Thus, the coarser meshing is employed for a full 40 s simulation.
2. Three different initial conditions of the simulation are examined. The simulation results show quantitatively good agreement. Therefore, it could be deduced that the effect of the initial condition used in the current simulation tends to disappear after a certain calculation time period.
3. The simulation parameters which are examined in this study are three different drag models, two different radial distribution function models, and two different coefficient

of restitution values. Using two different time steps, there are totally 24 variations of the simulations. In order to categorize 24 variations into several groups, the simulation up to 6 s is carried out for all variations. For the time step of 0.0001 s, the 12 variations of the simulations could be categorized into 5 typical groups, while with time step of 0.00015 s the simulations are clustered into 4 groups.

4. There are 13 variations of simulation parameters which are fully calculated up to 40 s. Among these, there are the best four simulation variations which show better agreement to the experimental result than the other variations, namely the simulations with Syamlal et al. and Gidaspow drag model-Syamlal et al. RDF-COR of 0.7-time step of 0.00015 s, the simulations with Syamlal et al. drag model-Syamlal et al. RDF-COR of 0.7-time step of 0.0001 s, and the simulations with Gidaspow drag model-Syamlal et al. RDF, COR of 0.84-time step of 0.0001 s.
5. The effect of radial distribution function model tends to be negligible when the simulation uses the coefficient restitution of 0.84. Both Carnahan-Starling model and Syamlal et al. model yield almost the same value either for the axial gas velocity and the solid volume fraction. Whilst the simulation that uses the coefficient restitution of 0.7, the effect of different models for radial distribution function is significant.
6. The effect of different restitution coefficient can be recognized by the increase of solid volume fraction in the area close to the riser wall with the increasing of the restitution coefficient. An increase in the restitution coefficient will generally increase the granular temperature due to the decrease of dissipation of fluctuating energy due to particle-particle collision.
7. Two different simulation time steps are employed, namely 0.0001 s and 0.00015 s. It could be resumed that the effect of different simulation time steps depends on the combination of the simulation parameters.

For the case of a 3D rectangular riser, a simulation with Syamlal et al. drag model, Syamlal et al. radial distribution function, restitution coefficient of 0.7, and simulation time step of 0.00015 s has been performed and analysed. The result showed that the simulation predicts

the gas-solid flow inside the rectangular riser poorly, as showed by the comparisons between the experimental data and the simulation result in terms of the solid velocity and the gas volume fraction profile. From these comparisons, the asymmetrical profile and generally the overestimated result are achieved by the simulation. More proper properties for the inlet condition and a finer mesh for the numerical simulation may lead to a better simulation result.

7.2 Outlook

In the course of developing, testing, and evaluating the present code and its results, there are several important hints that should be considered for the future development of the present work. The aim of these hints is to obtain a better simulation result. Here are some recommendations which may be accounted for.

1. Gas-solid multiphase flow simulation in a 3D domain is absolutely a massive calculation task. Comparing to a single phase flow, gas-solid multiphase simulation has more equations that should be solved and mostly it is a transient calculation. Thus, simulating such a case on a single computer is not efficient at all due to an exceptionally very long time obtaining the results. Therefore, none of the researchers utilizes a single computer for their gas-solid flow calculation. All of them use a parallel computer for the simulation, even though if the case is only 2D. Concerning this aspect, it is really recommended to use a parallel computer for developing the present code in the future.
2. A proper implementation of wall boundary conditions leads to a better understanding of the hydrodynamics phenomena near the wall. One of the alternatives to deal with that is by implementing the Johnson and Jackson boundary condition. The Johnson and Jackson boundary condition is adopted to describe the solid particle-wall interactions. The wall shear contributed by the solid phase is generated by the rate of axial momentum transferred to wall by the solid particles in a thin layer adjacent to the wall surface. Several previous investigations have been reported that using the Johnson and Jackson wall boundary condition, a typical region in gas-solid riser flow,

core-annulus, is successfully recognized in riser.

3. The discrepant results between the experimental and the present simulation could be contributed by the lack of the conventional drag models used in the simulation in taking into account the presence of solid clusters near the riser wall. The presence of clusters may lead to a higher pseudo solid diameter and then the terminal velocity of solid clusters becomes higher. Some reports say that it yields to down flow of solid phase and higher segregation of the solids near the wall. In order to overcome the drawback of conventional drag models in considering the cluster presence, implementing an alternative drag model called the energy minimization multi-scale (EMMS) model is a prospect that may lead to better results in the future.

Bibliography

- [1] Adnan Almuttahir and Fariborz Taghipour. Computational fluid dynamics of high density circulating fluidized bed riser: study of modeling parameters. *Powder Technology*, 185(1):11–23, 2008.
- [2] T B Anderson and Roy Jackson. Fluid mechanical description of fluidized beds: equations of motion. *Industrial & Engineering Chemistry Fundamentals*, 6(4):527–539, 1967.
- [3] G Balzer, O Simonin, A Boelle, and J Lavieville. A unifying modelling approach for the numerical prediction of dilute and dense gas-solid two phase flow. 1996.
- [4] Prabir Basu. *Combustion and gasification in fluidized beds*. CRC Press, Florida, 2006.
- [5] Prabir Basu. *Circulating fluidized bed boilers: design, operation and maintenance*. Springer, Halifax NS, Canada, 2015.
- [6] S Benyahia, H Arastoopour, TM Knowlton, and H Massah. Simulation of particles and gas flow behavior in the riser section of a circulating fluidized bed using the kinetic theory approach for the particulate phase. *Powder Technology*, 112(1):24–33, 2000.
- [7] Sofiane Benyahia, Madhava Syamlal, and Thomas J O'Brien. Study of the ability of multiphase continuum models to predict core-annulus flow. *AIChE Journal*, 53(10):2549–2568, 2007.
- [8] Sofiane Benyahia, Madhava Syamlal, and Thomas J O'Brien. Summary of mfix equations 2012-1. *NETL, Department of Energy, United States*, 2012.
- [9] JX Bouillard, RW Lyckowski, and D Gidaspow. Porosity distributions in a fluidized bed with an immersed obstacle. *AIChE Journal*, 35(6):908–922, 1989.
- [10] Luben Cabezas-Gomez, Renato César da Silva, Hélio Aparecido Navarro, and Fer-

- nando Eduardo Milioli. Cluster identification and characterization in the riser of a circulating fluidized bed from numerical simulation results. *Applied Mathematical Modelling*, 32(3):327–340, 2008.
- [11] Charles S Campbell and David G Wang. Particle pressures in gas-fluidized beds. *Journal of Fluid Mechanics*, 227:495–508, 1991.
- [12] J Cao and G Ahmadi. Gas-particle two-phase turbulent flow in a vertical duct. *International Journal of Multiphase Flow*, 21(6):1203–1228, 1995.
- [13] Norman F Carnahan and Kenneth E Starling. Equation of state for nonattracting rigid spheres. *The Journal of Chemical Physics*, 51(2):635–636, 1969.
- [14] Sydney Chapman and Thomas George Cowling. *The mathematical theory of non-uniform gases: an account of the kinetic theory of viscosity, thermal conduction and diffusion in gases*. Cambridge University Press, 1970.
- [15] J Dallavalle. Micromeritics, the technique of fine particles. *London, Sir Isaac Pitman*, pages 10–1, 1948.
- [16] AW Date. Complete pressure correction algorithm for solution of incompressible Navier-Stokes equations on a nonstaggered grid. *Numerical Heat Transfer*, 29(4):441–458, 1996.
- [17] JM Delhay and JL Achard. On the use of averaging operators in two phase flow modeling: Thermal and aspects of nuclear reactor safety, 1: Light water reactors. In *ASME Winter Meeting, Washington*, 1978.
- [18] Jianmin Ding and Dimitri Gidaspow. A bubbling fluidization model using kinetic theory of granular flow. *AIChE journal*, 36(4):523–538, 1990.
- [19] A. Einstein. Eine neue Bestimmung der Molekuldimensionen. *Ann. Phys.*, 34:591–592, 1911.
- [20] Hans Enwald, Eric Peirano, and A-E Almstedt. Eulerian two-phase flow theory applied to fluidization. *International Journal of Multiphase Flow*, 22:21–66, 1996.
- [21] Dieter Förtsch. *A kinetic model of pulverised coal combustion for computational fluid dynamics*. Dissertation, University of Stuttgart, 2003.

- [22] Xi Gao, Li-Jun Wang, Cheng Wu, You-Wei Cheng, and Xi Li. Steady-state simulation of core-annulus flow in a circulating fluidized bed (cfb) riser. *Chemical engineering science*, 78:98–110, 2012.
- [23] John Garside and Maan R Al-Dibouni. Velocity-voidage relationships for fluidization and sedimentation in solid-liquid systems. *Industrial & engineering chemistry process design and development*, 16(2):206–214, 1977.
- [24] Derek Geldart. Types of gas fluidization. *Powder technology*, 7(5):285–292, 1973.
- [25] Dimitri Gidaspow. *Multiphase flow and fluidization: continuum and kinetic theory descriptions*. Academic Press, California, 1994.
- [26] Dimitri Gidaspow, Jonghwun Jung, and Raj K Singh. Hydrodynamics of fluidization using kinetic theory: an emerging paradigm: 2002 flour-daniel lecture. *Powder Technology*, 148(2):123–141, 2004.
- [27] Masayuki Horio and Hiroaki Kuroki. Three-dimensional flow visualization of dilutely dispersed solids in bubbling and circulating fluidized beds. *Chemical Engineering Science*, 49(15):2413–2421, 1994.
- [28] Christine M Hrenya and Jennifer L Sinclair. Effects of particle-phase turbulence in gas-solid flows. *AIChE Journal*, 43(4):853–869, 1997.
- [29] M Ishii. Thermo-fluid dynamic theory of two-phase flow., volume 22 of direction des études et recherches délectricité de france. *Eyrolles, Paris*, 1975.
- [30] M Ishii. One-dimensional drift-flux model and constitutive equations for relative motion between phases in various two-phase flow regimes, anl-77-47. Technical report, Argonne National Laboratory, Illinois, United States of America, 1977.
- [31] R Jackson. Locally averaged equations of motion for a mixture of identical spherical particles and a Newtonian fluid. *Chemical Engineering Science*, 52(15):2457–2469, 1997.
- [32] Umesh Kumar Jayaswal. Hydrodynamics of multiphase flows: separation, dissemination and fluidization. Technical report, Illinois Inst. of Tech., Chicago, IL (United States), 1991.

- [33] James T Jenkins and Stuart B Savage. A theory for the rapid flow of identical, smooth, nearly elastic, spherical particles. *Journal of Fluid Mechanics*, 130:187–202, 1983.
- [34] Klas Johansson, BGM Van Wachem, and Alf-Erik Almstedt. Experimental validation of CFD models for fluidized beds: influence of particle stress models, gas phase compressibility and air inflow models. *Chemical Engineering Science*, 61(5):1705–1717, 2006.
- [35] Paul C Johnson and Roy Jackson. Frictional–collisional constitutive relations for granular materials, with application to plane shearing. *Journal of Fluid Mechanics*, 176:67–93, 1987.
- [36] Murat Koksai. Gas mixing and flow dynamics in circulating fluidized beds with secondary air injection. 2001.
- [37] Joris Koornneef, Martin Junginger, and André Faaij. Development of fluidized bed combustion an overview of trends, performance and cost. *Progress in energy and combustion science*, 33(1):19–55, 2007.
- [38] JAM Kuipers, KJ Van Duin, FPH Van Beckum, and Willibrordus Petrus Maria Van Swaaij. A numerical model of gas-fluidized beds. *Chemical Engineering Science*, 47(8):1913–1924, 1992.
- [39] Daizo Kunii and Octave Levenspiel. *Fluidization engineering*. Butterworth-Heinemann, Elsevier, New York, 2013.
- [40] Brian Edward Launder and Dudley Brian Spalding. *Mathematical models of turbulence*. Academic Press, London, 1972.
- [41] Bo Leckner. Developments in fluidized bed conversion of solid fuels. *Thermal Science*, 20(suppl. 1):1–18, 2016.
- [42] Simon Leiser. *Numerical simulation of oxy-fuel combustion*. Dissertation, University of Stuttgart, Shaker Verlag GmbH, 2011.
- [43] Warren K Lewis. *Reaction between Solids and Gases*. US Patent 2,343,780, Original Application 1941, Patented 1944, 1941.
- [44] Warren K Lewis and Edwin R Gilliland. *Conversion of Hydrocarbons with Suspended Catalyst*. US Patent 2,498,088, Original Application 1940, Patented 1950, 1940.

- [45] Jinghai Li. *Particle-fluid two-phase flow: the energy-minimization multi-scale method*. Metallurgical Industry Press, Beijing, 1994.
- [46] Jinghai Li, Congli Cheng, Zhongdong Zhang, Jie Yuan, Anton Nemet, and Franz N Fett. The emms modelits application, development and updated concepts. *Chemical Engineering Science*, 54(22):5409–5425, 1999.
- [47] Tingwen Li, Sreekanth Pannala, and Chris Guenther. Numerical simulations of a circulating fluidized bed with a square cross-section. 2011.
- [48] CKK Lun, S Br Savage, DJ Jeffrey, and N Chepurniy. Kinetic theories for granular flow: inelastic particles in couette flow and slightly inelastic particles in a general flowfield. *Journal of Fluid Mechanics*, 140:223–256, 1984.
- [49] K.M. Luo. *Dilute, Dense-Phase and Maximum Solids-Gas Transport*. PhD thesis, Illinois Institute of Technology, Chicago, 1987.
- [50] NETL. Multiphase flow with interphase exchanges (mfix). Technical report, Department of Energy, United States, 2013.
- [51] JJ Nieuwland, M van Sint Annaland, JAM Kuipers, and Willibrordus Petrus Maria van Swaaij. Hydrodynamic modeling of gas/particle flows in riser reactors. *AIChE Journal*, 42(6):1569–1582, 1996.
- [52] Peter D Noymer and Leon R Glicksman. Descent velocities of particle clusters at the wall of a circulating fluidized bed. *Chemical Engineering Science*, 55(22):5283–5289, 2000.
- [53] Preetanshu Pandey, Richard Turton, Paul Yue, and Lawrence Shadle. Nonintrusive particle motion studies in the near-wall region of a pilot-scale circulating fluidized bed. *Industrial & Engineering Chemistry Research*, 43(18):5582–5592, 2004.
- [54] RL Panton. *Incompressible flow*. John Wiley and Sons, New York, 1984.
- [55] SV Patankar. Numerical heat transfer and fluid flow. *Hemisphere Publishing Corporation, New York*, 1980.
- [56] DJ Patil, M van Sint Annaland, and JAM Kuipers. Critical comparison of hydrodynamic models for gas-solid fluidized beds-part ii: freely bubbling gas-solid fluidized beds. *Chemical engineering science*, 60(1):73–84, 2005.

- [57] Jorge A Pita and Sankaran Sundaresan. Gas-solid flow in vertical tubes. *AIChE Journal*, 37(7):1009–1018, 1991.
- [58] JF Richardson. Sedimentation and fluidization. *Trans. Inst. Chem. Eng.*, 32:35–53, 1954.
- [59] SB Savage and DJ Jeffrey. The stress tensor in a granular flow at high shear rates. *Journal of Fluid Mechanics*, 110:255–272, 1981.
- [60] David G Schaeffer. Instability in the evolution equations describing incompressible granular flow. *Journal of Differential Equations*, 66(1):19 – 50, 1987.
- [61] Von L Schiller. Uber die grundlegenden Berechnungen bei der Schwerkraftaufbereitung. *Zeitschrift des Vereines Dsutscher Ingenieure*, 77:318–320, 1933.
- [62] Milinkumar T Shah, Ranjeet P Utikar, Vishnu K Pareek, Geoffrey M Evans, and Jyeshtharaj B Joshi. Computational fluid dynamic modelling of fcc riser: A review. *Chemical Engineering Research and Design*, 111:403–448, 2016.
- [63] Milinkumar T Shah, Ranjeet P Utikar, Vishnu K Pareek, Moses O Tade, and Geoffrey M Evans. Effect of closure models on eulerian–eulerian gas–solid flow predictions in riser. *Powder Technology*, 269:247–258, 2015.
- [64] JL Sinclair and R Jackson. Gas-particle flow in a vertical pipe with particle-particle interactions. *AIChE Journal*, 35(9):1473–1486, 1989.
- [65] P Sreekanth, M Syamlal, and TJ OBrien. Computational gas-solid flows and reacting systems: Theory, methods and practice. *IGI Global, Hershey PA, USA*, 4:4493–4500, 2011.
- [66] David E Stock. Particle dispersion in flowing gases–1994 freeman scholar lecture. *Journal of Fluids Engineering*, 118(1), 1996.
- [67] M Syamlal. A review of granular stress constitutive relations. Technical report, EG and G Washington Analytical Services Center, Inc., Morgantown, WV (USA), 1987.
- [68] Madhava Syamlal and Thomas J OBrien. Computer simulation of bubbles in a fluidized bed. In *AIChE Symp. Ser*, volume 85, pages 22–31, 1989.
- [69] Madhava Syamlal, William Rogers, and Thomas J OBrien. Mfix documentation: The-

- ory guide. *National Energy Technology Laboratory, Department of Energy, Technical Note DOE/METC-95/1013 and NTIS/DE95000031*, 1993.
- [70] Mohit P Tandon and Aditya U Karnik. Simulation of rectangular fluidised bed with Geldart d particles. 2014.
- [71] Yuan P Tsuo and Dimitri Gidaspow. Computation of flow patterns in circulating fluidized beds. *AIChE Journal*, 36(6):885–896, 1990.
- [72] BGM Van Wachem, JC Schouten, CM Van den Bleek, R Krishna, and JL Sinclair. Comparative analysis of CFD models of dense gas–solid systems. *AIChE Journal*, 47(5):1035–1051, 2001.
- [73] Michael W. Weber and Christine M. Hrenya. Square-well model for cohesion in fluidized beds. *Chemical Engineering Science*, 61(14):4511 – 4527, 2006.
- [74] C Yu Wen. Mechanics of fluidization. In *Chem. Eng. Prog. Symp. Ser.*, volume 6, pages 100–101, 1966.
- [75] Joachim Werther and Ernst-Ulrich Hartge. Modeling of industrial fluidized-bed reactors. *Industrial & Engineering Chemistry Research*, 43(18):5593–5604, 2004.
- [76] Stephen Whitaker. Advances in theory of fluid motion in porous media. *Industrial & Engineering Chemistry*, 61(12):14–28, 1969.
- [77] Fritz Winkler. *Process for Production of Water Gas*. IG Farbenindustrie AG, Patent Nr 437970, 1922.
- [78] Joseph Yerushalmi and NT Cankurt. Further studies of the regimes of fluidization. *Powder Technology*, 24(2):187–205, 1979.
- [79] Joseph Yerushalmi, NT Cankurt, Derek Geldart, and Barry Liss. Flow regimes in vertical gas-solid contact systems. Technical report, City Coll., New York (USA); Bradford Univ.(UK); Coalcon, New York (USA), 1976.
- [80] Hanbin Zhong, Xingying Lan, Jinsen Gao, Yajun Zheng, and Zhiping Zhang. The difference between specular coefficient of 1 and no-slip solid phase wall boundary conditions in CFD simulation of gas–solid fluidized beds. *Powder Technology*, 286:740–743, 2015.

- [81] J Zhou, JR Grace, CJ Lim, and CMH Brereton. Particle velocity profiles in a circulating fluidized bed riser of square cross-section. *Chemical Engineering Science*, 50(2):237-244, 1995.